



**Search for New Massive Long-Lived Neutral Particles  
decaying to Photons in  $pp$  Collisions at  $\sqrt{S} = 8$  TeV**

A DISSERTATION  
SUBMITTED TO THE FACULTY OF THE GRADUATE SCHOOL  
OF THE UNIVERSITY OF MINNESOTA  
BY

Tambe Ebai Norbert

IN PARTIAL FULFILLMENT OF THE REQUIREMENTS  
FOR THE DEGREE OF  
Doctor of Philosophy

Prof. Yuichi Kubota

May, 2015

**© Tambe Ebai Norbert 2015  
ALL RIGHTS RESERVED**

# Acknowledgements

There are many people that have earned my gratitude for their contribution to my time in graduate school.

*The universe is unbiased, she chooses to reveal herself to all who have the correct attitude.*

Tambe E. Norbert

*So I would claim you are profoundly misled by thinking about physics as similar to logic or number theory. Its not! its dynamical evolution, and most results of physics problems are not nice numbers like 1 or  $\pi$  or even  $e^\pi$ .*

by Prof. Matt Strassler

# Dedication

*No, I have nothing against Mr. Einstein. He is a kind person and has done many good things, some of which will become part of the music. I will write to him and try to explain that the ether exists, and that its particles are what keep the Universe in harmony, and the life in eternity.*

Nikola Tesla

*The Universe is unbiased, she chooses to reveal herself to whomever she wants.*

Tambe E. Norbert

## Abstract

Dark matter particles are believed to be neutral, stable, weakly interacting with ordinary matter and maybe massive. The hunt for dark matter particles is on! There are theoretical models which predict the existence of dark matter particles that can be produced in a proton-proton collider like the Large Hadron Collider provided there is sufficient center of mass energy. Gauge Mediating Supersymmetric Models are examples of such models. These models describe the production and decay into isolated energetic photons, new, massive, neutral, weakly interacting particles known as supersymmetric particles. The Neutralino ( $\tilde{\chi}_1^0$ ), being the lightest supersymmetric particle in terms of mass, is a prime example and its decay into a photon is accompanied by a light weakly interacting and stable supersymmetric particle, the gravitino ( $\tilde{G}$ ) which is considered to be a very good candidate for dark matter particles. The resulting photon from such a decay, is understood to be delayed in its arrival time at the detector. This timing delay is due to inherent dynamics understood and well described by models beyond the standard model. The signature of a delayed photon is not specific to only supersymmetric models but could be the result of probably some new kind of physics unrelated to the standard model. Using the Compact Muon Solenoid detector at the LHC, we have performed a search for delayed photons produced from proton-proton collisions at the center of mass energy,  $\sqrt{S} = 8$  TeV. We did not find any excess of events over standard model background. Consequently, we compute an upper limit on the cross section  $\sigma_{\tilde{\chi}_1^0} > 0.02$  pb of the production and decay of the lightest neutralino with mass and proper lifetime;  $m_{\tilde{\chi}_1^0} \geq 235$  GeV/ $c^2$  and  $\tau_{\tilde{\chi}_1^0} \geq 35$  ns respectively, as described in a minimal gauge mediated supersymmetric model. We also show that using only the timing information of the electromagnetic calorimeter as observable, the CMS detector is sensitive to neutralinos with lifetimes up to 30 ns and mass,  $m_{\tilde{\chi}_1^0} \approx 260$  GeV/ $c^2$  which no previous experiment could show. We provide possible improvements of our search analysis which might help discover delayed photons in future.

# Contents

|  |            |
|--|------------|
| <b>Acknowledgements</b>                                    | <b>i</b>   |
| <b>Dedication</b>  | <b>ii</b>  |
| <b>Abstract</b>  | <b>iii</b> |
| <b>List of Tables</b>                                      | <b>vii</b> |
| <b>List of Figures</b>                                     | <b>ix</b>  |
| <b>1 Introduction</b>                                      | <b>1</b>   |
| <b>2 Phenomenology of Long-Lived Particles</b>             | <b>5</b>   |
| 2.1 The Standard Model of Particle Physics . . . . .       | 5          |
| 2.1.1 Main Components of the SM . . . . .                  | 5          |
| 2.1.2 Spontaneous Symmetry Breaking . . . . .              | 11         |
| 2.1.3 Limitations of the Standard Model . . . . .          | 14         |
| 2.2 Beyond Standard Model Physics . . . . .                | 15         |
| 2.2.1 Supersymmetry . . . . .                              | 16         |
| 2.2.2 Minimal Supersymmetric Standard Model . . . . .      | 17         |
| 2.3 Gauge Mediated Supersymmetry Breaking Models . . . . . | 20         |
| 2.3.1 Phenomenology . . . . .                              | 21         |
| 2.3.2 Long-Lived Particles in GMSB Models . . . . .        | 22         |
| 2.4 Previous Search Experiments . . . . .                  | 29         |

|  |           |
|--|-----------|
| <b>3 Hadron Collider and Detector</b>                        | <b>31</b> |
| 3.1 Large Hadron Collider . . . . .                          | 31        |
| 3.1.1 Overview . . . . .                                     | 31        |
| 3.1.2 Colliding Energy . . . . .                             | 32        |
| 3.1.3 Luminosity . . . . .                                   | 33        |
| 3.1.4 LHC Bunch Structure . . . . .                          | 34        |
| 3.2 Compact Muon Solenoid . . . . .                          | 38        |
| 3.2.1 Overview . . . . .                                     | 38        |
| 3.2.2 Calorimeter . . . . .                                  | 40        |
| 3.2.3 Muon Chambers . . . . .                                | 45        |
| 3.2.4 Triggering . . . . .                                   | 47        |
| <b>4 Timing Reconstruction and Calibration</b>               | <b>48</b> |
| 4.1 Electromagnetic Calorimeter Readout Chain . . . . .      | 50        |
| 4.2 Timing Extraction . . . . .                              | 53        |
| 4.3 Timing Resolution . . . . .                              | 55        |
| 4.3.1 Timing Calibration Procedure . . . . .                 | 58        |
| 4.3.2 Offline Timing Calibration . . . . .                   | 58        |
| 4.3.3 Hardware Timing Calibration . . . . .                  | 61        |
| 4.3.4 Timing Bias . . . . .                                  | 64        |
| 4.4 Electromagnetic Calorimeter Timing Performance . . . . . | 68        |
| <b>5 Event Reconstruction</b>                                | <b>72</b> |
| 5.1 Physics Object Reconstruction . . . . .                  | 72        |
| 5.1.1 Supercluster Reconstruction . . . . .                  | 73        |
| 5.1.2 Vertex and Track Reconstruction . . . . .              | 76        |
| 5.1.3 Photon or Electron Identification . . . . .            | 78        |
| 5.1.4 Muon Reconstruction . . . . .                          | 83        |
| 5.1.5 Jet Reconstruction . . . . .                           | 85        |
| 5.1.6 Missing Transverse Energy Reconstruction . . . . .     | 86        |
| 5.2 Anomalous Signals . . . . .                              | 88        |
| 5.3 Using Timing for Event Cleaning . . . . .                | 91        |

|  |            |
|--|------------|
| <b>6 Search Analysis for Long-Lived Particles</b>              | <b>93</b>  |
| 6.1 Analysis Strategy . . . . .                                | 93         |
| 6.1.1 Signal and Background Modelling . . . . .                | 95         |
| 6.1.2 Datasets . . . . .                                       | 96         |
| 6.2 Event Selection . . . . .                                  | 98         |
| 6.2.1 Trigger . . . . .  | 100        |
| 6.2.2 Offline Selection . . . . .                              | 101        |
| 6.2.3 ECAL Time . . . . .                                      | 104        |
| 6.3 Background Estimation . . . . .                            | 109        |
| 6.3.1 Non-Collision Backgrounds . . . . .                      | 111        |
| 6.3.2 Collision Backgrounds . . . . .                          | 117        |
| 6.3.3 Event Cleaning, Veto Performance and Fake Rate . . . . . | 117        |
| 6.3.4 Background Estimation Cross Check . . . . .              | 122        |
| 6.4 Results . . . . .  | 127        |
| 6.5 Systematic Studies . . . . .                               | 128        |
| <b>7 Statistical Analysis</b>                                  | <b>130</b> |
| 7.1 Limit Computation . . . . .                                | 130        |
| 7.1.1 CLs Technique . . . . .                                  | 131        |
| 7.1.2 Statistical Test Formalism . . . . .                     | 132        |
| 7.1.3 Test Statistics and $p$ -values . . . . .                | 134        |
| <b>8 Limit Interpretation</b>                                  | <b>138</b> |
| 8.1 Signal Efficiency and Acceptance . . . . .                 | 138        |
| <b>9 Conclusion</b>  | <b>143</b> |
| <b>Bibliography</b>  | <b>144</b> |
| <b>Appendix A. Glossary and Acronyms</b>                       | <b>149</b> |
| A.1 Glossary . . . . .   | 149        |
| A.2 Acronyms . . . . .   | 149        |

# List of Tables

|     |  |     |
|-----|--|-----|
| 2.1 | SM particles and their gauge multiplets(representation) with quantum numbers. the numbers for example ( <b>3</b> , <b>2</b> , $\frac{1}{6}$ ) means ( <i>triplet, doublet, Y = 1/6</i> ) representations. . . . .  | 11  |
| 2.2 | Supermultiplets and particle spin in SM and Supersymmetry. . . . .   | 17  |
| 2.3 | Chiral supermultiplets and representation in Minimal Supersymmetric SM (MSSM). Super symmetric particles (sparticles) have a $\sim$ on them. Spin -0 fields are complex scalars while spin-1/2 fields are left-handed two component Weyl fermions. . . . . | 18  |
| 2.4 | Gauge supermultiplets and representation in Minimal Supersymmetric SM (MSSM). Super symmetric particles (sparticles) have a $\sim$ on them. . . . .  | 18  |
| 3.1 | LHC operation parameter conditions during RUN 1, 2010-2013 . . . . .   | 37  |
| 3.2 | CMS detector material, Ref.[20], and resolution(Time resolution: $N \approx 35$ ns, $\bar{C} \approx 0.070$ ns Ref. [37]) . . . . .  | 40  |
| 4.1 | ECAL timing resolution absolute time and single precision for 2011 and 2012 of LHC Run 1 . . . . .   | 71  |
| 5.1 | Simple Cut-Based criteria for High energy electron and photon identification in CMS . . . . .  | 82  |
| 6.1 | Dataset and corresponding integrated luminosity totaling $19.1 \text{ fb}^{-1}$ used in this analysis . . . . .  | 97  |
| 6.2 | The signal GMSB SPS8 MC samples for difference $\Delta$ and Branching Ratios used in this analysis . . . . .   | 98  |
| 6.3 | The $\gamma +$ jets samples used in this analysis . . . . .  | 98  |
| 6.4 | The photon identification and selection criteria used in this analysis . . . . .   | 102 |
| 6.5 | The Jet ID selection used in this analysis . . . . .   | 103 |

|      |  |     |
|------|--|-----|
| 6.6  | Fake rates for different non-collision cleaning. . . . .   | 118 |
| 6.7  | ABCD Control Regions (CRs) for estimating non-collision background. .  | 120 |
| 6.8  | $A' B' C' D'$ and $I I'$ CRs for estimating collision background. . . . .  | 120 |
| 6.9  | Result from closure test of background estimation technique using 0 and<br>1-jet events. Numbers in bracket represent our expected background<br>estimate using ABCD method. . . . .   | 122 |
| 6.10 | Result of observed events and estimated background from signal sample,<br>events with at least 2-jets. Numbers in bracket represent our observed<br>number of events while numbers not in bracket are our expected number<br>of background events estimated using ABCD method. . . . . | 127 |
| 6.11 | Final number for $\Lambda = 180$ TeV GMSB SPS8 MC signal events events<br>passing our selection cuts. . . . .  | 128 |
| 6.12 | Summary of systematic uncertainties used in this analysis and applied to<br>our cross-section upper limit, $\sigma_{UL}$ calculation. . . . .  | 129 |
| A.1  | Acronyms . . . . .   | 150 |

# List of Figures

|     |   |    |
|-----|---|----|
| 2.1 | Higgs boson ‘‘Mexican hat’’ potential, $V(\phi^*\phi) = \mu^2(\phi^*\phi) + \lambda(\phi^*\phi)^2$ , which leads to spontaneous symmetry breaking with choice of parameters $\mu^2 < 0, \lambda > 0$ . . . . .  | 13 |
| 2.2 | SM particles and their interactions with vector bosons as mediators. . . . .  | 13 |
| 2.3 | Higgs mass contributions from its coupling to fermions (a) and scalar (b) fields. . . . .   | 15 |
| 2.4 | Supersymmetry particle mass spectra in the SPS8 or minimal GMSB (mGMSB) model. . . . .  | 20 |
| 2.5 | Feynman diagrams of gravitino/golstino, $\tilde{G}$ , gaugino and scalar interactions with superpartner pairs $(\psi, \phi)$ scalar (a) and $(\lambda, A)$ gaugino (b) decay to gravitino. . . . .  | 21 |
| 2.6 | Supersymmetry production cross-section against sparticle mass for different modes of supersymmetry production at a proton-proton collider. $pp \rightarrow \tilde{g}\tilde{g}$ processes have the dominant production cross section. . . . .                              | 24 |
| 2.7 | Feynman diagrams for gluino single ( <i>top left</i> ) and double ( <i>top right</i> ) photon and squarks single ( <i>bottom left</i> ) and double ( <i>bottom right</i> ) photon production from cascade decays of gluino and squark at LHC. . . . .                     | 25 |
| 2.8 | Neutralino transverse momentum distribution( <i>top left</i> ) and proper decay length( <i>top right</i> ) with its decayed photon transverse momentum distribution( <i>bottom left</i> ) and time of arrival at ECAL( <i>Bottom right</i> ) for GMSB SPS8 model. . . . . | 29 |
| 2.9 | Neutralino lifetime and mass upper limit from ATLAS(left) and CMS(right) 7 TeV analysis with non-pointing photons and MET. . . . .  | 30 |
| 3.1 | Schematic diagram showing the full Large hadron Collider. . . . .   | 32 |

|     |   |    |
|-----|---|----|
| 3.2 | Cumulative luminosity versus day delivered to (blue), and recorded by CMS (orange) during stable beams and for p-p collisions at 8 TeV center-of-mass energy in 2012. . . . .   | 34 |
| 3.3 | Longitudinal Profile taken with Longitudinal Density Monitor (LDM) detector showing definition of Ghost/Satellite bunches with respect to main bunches. . . . .   | 35 |
| 3.4 | (left)Arrival time distribution(red) of ATLAS MBTS for LHC fill 1533 during 2010 Pb-Pb run and LDM profile(black) for Beam2(same for Beam1).<br>(Right) Timing of Clusters in the CMS endcap calorimeters for fill 1089:Left:<br>EEP detector(left side of IP $z > 0$ ) Right: EEM detector( right side of IP, $z < 0$ ). Plots from ATLAS Ref.[28] and CMS, Ref.[29] . . . . . | 36 |
| 3.5 | CMS Detector showing the different subdetectors and their material. . .   | 39 |
| 3.6 | CMS detector schematic view with definition of $x - y - z$ coordinates. .   | 39 |
| 3.7 | Schematic diagram of CMS calorimetry system with HCAL enclosing ECAL in the Barrel and Endcap regions. . . . .  | 41 |
| 3.8 | Layout of the CMS electromagnetic calorimeter showing the arrangement of crystal modules, supermodules in the barrel with the preshower in front of endcap with supercrystals. . . . .  | 46 |
| 3.9 | Cross section view showing the coverage range of CMS sub-detectors and their longitudinal distance from the IP. . . . .   | 46 |
| 4.1 | Schematic diagram of the CMS ECAL ReadOut Chain. . . . .  | 53 |
| 4.2 | Typical pulse shape of a given signal showing crystal signal. . . . .   | 53 |
| 4.3 | <i>Left:</i> A measured ECAL pulse shape for a single channel. <i>Right:</i> $T - T_{MAX}$ Vs $R(T)$ showing the distribution of $T(R)$ . Solid line is reference shape or shape from test beam while dots correspond to a 10 discrete samples corresponding to signal from proton-proton collision. . . . .  | 54 |
| 4.4 | Deviation of the timing difference as a function of $A_{eff}/\sigma_n$ between two crystals sharing an energy in the same electromagnetic shower obtained during electron testbeam measurements. The single crystal energy scales for barrel (EB) and endcap (EE) is overlaid. The fitted results give $N = (35.1 \pm 0.2)$ ns and $\bar{C} = (20 \pm 4)$ ns. . . . .           | 57 |

|      |  |    |
|------|--|----|
| 4.5  | <i>Top 3:</i> Timing calibration maps showing the distribution of mean time for each channel/PbWO <sub>4</sub> crystal in EB (top) and EE (below: EE-(left), EE+(right)) before calibration. <i>Bottom 3:</i> Timing calibration maps showing the distribution of mean time after calibration. After calibration most crystals have an average time of zero(Green). . . . .  | 61 |
| 4.6  | <i>Top:</i> Crystal mean time distribution for crystals in readout electronics EB±8. Crystal time obtained from Laser data. <i>Bottom:</i> Clock and Control Unit (CCU) mean timing shift distribution of readout electronics of EE+ and EE-. The adjustment for global timing shift per FED due to difference in light source for each CCU has been shown to reduce the possibility of CCU showing false timing shift. The figures show $\Delta t_{CCU}$ distributions after the global shift has been removed. . . . . | 64 |
| 4.7  | Distribution of mean time ( $\mu$ ), <i>top row</i> ) and timing deviation ( $\sigma$ , <i>bottom row</i> ) as a function of crystal energy for EB prior (left) and after (right) timing bias corrections depending on amplitude have been applied. . . . .  | 66 |
| 4.8  | <i>Top row:</i> Distribution of mean time ( $\mu$ ) as a function of amplitude (left) and resolution ( $\sigma$ ) as a function of amplitude (right) for different pseudo-rapidity regions in the barrel. <i>Bottom:</i> All modules in EB combined timing resolution as a function against $\eta$ crystals in the same readout electronics in barrel (EB). . . . .  | 67 |
| 4.9  | Ecal time difference between the two reconstructed electrons in $Z \rightarrow e^-e^+$ decay. The electron time is the seed (crystal with highest energy deposit) time with additional correction due to the time of flight of the electron in EB and EE . . . . .   | 69 |
| 4.10 | Ecal absolute time of a single reconstructed electron in $Z \rightarrow e^-e^+$ decay. The electron time is the seed (crystal with highest energy deposit)time of the electron in EB and EE . . . . .  | 69 |
| 4.11 | Timing resolution from: <i>left:</i> Two most energetic crystals in the same readout unit, <i>right:</i> Two most energetic crystals belonging to different readout units, as a function of effective amplitude( $A_{eff} = A_1A_2/\sqrt{A_1^2 + A_2^2}$ ) normalized to noise in EB. Both crystals are from reconstructed electrons in $Z \rightarrow e^-e^+$ events. . . . .   | 70 |

|     |  |     |
|-----|--|-----|
| 5.1 | Superclustering algorithm in ECAL for both hybrid (EB) and island (EE) clustering algorithms. . . . .  | 74  |
| 5.2 | Superclustering in ECAL for hybrid clustering algorithm in barrel. . . . .   | 74  |
| 5.3 | Superclustering in ECAL for Island clustering algorithm in barrel. . . . .   | 75  |
| 5.4 | $Z \rightarrow e^+e^-$ mass plot showing resolution and energy scale that is obtained from applying energy scale corrections to account for intrinsic spread in crystal and photo-detector response and time-dependent corrections to compensate for channel response loss for EB (right) and EE (left) . . . . .  | 79  |
| 5.5 | Super-clusters showing resolution and energy scale that is obtained from applying energy scale corrections for EB (right) and EE (left) . . . . .  | 79  |
| 5.6 | Illustration of the differences between proton-proton collision muons, cosmic and halo muons. (a) Muons from collision propagating from the center and moving outwards in a well defined pattern, (b) Cosmic muons penetrating the detector and leaving signals in opposite hemispheres of the muon system, (c) Cosmic muons leaving signals in the tracker and opposite hemispheres, (d) cosmic muons entering and leaving the detector without passing through the muon detector layers, (e) beam halo muons penetrating the detector and leaving signals in the endcaps and (f) Cosmic muons entering the detector through the endcap and leaving through the barrel and which can happen in a vice-versa manner. . . . . | 84  |
| 6.1 | Schematic diagram showing $\tilde{\chi}_1^0 \rightarrow \gamma + \tilde{G}$ decay topology within the ECAL volume of the CMS detector. Proton beams are also shown showing the possible production of collision and non-collision delayed photons . . . . .  | 100 |
| 6.2 | Trigger efficiency turn-on curves for photon $p_T$ and $E_T^{\text{miss}} > 25$ GeV (left) and for $E_T^{\text{miss}}$ with photon $p_T > 80$ GeV/c (right). The $\gamma +$ jets samples require photon $p_T > 170$ GeV/c for selecting events with true $E_T^{\text{miss}}$ . . . . .   | 101 |
| 6.3 | Pulse shape profile showing a spike (solid line) and a real photon (dashed line) from data. . . . .  | 104 |

|      |  |     |
|------|--|-----|
| 6.4  | Timing distribution of photons showing timing measurements using seed crystal (black) and using Weighted Average basic cluster time (blue). Resolution ( $\sigma$ ) from seed time is better compared to that for cluster time which is computationally intensive. Together with the $\chi^2$ , the seed time performs better in identifying anomalous timing objects. . . . .   | 105 |
| 6.5  | Timing distribution of photons showing timing of data and MC $\gamma+$ jets (blue) samples and data (red) before (left) and after (right) timing Calibration is applied to MC. . . . .   | 106 |
| 6.6  | ECAL timing distribution of photons in barrel (EB), endcap (EE) and all of ECAL (ALL ECAL) with $p_T > 50$ GeV from data. A 2.5 ns delay timing structure is observed in endcap subdetector. . . . .   | 107 |
| 6.7  | Sources of delayed photons produced from neutralino decay in the SPS8 model with $\Lambda = 180$ TeV and $c\tau = 6000$ mm arriving at ECAL. . . . .   | 108 |
| 6.8  | ECAL time against $\eta$ (left) and ECAL time against $\phi$ (right) for photons with $p_T > 60$ GeV from data. The lower plot shows the photon timing distribution for events with different jet multiplicity. . . . .  | 110 |
| 6.9  | ECAL time Vs $\eta$ (left) and ECAL time Vs $\phi$ (right) and $CSC(Seg, \gamma)\Delta\phi$ for photons with $p_T > 80$ GeV from data. Halo photons show a clear matched between CSC segments and ECAL cluster in $\Delta\phi$ with their distribution peaking at $\phi = 0, \pm\pi$ and also the shape of their expected time. . . . .  | 114 |
| 6.10 | 2 dimensional plot showing $DT\Delta\eta(Seg, \gamma)$ against $DT\Delta\phi(Seg, \gamma)$ for photons with $p_T > 80$ GeV, ECAL Time, $t_\gamma > 2$ ns and ECAL Time $t_\gamma < -3$ ns from proton-proton collision data (left) and pure cosmic muon data (right). Small $\Delta\eta$ and $\Delta\phi$ are cosmic photon candidates. . .  | 115 |
| 6.11 | Plot showing <i>number of crystals</i> in photon supercluster for photons from the region with ECAL Time, $t_\gamma < 0$ ns. Figure shows the timing distribution of candidate true photons(black), spike candidate photons (magenta) and halo candidate photons (red). The toplogical swiss-cross variable ( $1-E_4/E_1$ ) distribution is shown comparing true photons ( $ t_\gamma  < 1.0$ ) to spike populated sample. . . . . | 116 |

|      |   |     |
|------|---|-----|
| 6.12 | Residual Background after tagging the different non-collision background sources using the methods described in text. . . . .   | 119 |
| 6.13 | ECAL time, $t_\gamma$ Vs $\eta_\gamma$ (top) and $t_\gamma$ Vs $\phi$ (bottom) for photons from <b>SinglePhoton</b> dataset (left) compared to electron candidates from the <b>DoubleElectron</b> dataset (right). All photons or electron candidates are in barrel subdetector. Most of the photons with $\phi = 0, \pm\pi$ are halo photons which are not observed in the $Z$ boson candidate sample. . . . . | 123 |
| 6.14 | Di-electron candidate mass distribution and the time of both electrons for the signal $76 < m_Z < 100$ GeV/ $c^2$ $Z$ boson sample(left) and similar distributions from the Control ( $50 < m_Z < 76$ GeV/ $c^2$ and $100 < m_Z < 130$ GeV/ $c^2$ ) sample (right). Candidates events from the DoubleElectron dataset. . . . .  | 124 |
| 6.15 | <i>Top:</i> Control sample (left) and signal sample (right) of di-electron candidate mass distribution. <i>Bottom:</i> Figure showing definition of scale factor use in estimating the contributions from control sample in signal sample.  | 126 |
| 6.16 | Timing distribution of genuine $Z$ bosons after background contribution has been subtracted. . . . .  | 127 |
| 7.1  | Sampling distributions for $f(t_\mu \mu)$ showing how one extracts the $p$ -vlaues. left: is the using a analytic of the Asymptotic method and right: is from the HybridNew method. . . . .   | 135 |
| 7.2  | Distribution of $p$ -vlaues showing how upper limit on $\mu$ is extracted for a given threshold probability. . . . .  | 137 |
| 8.1  | The reconstruction and selection efficiency (left) $\times$ Acceptance ( $t > 3$ ns) (right) against transverse decay length in laboratory frame for different $c\tau$ points. . . . .  | 139 |
| 8.2  | Neutralino production cross section against proper delay length upper limit interpretation in SPS8 model. (Left) $\Lambda = 100$ TeV, (Right)(left) $\Lambda = 180$ TeV . . . . .   | 140 |
| 8.3  | Neutralino production cross section against neutralino mass upper limit at 95% confidence levels interpretation in SPS8 model.(Left) $C\tau = 11000$ mm, (Right) $C\tau = 6000$ mm . . . . .  | 141 |

- 8.4 Neutralino two dimensional exclusion limit of neutralino mass ( $\Lambda$ ) against proper delay length upper limit interpretation in SPS8 model in the decay  $\tilde{\chi}_1^0 \rightarrow \gamma + \tilde{G}$  with limits from previous experiments shown. . . . . 142

# Chapter 1

## Introduction

We have performed a search for Neutral Massive Long-Lived Particles (NMLLP) decaying to photons using timing information. This analysis uses data recorded using the CMS detector from proton-proton ( $pp$ ) collisions by the Large Hadron Collider (LHC) with a center of mass energy  $\sqrt{S} = 8$  TeV.

Particles from the decay of NMLLP could be *Dark Matter* (DM) particles as they are weakly interacting and stable. Matter observed around us make up only 4.5% of our total universe or multiverse. It is best described with unmatched precision by simple symmetries known as gauge symmetries. The mathematical formulation of gauge symmetries used in our understanding of the visible or baryonic universe is best implemented in the Standard Model (SM). The SM cannot describe non-visible or non-baryonic matter (DM) which make up the larger percentage of matter content in our universe. Although a direct detection of DM is yet to be presented, indirect detection experiments in Cosmology and Astrophysics support speculation that non-visible matter is made up of particles which may be very stable or have long lifetime collectively called *Long-Lived* (LL) particles. In general, LL particles are either charged (electromagnetically charged (i.e interact with light (photons)) or color charged) or neutral (i.e cannot interact with light in the context of the SM).

Of particular interest to the scientific community are neutral LL particles, since DM is understood to not interact directly with light and could very weakly interact with visible matter. Recent negative search results is indicating that dark matter particles,

if they exists, could be very light i.e having very small mass of about a few eV to keV. These are known as Warm Dark Matter (WDM). DM particles could also be heavy with mass in the GeV to TeV mass range. These are called Cold Dark Matter (CDM). A common property is that they are stable.

The phenomenon of interest is a delayed photon produced in the decay of a meta-stable Next-to-Lightest Supersymmetric Particle (NLSP). The NLSP is the NMLLP. A classic example of a NLSP is the neutralino ( $\tilde{\chi}_1^0$ ). It decays into a photon and the Lightest Supersymmetric Particle (LSP) called the gravitino ( $\tilde{G}$ ). In R-parity conserving (RPC) models, supersymmetric particles like the neutralino are produced in pairs at a particle collider. The neutralinos are produced in a cascade decay of higher massive supersymmetric particles produced from proton-proton ( $pp$ ) collisions. The gravitino being the LSP is stable, light in mass, neutral and weakly interacting with ordinary matter. This makes it a good candidate particle for DM. The photons from neutralino decay are energetic, isolated and delayed in their arrival time at a detector. These photons can be detected using the electromagnetic calorimeter. High transverse momentum ( $p_T$ ) spray of hadronic particles collectively called jets and missing transverse energy due to the weakly interacting nature of the gravitino as it leaves the detector undetected, accompany this decay. The measured photon arrival time at the electromagnetic calorimeter is large (nanoseconds (ns)) because of the inherently long neutralino lifetime and extra distance traveled inside the detector. This combination of jets, missing transverse momentum and delayed photon is a clear signal for a new kind of physics beyond the standard model (SM). An event with the decay of a neutralino, produced in the LHC  $pp$  collider would be recorded using the Compact Muon Solenoid (CMS) detector. The CMS detector is located at one of the beam crossing or collision points (also known as Interaction Point (IP)) at Point 5 in Cessy, France. Relying on the excellent timing and energy resolution of Electromagnetic Calorimeter (ECAL) sub detector, of the CMS detector, we can distinguish between high energy photons from NMLLP decay and photons produced in interactions precisely and well described by the SM. Finding such a LL particle would address a lot of important questions in modern physics like: Why do we observe so much matter than anti-matter in our universe? Is there a reason

why particles as currently observed in the SM have very different masses and can be classified to exists in 3 generations? What is the origin and existence of Dark Matter (DM) and what is it made of? Do all fundamental forces behave the same way at some higher energy scale? Answers to these questions will provide a clear understanding and direction towards studying physics beyond the standard model.

We have described in this thesis, a search analysis for delayed photons with results. This description is arranged as follows in the following chapters:

- Chapter 1 gives an introduction and general outline of this thesis.
- In Chapter 2, we give a brief description of the current standard model highlighting its strengths and weaknesses. We also describe *supersymmetric* models which are theoretical extensions beyond the standard model (BSM) embedded with the prediction of NMLLP. The physics of long-lived particle is also described. This chapter also presents compelling hints from theory, experiment as well as cosmological observation supporting the existence of NMLLPs which motivates our search. The phenomenology of NMLLP in *gauge mediating supersymmetric* models is used as a benchmark model in our search. Results from previous search analysis are also presented.
- Chapter 3, describes the experimental setup particularly the LHC collider and CMS detector giving detail description of its sub-detectors emphasizing on those which have been used in our search analysis.
- Timing reconstruction and calibration is described in chapter 4, detailing the method of extraction and calibration procedure used by CMS.
- In chapter 5, the reconstruction of physics objects such as superclusters, photons, jets and missing transverse energy ( $E_T^{\text{miss}}$ ) according the CMS standards is described here. The presence of anomalous signals in the electromagnetic calorimeter is also mentioned.
- The search analysis is described in chapter 6 detailing triggers used, dataset, choice of observables, event selection and background estimation techniques used. The

result of the search is also presented here. Sources of systematic and quantification considered in this experiment are also described.

- Chapter 7 presents the statistical analysis and methods used providing clear meaning of  $p$ -values as used in this search analysis.
- Using the minimal *Gauge Mediating Supersymmetric Model* (mGMSB) with *Snowmass Signal Point 8* (SPS8) as our benchmark model, chapter 8 provides an interpretation of our results in terms of exclusion regions reached by our analysis. Possible improvement for future analysis is briefly mentioned.
- In chapter 9, we present our conclusion from performing the search for delayed photons.

## Chapter 2

# Phenomenology of Long-Lived Particles

### 2.1 The Standard Model of Particle Physics

The Standard Model (SM) provides a thorough and experimentally valid mathematical description of the fundamental constituents of baryonic matter and its interactions (except gravity) of our universe. Predictions using the SM agree with most of the available experimental data with unmatched precision. However, there are some theoretical and experimental difficulties with the model, such as, the observational evidence for the existence of Dark Matter (DM) in gravitational lensing experiments, the experimental evidence for neutrino oscillation and neutrino masses and gravitational interactions. These observations cannot be explained using the SM. As a result, it is believed that the SM could be the lower energy extension of a more general model. A candidate mathematical model which extends the SM providing possible explanation for these observations is *supersymmetry*. In the next section, we briefly describe the SM highlighting its major components, its strengths and some of its limitations.

#### 2.1.1 Main Components of the SM

Mass, Charge, Spin and Lifetime can be used to identify and categorize fundamental particles of nature. *Spin* is an *internal quantum number* i.e a non-spatial unlike mass

and charge. A particle's spin is expressed in units of  $n\hbar$ , where  $n$  can be *integer* or *half-integer*. Half-integer spin ( $\frac{1}{2}, \frac{3}{2}, \dots \times \hbar$ ) particles obey a *Fermi-Dirac* statistics. These are called *fermions*. No two identical fermions can occupy the same quantum state. While integer spin particles ( $0, 1, 2, \dots \times \hbar$ ) obey *Bose-Einstein* statistics. These are called *Bosons*. Any number of bosons can occupy a given quantum state. Particles also have their *Anti-particles* which have the same mass and spin as the particle but have opposite charge. Particles and anti-particles can be massive or massless and charged or neutral. Fermions are the fundamental building blocks of the material or matter in our universe while bosons help mediate interactions between fermions. No spin =  $0\hbar$  particle had ever been experimentally observed prior to the 4th of July 2012 when the *Higgs* boson which is a favorable candidate for the first spin-0 particle was observed, Ref.[1]. The Higgs boson is responsible for providing mass to both fermions and bosons. Its discovery completes the SM. From an elementary view point, it is not unreasonable to classify the present and possibly future fundamental particles describing our universe using a spin set,  $S$ , given as:

$$S = \{s = (\dots, 0, \frac{1}{2}, 1, \frac{3}{2}, 2, \dots) \cdot \hbar\}$$

where  $s$  is the spin of a particle and  $\hbar$  is the fundamental *Planck* constant. Our present and possibly future understanding of the universe can thus be summarize as:

- $S = \frac{1}{2}\hbar$  Particles which make up all the matter in our universe.
- $S = 1\hbar$  Mediating particles for gauge interactions.
- $S = 0\hbar$  The fundamental particle responsible for giving mass to other particles.
- $S = 2\hbar$  Mediator for gravitational interactions (might be gauged).
- $S = \frac{3}{2}\hbar$  Particles which make up **Dark Matter?**

However, a subset of the above set with particle spins,  $s = \{0, \frac{1}{2}, 1\}\hbar$  very precisely describes only  $\approx 4\%$  of the entire universe using the mathematical understanding provided by SM. This mathematical framework is a *relativistic quantum field theory* in which particles are represented as *quantum fields* and their dynamics and interaction with other particles can be expressed using a mathematical functions called the *Lagrangian density*,

$\mathcal{L}$ . The Lagrangian density describes the dynamics of fermions, bosons and their interactions with the Higgs boson. Fermions and bosons obtain their mass interacting with the Higgs boson through a process fundamental to the SM called the *Higgs Mechanism*. In our brief description of the SM, we have divided it into the following sections:

- **Fermions:** All of visible matter is described using fermion fields.
- **Interactions:** Fermions interact either through electromagnetic, weak and strong interactions with vector bosons mediating those interactions. An interaction is described by a given symmetry.
- **Spontaneous Symmetry Breaking or Higgs Mechanism:** Fermions originally have no mass. They get their mass by interacting with the Higgs field through a process known as *Higgs mechanism*. New states or particles of matter can be formed from mixing other states or fermions.

## Fermions

The *Dirac* equation given as:

$$\mathcal{L}(\bar{\psi}, \psi, G^\mu) = \bar{\psi} (i\gamma^\mu \mathcal{D}_\mu - m) \psi \quad (2.1)$$

describes fermion dynamics and interaction. Fermions exist in *pairs* known as *doublets* in the SM as either leptons ( $\ell$ ) or quarks ( $q$ ) and come in 3 *generations*. The SM gives no explanation for the existence of only 3 generations. Leptons do participate in electromagnetic and weak interactions but not in strong interactions while quarks participate in all three interactions. In the SM, leptons have integer charge while quarks have fractional charge. The 3 generation of quarks and leptons also known as *flavors* are arranged in a mass hierarchy with the third generation being the heaviest. The second and third generation being meta stable can disintegrate or *decay* into the first generation through weak interactions. A lepton pair or doublet consists of a particular lepton flavor and its corresponding neutral neutrino flavor type. For example, an **electron** ( $e$ ) and its corresponding electron **neutrino** ( $\nu_e$ ) make the first generation pair, ( $e, \nu_e$ ). Other lepton flavors include **muon** ( $\mu$ ) and **muon neutrino** ( $\nu_\mu$ ) pair ( $\mu, \nu_\mu$ ) and **tau** ( $\tau$ ) and **tau neutrino** ( $\nu_\tau$ ) pair ( $\tau, \nu_\tau$ ). In the SM, neutrinos are described as

having no mass, however, numerous experiments have confirmed that neutrinos have a very tiny mass (order of electronvolts (eV)) and can oscillate from one flavor or generation into another over sufficiently large distances.

On the other hand, a first generation pair of quarks consists of an “*up-type*” and a “*down-type*” quark. In addition to the electric charge, quarks also carry a *color* charge and as a result can equally participate in strong interactions. *Up-type* quarks like **up** (u), **charm** (c), **top** (t) have charge of  $+\frac{2}{3}$  and *down-type* quarks such as **down** (d), **strange** (s), **bottom** (b) have a charge of  $-\frac{1}{3}$ . Charges are expressed in units of elementary charge e. Quark doublets include (u, d) as the first generation and (c, s) and (t, b) as second and third generations respectively. Quarks do not exist as free particles in nature and are found in bound states as composite particles like *protons* and *neutrons* collectively called *hadrons*. The distributions of these quarks inside hadrons can be modeled using *parton distribution functions* (PDF) which depends on the fraction of momentum of the given hadron carried by each quark.

One can distinguish between “Left” from the “Right” handed fermions based on the nature of their interaction with electroweak bosons. Since most particles in the second and third generation are meta-stable, it is possible to describe all visible matter in our universe using only one generation of leptons, **electron** and the **electron neutrino** ( $e, \nu$ ) and one generation of quarks, **up-quark** and **down quark** (u,d).

## Interactions

Fermions interaction is mediated by particles called vector *bosons*; i.e  $s = 1\hbar$ . The SM describes three different forces and their carriers. The *electromagnetic force* described using the mathematical frame work of *Quantum Electrodynamics* (QED). Its force carrier is a massless vector boson called the *photon* ( $\gamma$ ). The two nuclear forces which include the *weak force* which was developed later in the 1960s in a combined *electro-weak* framework of *Electro-Weak Field Theory* independently developed by Sidney Glashow, Abdus Salam and Steven Weinberg, Ref.[2] have 3 massive vector bosons  $W^\pm, Z^0$  discovered at CERN in 1983 as its force-mediating particles. Finally, the *strong force* described using the frame work of *Quantum Chromodynamics* (QCD), is mediated by massless *gluons* (g). The strong force is not unified with the other two forces. It remains an open question whether at a much higher energy scale, all these forces unify and

start behaving as a single force. It is also understood(theoretically) that *gravitational* interaction is mediated by a spin-2 particle called the *graviton*. There are experiments searching for gravitons.

At the heart of the formulation of the SM, is the concept of *symmetry* and *conserved quantum numbers*. Symmetry is the invariance of the dynamics (Lagrangian density,  $\mathcal{L}$ ), under a given transformation and a conserved quantum number is the conserved quantity associated with that transformation. In the SM, these transformations are called *local gauge* transformations or symmetry groups. The gauge transformations present in the SM can be written as:

$$SU(3)_C \otimes SU(2)_L \otimes U(1)_Y \quad (2.2)$$

$SU(3)_C$  is the local gauge transformation for strong interactions. Its conserved quantum number is the *color* ( $C$ ) charge which allows gluons to couple with quarks. There are  $3^2 - 1 = 8$  colorless and massless self interacting gluons and three different color type quarks for each quark flavor. There are eight gluons because of the  $SU(3)$  group symmetry. Anti-quarks carry opposite color charges. As previously mentioned, no free quark has been observed, rather, quarks exist in nature in the form of bound states called *hadrons*. Hadrons are made up of 2 or 3 quarks as in the case of pions and protons or neutrons respectively. Recent experiments have observe bound states consisting of 4 quarks,Ref.[3], which remain consistent with the nature of strong interactions.

$SU(2)_L \otimes U(1)_Y$  is the gauge transformation group with conserved quantum number, *weak isospin* ( $T_3$ ), necessary for the electroweak interaction. Corresponding to the  $SU(2) \otimes U(1)$  gauge group, there are  $2^2 - 1 + 1 = 4$  massless gauge bosons,  $W_\mu^{1,2,3}, B_\mu$ , capable of mixing with each other to form the physical electroweak bosons as charged  $W^\mp$  and neutral  $Z^0$  and  $\gamma$ . The  $W^\mp$  and  $Z^0$  through the spontaneous breaking of the electro-weak symmetry, obtain their mass and are the physical mass states ensuring quark flavor transformations. These bosons couple using the “charge” of the weak interaction called *weak isospin*,  $T_3$ , and the *hypercharge*,  $Y$ , to matter fields. The  $W^\mp$  only interacts with **left-handed** fermions and **right-handed** anti-fermions. This leads to a phenomenon called *parity* violation. The electromagnetic charge,  $Q$ , is the result of a combination of the third component of the weak isospin,  $T_3$  and the hyper charge,

$Y$ , through the following relation:

$$Q = T_3 + \frac{Y}{2} \quad (2.3)$$

Left handed fermions have  $T_3 = \pm \frac{1}{2}$  and are represented as *multiplets* or in this case of the SM, isospin *doublets*, while, right-handed fermions have  $T^3 = 0$  and are isospin *singlets*. We summarize fundamental particles as described by the SM in Table 2.1 showing their representations as *multiplets*(*doublets*, *triplets*, etc) and quantum numbers.

Infact, the  $SU(2)_L \otimes U(1)_Y$  guage group is a combination of two symmetry groups with coupling strengths  $g$  and  $g'$  connected to the electric charge of each fermion as  $e = g \sin \theta_w = g' \cos \theta_w$ .

The angle,  $\theta_w$ , is the *Weinberg angle*,  $\sin^2 \theta_w \approx 0.231$  is not predicted by the SM but measured from experiments. Gauge bosons can rotate from their *weak* eigen states to physically observed states using this angle.

$$W^\mp_\mu = \frac{W_\mu^1 \mp i W_\mu^2}{\sqrt{2}}, \quad \begin{pmatrix} A_\mu \\ Z_\mu \end{pmatrix} = \begin{pmatrix} \cos \theta_w & \sin \theta_w \\ -\sin \theta_w & \cos \theta_w \end{pmatrix} \begin{pmatrix} B_\mu \\ W_\mu^3 \end{pmatrix} \quad (2.4)$$

This angle also allows for the transformation of a quark from one flavor into another through the  $W^\mp$  bosons. On the contrary, according to the SM, such flavor transformation could be possible with leptons but does not lead to any possible observable effects as neutrinos are considered massless in the SM. On the contrary, recent neutrino experiments have proven otherwise as they observed mixing between different neutrino types indicating neutrinos do have mass. The transformation of quarks into different flavors is a typical interaction happening inside the core of our sun as in a nuclear reactor in the decay of neutrons to protons. The complete transformation of all quark flavors is described by the *Cabibbo-Kobayashi-Maskawa* (CKM) 3 by 3 matrix whose elements are parameters only measured from experiments and not predicted by the SM.

| Particle and Their Gauge Group Representation                      |                         |  |  |
|--|-------------------------|--|--|
| Particle Name(Symbol)  | Spin                    | Multiplet  | $SU(3)_C \otimes SU(2)_L \otimes U(1)_Y$   |
| Quarks ( $Q$ )<br>$\bar{u}$<br>$\bar{d}$<br>( $\times 3$ families) | $1/2$<br>$1/2$<br>$1/2$ | $(\mathbf{u}_L, \mathbf{d}_L)$<br>$\mathbf{u}_R^\dagger$<br>$\mathbf{d}_R^\dagger$ | $(\mathbf{3}, \mathbf{2}, \frac{1}{6})$<br>$(\bar{\mathbf{3}}, \mathbf{1}, -\frac{2}{3})$<br>$(\bar{\mathbf{3}}, \mathbf{1}, \frac{1}{3})$ |
| Leptons( $L$ )<br>$\bar{e}$<br>( $\times 3$ families)              | $1/2$<br>$1/2$          | $(\nu, \mathbf{e}_L)$<br>$\mathbf{e}_R^\dagger$                                    | $(\mathbf{1}, \mathbf{2}, -\frac{1}{2})$<br>$(\bar{\mathbf{1}}, \mathbf{1}, 1)$  |
| Higgs ( $H_u$ )<br>Higgs( $H_d$ )                                  | $0$<br>$0$              | $(\tilde{H}^+_u, \tilde{H}^0_u)$<br>$(\tilde{H}^+_d, \tilde{H}^-_d)$               | $(\mathbf{1}, \mathbf{2}, +\frac{1}{2})$<br>$(\mathbf{1}, \mathbf{2}, -\frac{1}{2})$   |
| <b>Force Carriers</b>  |                         |  |  |
| Gluons<br>(Strong Force)   | $1$                     | $\mathbf{g}$   | $(\mathbf{8}, \mathbf{1}, 0)$  |
| W bosons<br>B boson<br>(Electro-Weak Force)                        | $1$<br>$1$              | $\mathbf{W}^\pm$<br>$\mathbf{B}^0$   | $(\mathbf{1}, \mathbf{3}, 0)$<br>$(\mathbf{1}, \mathbf{1}, 0)$   |

Table 2.1: SM particles and their gauge multiplets(representation) with quantum numbers. the numbers for example  $(\mathbf{3}, \mathbf{2}, \frac{1}{6})$  means (*triplet, doublet,  $Y = 1/6$* ) representations.

### 2.1.2 Spontaneous Symmetry Breaking

It is the spontaneous breaking of the gauge transformation group:

$$SU(3)_C \otimes SU(2)_L \otimes U(1)_Y \xrightarrow{SSB \text{ into}} SU(3)_C \otimes U(1)_{QED} \quad (2.5)$$

Early attempts prior to the 1960s to construct a gauge theory of weak interactions failed because the gauge bosons were massless while experimental evidence proved otherwise. The Higgs (or Higgs-Brout-Englert) mechanism,Ref.[4], is archived by introducing a complex weak isospin *scalar doublet*,  $\phi$ , i.e spin  $s = 0\hbar$ .

During this process, the  $SU(2)_L \otimes U(1)_Y$  symmetry is spontaneously broken into a  $U(1)$  symmetry which describes electromagnetic interaction. Figure 2.1 shows a picture

of the potential of the spin-0 complex Higgs field.

The choice for the minimum value of the potential,  $|\phi_0| = \sqrt{\frac{-\mu^2}{\lambda}} = \nu$ , where  $\mu^2 < 0$  and  $\lambda > 0$ , as parameters, is to spontaneously break the  $SU(2)_L \otimes U(1)_Y$  symmetry into  $U(1)$  symmetry. In this process, both matter and gauge bosons except the photon obtain their mass. This process is referred to as *Higgs-Brout-Englert mechanism* or *Higgs mechanism*.

Quarks and leptons through their interaction with the Higgs field obtain their mass. A fermion's mass,  $m_f$ , is proportional to the strength of its interaction (Yukawa coupling  $\lambda_f$ ) with the Higgs field. Electro-weak interaction mediating gauge bosons,  $Z^0$  and  $W^\pm$  obtain their mass  $m_Z$  and  $m_{W^\pm}$  respectively, by engulfing or “*eating*” the available massless components (*Nambu-Goldstone bosons*) of the complex Higgs doublet. From the four scalar fields(complex Higgs doublet), only a physically massive *Higgs boson* remains.

$$m_f = \lambda_f \frac{\nu}{\sqrt{2}}, \quad \frac{m_{W^\pm}}{m_Z} = \frac{\frac{1}{2}\nu g}{\frac{1}{2}\nu \sqrt{g^2 + g'^2}} = \cos \theta_w \quad (2.6)$$

The search for the Higgs boson was one of the purpose for building the large hadron collider at CERN. The discovery of the Higgs candidate scalar boson through its decay into two photons,  $H \rightarrow \gamma\gamma$ , and a pair of Z bosons,  $H \rightarrow ZZ$ , was presented to the public on June 04, 2012. Its mass measured was  $m_H = 125 \pm 0.21 \text{ GeV}/c^2$ .

It is important to note that there is no fundamental reason given by the SM why there should be only one type of the Higgs field to which all fermions couple to obtain their mass nor any prediction from the SM for the choice of parameters. There are other models such as supersymmetry, which allows for the possibility of more than one Higgs field. In Figure 2.2, we show a complete summary of particles and their interactions as described by the SM.

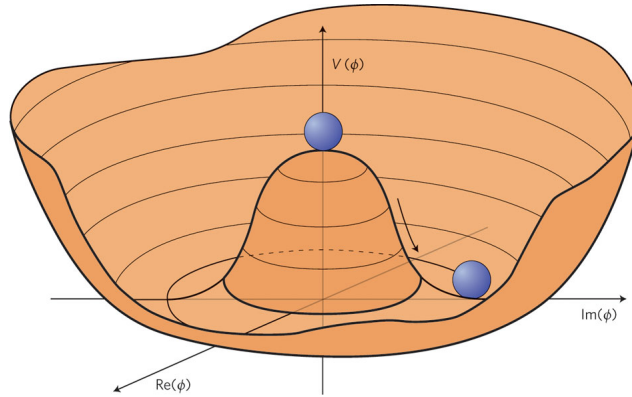


Figure 2.1: Higgs boson “Mexican hat” potential,  $V(\phi^*\phi) = \mu^2(\phi^*\phi) + \lambda(\phi^*\phi)^2$ , which leads to spontaneous symmetry breaking with choice of parameters  $\mu^2 < 0$ ,  $\lambda > 0$ .

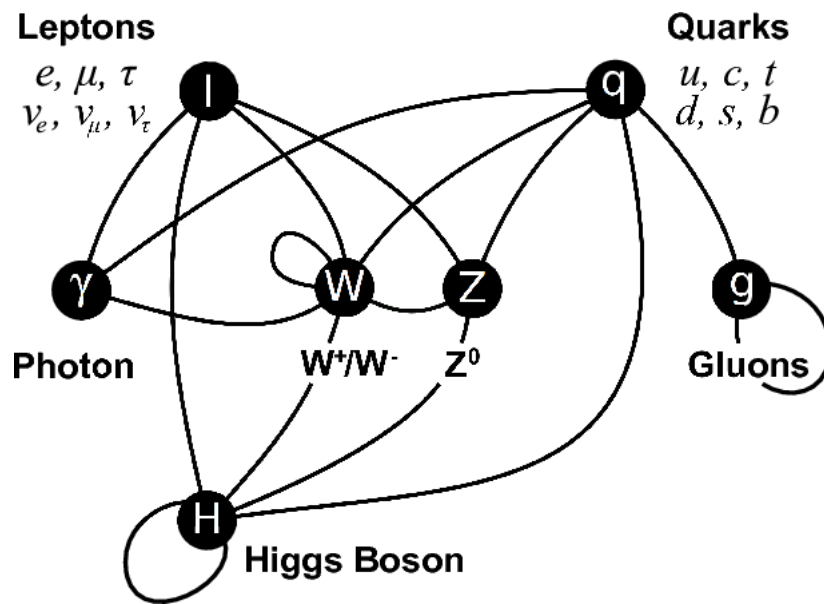


Figure 2.2: SM particles and their interactions with vector bosons as mediators.

### 2.1.3 Limitations of the Standard Model

Although numerous experiments support the SM in its description of particle properties with unmatched precision, there are many unanswered questions by the SM. We provide a summary below of those of our interest.

- **General Formalism**

Many important parameters like particle masses, Weinberg angle, the CKM matrix elements for example cannot not be derived from the SM. These are measured from experiments. Why only 3 generations of particles? Why multiplet structure of fields representation in the SM? These are questions to which the SM provides no answer.

- **Astrophysical**

Why is there so much matter than anti-matter in the universe? *Cosmic Microwave Background* (CMB) and the *Wilkinson Microwave Anisotropy Probe* (WMAP) experimental results indicate the presence of excess matter which does not interact with light called *Dark Matter* (DM) and *Dark Energy* (DE). DE is responsible for an increase energy density causing rapid acceleration expansion of the universe. The nature of DM and DE and such observations cannot be explained using the current SM.

- **Theory**

SM description of nature does not include gravitational interactions. Observation of SM coupling constants varying with energy begs the question of whether at some higher energy scale, all the weak, strong and electromagnetic coupling constants behave as one i.e unify as a single coupling constant. If possible, at what energy scale does this force unification occur?

- **Mass Hierarchy or Naturalness**

Particle masses ranges from neutrino masses, a few eV to the top particle's mass of  $173 \text{ GeV}/c^2$ . The SM does not explain this mass hierarchy. To some physicist, the energy gap between the electro-weak symmetry breaking energy scale ( $\approx 246 \text{ GeV}$ ) and the Planck energy scale (reduced Planck mass,  $M_p = 10^{18} \text{ GeV}$ ) seems unnatural.

## 2.2 Beyond Standard Model Physics

The Higgs boson mass from SM predictions include additional corrections,  $\delta m^2$ , to the higgs mass through its couplings with fermions such as that shown in figure 2.3(a). These additional corrections are given as shown in equation 2.7.

$$\delta m_f^2 = \frac{1}{16\pi^2} |\lambda_f|^2 \left( -2\Lambda^2 + 6m_f^2 \ln \left( \frac{\Lambda}{m_f} \right) + \dots \right) \quad (2.7)$$

Where  $\lambda_f$  is the Higgs to fermion coupling,  $\lambda_f H \bar{f} f$  and  $\Lambda$  is an arbitrarily large energy scale (can be of order  $10^{18}$  GeV) called the *cut-off* energy scale. As a result of this cut-off scale being very large, these corrections can also be very large. However, large corrections to the higgs boson's mass are not observed in experimental measurements of the higgs boson's mass which is only,  $m_H \approx 125$  GeV/ $c^2$ . The SM provide no explanation why these corrections are not observed.



Figure 2.3: Higgs mass contributions from its coupling to fermions (a) and scalar (b) fields.

Models beyond the SM like *supersymmetry*, provide a plausible explanation as to why these corrections are not observed in experiments. The explanations is that, there are in addition to the higgs boson being the only scalar particle in the SM, new scalar particles, yet to be observed, which can also couple to the higgs field as shown in the diagram in figure 2.3(b). These scalar coupling contribution, given in equation 2.8, unlike fermion coupling contribution, is of the opposite sign and thus cancel the fermion contribution to the higgs boson's mass. As a result cannot be observed experimentally.

$$\delta m_S^2 = \frac{1}{16\pi^2} |\lambda_S|^2 \left( \Lambda^2 - 2m_S^2 \ln \left( \frac{\Lambda}{m_S} \right) + \dots \right) \quad (2.8)$$

This problem is known as the *Hierarchy problem* and is explained using supersymmetry. This cancellation is provided at all levels of the higgs boson interaction and for whatever energy scale the cut-off value can be. Supersymmetry does not only provide an explanation to the Hierarchy problem, but also provide a good framework for the unification of fundamental forces. Supersymmetry also predicts the existence of additional particles to the SM which are non interacting with ordinary matter and having very long lifetime making these particles exceptional candidates as dark matter particles. These properties motivates the study of supersymmetry as an interesting extension of the SM for understanding physics beyond the SM (BSM).

### 2.2.1 Supersymmetry

Supersymmetry is a relativistic Quantum Field Theory (QFT), relating space-time symmetries (rotation and translation) and gauge symmetries ( $SU(3)_C \otimes SU(2)_L \otimes U(1)_Y$ ). Its breakthrough understanding resulted from the *Haag-Lapuszanski-Sohnius* theorem, Ref.[5], by Haag, Lapuszanski and Sohnius in 1975. This let to the introduction of supersymmetry generators called *Lie-superalgebra* generators,  $Q_i$ ,  $i = 1, \dots, N$ , where  $N$  is the number of supersymmetry generators, which anti-commute with the group and space-time generators. The consequence is that fermions can be transformed into bosons and vice-versa according to the equations 2.9.

$$Q|\text{Fermion}\rangle = |\text{Boson}\rangle, \quad Q|\text{Boson}\rangle = |\text{Fermion}\rangle \quad (2.9)$$

Thus, in supersymmetry, particles in a given state have the *same* mass but differ in their spin by half  $\hbar$  unit and in every irreducible representation of supersymmetry, there is an equal number of fermionic and bosonic degrees of freedom. Every particle has a supersymmetric partner with the same mass belonging to the same state representation or *supermultiplet*.

These supermultiplets are either *Chiral*, *Vector* or *Gravity* multiplets. The minimal supersymmetric extension of SM uses Chiral and Vector supermultiplets shown in Table 2.2.

| Supermultiplets | Spin in SM,   | Spin in Supersymmetry |
|-----------------|---------------|-----------------------|
| <i>Chiral</i>   | 0             | $\frac{1}{2}$         |
| <i>Chiral</i>   | $\frac{1}{2}$ | 0                     |
| <i>Vector</i>   | 1             | $\frac{1}{2}$         |
| <i>Gravity</i>  | 2             | $\frac{3}{2}$         |

Table 2.2: Supermultiplets and particle spin in SM and Supersymmetry.

Models in supersymmetry are build using *superfields*,  $\Phi$ . A given superfield consists of ordinary scalar real or complex fields ( $\phi$ ), a Lorentz vector field ( $A_\mu$ ) and Left-handed or Right-Handed Weyl(2 degrees of freedom) spinor fields ( $\psi$ ). *Chiral* and *Vector* superfields are used in constructing the minimal supersymmetric standard model. The simplest supersymmetric model is an extendsion of the SM to include supersymmetric particles with the same mass as their standard model partners. It is called the *Minimal Supersymmetric Standard Model* because it only involves the use of a single supersymmetry generator.

### 2.2.2 Minimal Supersymmetric Standard Model

In the Minimal Supersymmetric Standard Model (MSSM), the number of fundamental particles is increased. The full particle content in MSSM with this extension from SM is shown in Table 2.3 and 2.4.

The nomenclature of supersymmetric particles in derived from their SM counterparts by adding an s in front of the SM particles's name e.g a *selectron* is the supersymmetric particle of the electron, *squarks* are the supersymmetric particles of SM quarks. There are exceptions to this nomenclature which we will mentioned later. Both supersymmetry particles and their SM partners must have the same mass, however, there have been no experimental evidence for such supersymmetric particles having the same mass as SM particles. Thus, Supersymmetry is definitely not a fundamental symmetry in nature and must be broken.

| Particle Names                              | Symbol    | spin 0                       | spin 1/2                             | $SU(3)_C \otimes SU(2)_L \otimes U(1)_Y$       |
|---|-----------|------------------------------|--------------------------------------|--|
| squarks, quarks<br>( $\times 3$ families)   | $Q$       | $(\tilde{u}_L, \tilde{d}_L)$ | $(u_L, d_L)$                         | $(\mathbf{3}, \mathbf{2}, \frac{1}{6})$        |
|   | $\bar{u}$ | $\tilde{u}_R^*$              | $u_R^\dagger$                        | $(\bar{\mathbf{3}}, \mathbf{1}, -\frac{2}{3})$ |
|   | $\bar{d}$ | $\tilde{d}_R^*$              | $d_R^\dagger$                        | $(\bar{\mathbf{3}}, \mathbf{1}, \frac{1}{3})$  |
| sleptons, leptons<br>( $\times 3$ families) | $L$       | $(\tilde{\nu}, \tilde{e}_L)$ | $(\nu, e_L)$                         | $(\mathbf{1}, \mathbf{2}, -\frac{1}{2})$       |
|   | $\bar{e}$ | $\tilde{e}_R^*$              | $e_R^\dagger$                        | $(\bar{\mathbf{1}}, \mathbf{1}, 1)$            |
| higgsinos, Higgs                            | $H_u$     | $(H_u^+, H_u^\circ)$         | $(\tilde{H}_u^+, \tilde{H}_u^\circ)$ | $(\mathbf{1}, \mathbf{2}, +\frac{1}{2})$       |
|   | $H_d$     | $(H_d^\circ, H_d^-)$         | $(\tilde{H}_d^\circ, \tilde{H}_d^-)$ | $(\mathbf{1}, \mathbf{2}, -\frac{1}{2})$       |

Table 2.3: Chiral supermultiplets and representation in Minimal Supersymmetric SM (MSSM). Super symmetric particles (sparticles) have a  $\sim$  on them. Spin -0 fields are complex scalars while spin-1/2 fields are left-handed two component Weyl fermions.

| Particle Names    | spin 1/2                         | spin 1           | $SU(3)_C \otimes SU(2)_L \otimes U(1)_Y$ |
|-------------------|----------------------------------|------------------|--|
| gluino, gluon     | $\tilde{g}$                      | $g$              | $(\mathbf{8}, \mathbf{1}, 0)$            |
| winos, $W$ bosons | $\tilde{W}^\pm, \tilde{W}^\circ$ | $W^\pm, W^\circ$ | $(\mathbf{1}, \mathbf{3}, 0)$            |
| bino, $B$ boson   | $\tilde{B}^\circ$                | $B^\circ$        | $(\mathbf{1}, \mathbf{1}, 0)$            |

Table 2.4: Gauge supermultiplets and representation in Minimal Supersymmetric SM (MSSM). Super symmetric particles (sparticles) have a  $\sim$  on them.

In a similar fashion to the Higgs mechanism, supersymmetry breaking is also spontaneous. One of the ways in which supersymmetry is broken is through gauge interactions. Supersymmetric models build using such supersymmetry breaking are called *Gauge Mediated Supersymmetry Breaking* (GMSB) models. These models are interesting because they allow for only 5 fundamental parameters and provide phenomenological consequences like provides candidate dark matter particles.

Supersymmetry breaking is realized in each model through a *superpotential* and the breaking defines the phenomenology and particle mass spectrum. In MSSM, eqn 2.10, shows the interaction of particles and Higgs bosons through this superpotential.

$$W_{\text{mssm}} = \bar{u}\mathbf{y_u}QH_u - \bar{d}\mathbf{y_d}QH_d - \bar{e}\mathbf{y_e}LH_d - \mu H_dH_u \quad (2.10)$$

The objects  $H_u$ ,  $H_d$ ,  $Q$ ,  $L$ ,  $\bar{u}$ ,  $\bar{d}$ ,  $\bar{e}$  are chiral superfields of the chiral supermultiplets given in Table 2.3 above.

The dimensionless couplings  $\mathbf{y_u}, \mathbf{y_d}, \mathbf{y_e}$  are  $3 \times 3$  matrices of the Yukawa couplings. Rather than a single Higgs *doublet* in the SM, supersymmetry breaking requires two Higgs doublets;  $H_u$  and  $H_d$ . They give mass to **up-type** and **down-type** quarks and leptons respectively. The superpartners of these Higgses are fermions and those of the gauge bosons called *gauginos* mix to produce new neutral and charged fermions called *Neutralinos* and *Charginos* respectively. In order for GMSB models to agree with experiments in the prediction of the proton lifetime  $> 10^{32}$  years, an additional symmetry relating the quarks ad leptons through the *baryon* ( $B$ ) and *lepton* numbers ( $L$ ) symmetries called *R-Parity* or *Matter Parity* is introduced. R-parity is defined as;  $R_P = (-1)^{3(B-L)+2S}$  with  $S$  being the spin of the particle. SM particles like quarks have an *even* R-parity,  $R_P = 1$ , while supersymmetry particles like squarks have odd parity  $R_P = -1$ . The phenomenological consequence of R-parity is that, first, in the decay of supersymmetry particles, the lightest SUSY particle (LSP) have odd parity  $R_P = -1$  and is thus considered absolutely stable. Second, every supersymmetry particle produced and is not the LSP, will eventually decay into the LSP or an odd number of LSPs. Third, supersymmetry particles can only be produced in pairs in a collider experiment. If in addition to being stable, the LSP is neutral and interacts only very weakly with ordinary matter, then this makes it a good candidate for non-baryonic dark matter as required by cosmology, Ref. [6],[7], [8].

Models with the condition of conserving R-parity are called *R-parity Conserving* (RPC) models with the LSP stable while those without the condition of R-parity being conserved are called *R-parity Violating* (RPV) models. In RPV models the LSP is unstable and decays to SM particles. A simplified version of GMSB models studied in this thesis is the *Snowmass Point and Slopes* (SPS8), Ref.[9], models whose phenomenology predictions is within the reach of the large hadron collider. It is possible to produce supersymmetry particles with mass of about a few TeV at the large hadron collider (LHC).

Figure 2.4 shows the supersymmetry particle mass spectrum for particles within the SPS8 model also known as the minimal GMSB (mGMSB).

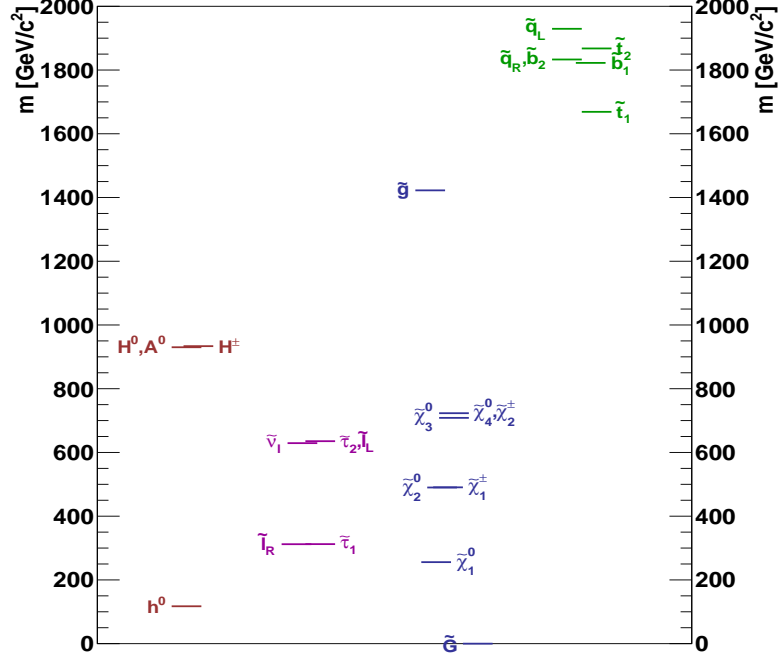


Figure 2.4: Supersymmetry particle mass spectra in the SPS8 or minimal GMSB (mGMSB) model.

In summary, MSSM in addition to SM particles, contains new particles whose spin (S) differ from their SM counterparts by half-integer. Bosons (fermions) in the SM have superpartners which are fermions (bosons). The superpartners of SM fermions are scalars called *sfermions* ( $\tilde{l}$ ), sneutrinos ( $\tilde{\nu}$ ) and squarks ( $\tilde{q}$ ) while *gluinos* ( $\tilde{g}$ ) being fermions are the superpartners of the massless gauge bosons of strong interaction, gluons. The scalar Higgs (2 needed) bosons and the vector gauge bosons of Electro-Weak interaction have fermionic superpartners called *higgsinos*, *Winos* and *Binos*. These can mix to form a pair of mass eigenstates called *charginos* ( $\tilde{\chi}_j^\pm, j = 1, 2$ ) i.e  $\tilde{\chi}_{1,2}^\pm$  is a from mixing  $\tilde{W}^+, \tilde{W}^-, \tilde{H}^+, \tilde{H}^-$  and a quartet of mass eigenstates called *neutralinos* ( $\tilde{\chi}_i^0, i = 1, \dots, 4$ ), i.e  $\tilde{\chi}_{1-4}^0$  is from mixing  $\tilde{B}^0, \tilde{W}^0, \tilde{h}^0, \tilde{H}^0$ .

### 2.3 Gauge Mediated Supersymmetry Breaking Models

GMSB models have 5 main parameters:

$$\{\Lambda, M_{\text{mess}}, N_5, \tan(\beta), \text{sgn}(\mu), C_{\text{grav}}\} \quad (2.11)$$

where  $\Lambda$  is the effective supersymmetry breaking scale,  $\mathbf{M}_{\text{mess}}$  is the mass of the messenger particle involved in mediating supersymmetry breaking to the MSSM energy scale,  $\mathbf{N}_5$  is the number of messenger particles. The other parameters,  $\tan \beta$  and  $\text{sgn}(\mu)$  are related to the two Higgs bosons necessary for supersymmetry breaking with  $\tan \beta$  being the ratio of the vacuum expectation values for both Higgs bosons. The sign of the Higgs potential is defined by  $\text{sgn}(\mu)$ . In these models, the gravitino can become very light with its mass bounded only by cosmological observations and as such is identified as the least stable supersymmetry particle (LSP). The mass of the gravitino is expressed in terms of the parameter  $C_{\text{grav}}$  according to equation 2.12.

$$m_{\tilde{G}} = C_{\text{grav}} \cdot \frac{\Lambda \mathbf{M}_{\text{mess}}}{\sqrt{3} M_{pl}} \quad (2.12)$$

where  $M_{Pl} = 1.3 \times 10^{19}$  GeV. This means,  $C_{\text{grav}}$  is a scaling parameter, which determines the lifetime of the Next-to-Lightest-Supersymmetry particle (NLSP) as its decay rate to the gravitino will depend on its mass difference with the gravitino.

### 2.3.1 Phenomenology

Light gravitinos with unique gravitino-scalar-chiral fermion and gravitino-gaugino-gauge boson interactions shown in figure 2.5 in GMSB models allow for the gravitino mass to be as low as a few eV and up to an upper bounded for them to provide the right amount of dark matter observed in the early universe. In addition to this, being neutral and stable makes them an excellent candidate particle for dark matter.

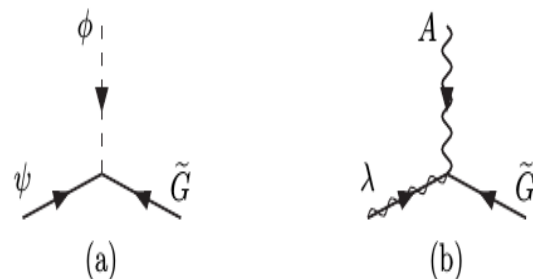


Figure 2.5: Feynman diagrams of gravitino/golstino,  $\tilde{G}$ , gaugino and scalar interactions with superpartner pairs  $(\psi, \phi)$  scalar (a) and  $(\lambda, A)$  gaugino (b) decay to gravitino.

The decay of the NLSP to the gravitino as LSP is always accompanied by the SM partner of the LSP, so as to conserve R-Parity. Thus if  $\tilde{p}$  is the NLSP, it decay to gravitino and SM particle  $p$ ,  $\tilde{p} \rightarrow p + \tilde{G}$ . In the SPS8 benchmark model, the choice of parameters is as follows:  $\mathbf{M}_{\text{mess}} = 2\Lambda$ ,  $\tan(\beta) = 15$ ,  $\mathbf{N}_5 = 1$ . Only  $\Lambda$  and  $C_{\text{grav}}$  are allowed to vary, Ref.[9]. The gravitino ( $\tilde{G}$ ), is the LSP. The NLSP,  $\tilde{p}$ , is the lightest neutralino ( $\tilde{\chi}_1^0$ ). There are four types of neutralinos which are a mixture of the supersymmetric particles Bino ( $\tilde{B}^\circ$ ), Wino ( $\tilde{W}^\circ$ ), higgsino ( $\tilde{H}_u^\circ, \tilde{H}_d^\circ$ ), depending on the choice of parameters  $\Lambda$ ,  $\tan\beta$ , and  $\text{sgn}(\mu)$ . The particle  $p$  could be a photon ( $\gamma$ ), Z boson ( $Z$ ) (or  $Z'$ ) and a higgs boson ( $h$ ). This thesis, for experimental convenience, will focus on the parameter space for which the the particle  $p$  is a photon ( $\gamma$ ) and  $C_{\text{grav}} > 1$ . This ensures that the lifetime of the NLSP is long enough such that its decay happens within the detector volume and the resulting photon is delayed or non-prompt on length scales of size of the detector. The decay rate for a NLSP to its SM partner and a gravitino can be approximated using only the mass of the NLSP and the effective supersymmetry breaking scale,  $\mathbf{F} = C_{\text{grav}} \cdot \Lambda \cdot \mathbf{M}_{\text{mess}}$  giving in equation 2.13.

$$\Gamma(N\tilde{LSP} \rightarrow \gamma\tilde{G}) \approx \frac{m_{NLSP}^5}{\mathbf{F}^4} \quad (2.13)$$

This approximation is almost the same for the non-minimal GMSB models except that additional parameters are present showing explicit dependence of the neutralino life time on neutralino mixing.

### 2.3.2 Long-Lived Particles in GMSB Models

Measuring a particle's life time or distance travelled before it decays can be a useful method to uncover new fundamental interactions. As the lifetime is related to the decay rate which is determine by the particles interactions and available energy space.

#### Production of supersymmetric particles at Hadron Colliders

The production of a particle in a particle collider is a probabilistic process. This probability is expressed as a measurable quantity called *cross section*. For example, the cross section of producing a particle in proton-proton collider such as the LHC, is the

probability that the proton beams will collide and interact in a certain way to produce that particle. Although this cross section ( $\sigma$ ) is measured in units of area as *barns* ( $1b = 10^{-24} \text{ cm}^2$ ), usually it has very little relation to the physical interpretation of area as used in everyday life. It is rather a technical term for counting the number of the particle produced when these proton beams collide. The cross section of producing the particle depends on the available energy of the proton beams compared to the mass of the particle, the nature of the interactions of the proton beams when colliding which in turn depends on the coupling constants and the flux of the proton beams. The rate or number per unit time of the particle produced at a specific particle collider is given as a product of its cross section times the instantaneous luminosity ( $\mathcal{L}$ ). The instantaneous luminosity is the number of incident particles per unit area per unit time times the opacity of the target. The typical cross section of producing a supersymmetry particle at the LHC is of the order of  $1 \text{ pb} = 10^{-12} \times 10^{-24} \text{ cm}^2$  or at times  $1 \text{ fb} = 10^{-15} \times 10^{-24} \text{ cm}^2$  for extremely rare SUSY processes. While that for a standard model process like the production of the Z or  $W^\pm$  bosons is of the order of a few  $nb = 10^{-9} \times 10^{-24} \text{ cm}^2$ . This makes the search for a supersymmetry particle in an environment like as the LHC is very challenging.

Producing a supersymmetry particle at a hadron collider like the LHC depends on the mass of supersymmetry particles. The mass of supersymmetry particles is much higher than those of SM particles and as a result, the cross section for producing supersymmetry particles at a hadron collider is much smaller compared to that for SM particles. The cross section of a given process in supersymmetry (SUSY) happening at the particle collider can be computed and compared with experimental measurements. This cross section depends on the type of processes involved. Each process can be expressed in diagrammatic forms called *feynman* diagrams and its probability of happening computed using these feynman diagrams. Supersymmetry processes that can lead to the production and decay of neutralino ( $\tilde{\chi}_1^0$ ), at a proton collider like the LHC can involve electro-weak and strong interactions. The production of supersymmetry particles in strong interactions have larger cross sections compared to electro-weak processes. This a because, the LHC being a proton-proton collider is mostly a strong interaction production process. The cross section for the production of supersymmetry particles of a given mass is shown in figure 2.6. As seen from the figure, production

of supersymmetry through strong interaction process like  $pp \rightarrow \tilde{g}\tilde{g}$ ,  $\tilde{q}\tilde{q}$  dominates over electro-weak interactions like  $pp \rightarrow \tilde{\chi}^\pm\tilde{\chi}^\mp, \tilde{\chi}^0\tilde{\chi}^\pm$ .

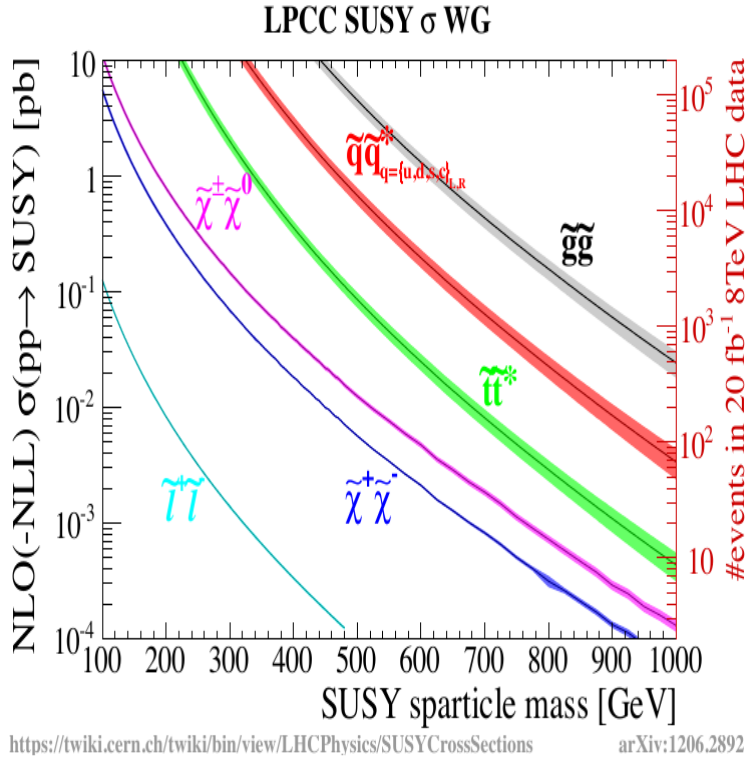


Figure 2.6: Supersymmetry production cross-section against sparticle mass for different modes of supersymmetry production at a proton-proton collider.  $pp \rightarrow \tilde{g}\tilde{g}$  processes have the dominant production cross section.

Since the production of neutralino through produce neutralinos through  $pp \rightarrow \tilde{g}\tilde{g}, \tilde{q}\tilde{q}$  process is dominant, we will focus only on these. The p neutralino is produced from the production and subsequent decay of massive supersymmetry particles like squarks ( $\tilde{q}$ ) and gluinos ( $\tilde{g}$ ). This is as *indirect* or *cascade decay* production of neutralinos. The feynman diagram for process,  $pp \rightarrow \tilde{g}\tilde{g}, \tilde{q}\tilde{q}^*$ , are shown in figure 2.7. The produced squarks and gluinos do not directly decay into gravitinos but through neutralinos and eventually to gravitinos because their coupling to the gravitinos is not possible. This is due to the fact that in GMSB models, there are no gravitino-gluino-gauge boson or gravitino-squark-gauge boson couplings but rather gravitino-gaugino-gauge boson or gravitino-scalar-chiral fermion interactions.

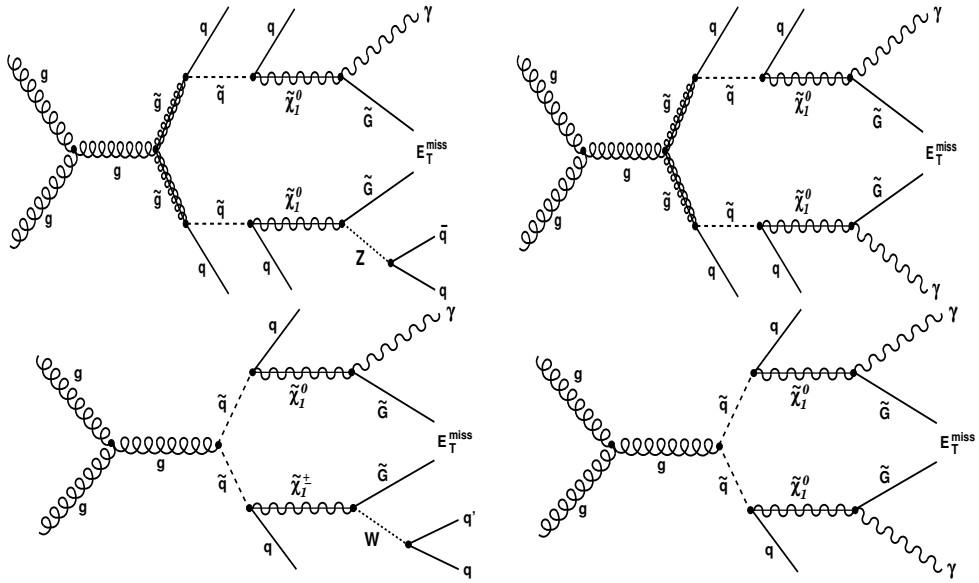


Figure 2.7: Feynman diagrams for gluino single (top left) and double (top right) photon and squarks single (bottom left) and double (bottom right) photon production from cascade decays of gluino and squark at LHC.

### Particle Decay Rate

When a particle is produced, say particle **A**, its coupling to other particles, say particles **B<sub>1</sub>** … **B<sub>n</sub>**, where  $n$  is total number of particles particle, allows for it to transform into these other particles. In addition its coupling, if the mass of particle **A** is greater than the total sum of mass of particles **B<sub>1</sub>** … **B<sub>n</sub>**, i.e  $m_A > m_{B_1} + \dots + m_{B_n}$ , then we say, particle **A** *decays* to particles **B<sub>1</sub>** … **B<sub>n</sub>**. Particle for which no such channel for decay is possible are termed *stable*. Our current understanding is that only the electron (e) and the proton (p) are stable( although there are theories which predict the proton to decay after  $10^{34}$  years and also theories where stable heavy or light particles will explain the nature of Dark Matter. This time through which a particle must live before it decays is called it's *lifetime*. Particle decays in which the particle decays instantly as soon as they are produced are called *prompt* decays while particle decays with observable lifetime are *non-prompt* decays. Non-prompt decays might range from a few fraction of a second lifetimes in *nanoseconds* ( $1 \text{ ns} = 10^{-9} \text{ s}$ ) to a few minutes. At particle detector length or size scales(of the order of a few minutes), such particles are termed *long-live*. In

particle decay, the stronger the *coupling* and the larger the *mass difference*, the faster the decay. This is expressed mathematically as;  $N(t) = N(0)e^{-t/\tau}$ , where both  $N(t)$  and  $N(0)$  are the number of the particle present at time  $t$  and the beginning,  $t = 0$  and  $\tau$  is the particle's *lifetime*.

The rate at which a particle decays is its *decay rate* ( $\Gamma$ ). Particle decay rate depends on the availability of other particles it couples to and with mass less than the particle's mass. It is therefore possible that a given particle, **A** would rather decay to other particles **C<sub>1</sub>** … **C<sub>n</sub>** preferred to if its coupling to these and mass condition is satisfied. The decay into a specific set of particle(s) or *decay channel* can be express as a ratio of its total decay rate to all particles possible. This ratio is called *branching ratio* (BR). Decay rate, ( $\Gamma$ ) is related to lifetime,  $\tau$  according to expression 2.14.

The inverse of a decay rate is the *proper life time*, denoted as  $\tau$ .

$$\tau = \frac{\hbar}{\Gamma} \quad (2.14)$$

$\tau$  is the particle's lifetime where the particle is not moving. It is convenient to express lifetime in terms of its distance traveled before it decays. This distance is expressed as  $c\tau$ , where  $c$  is the speed of light in vacuum. Since most particles have mass and travel with velocity  $\vec{v}$  not equal to  $c$ , this distance travel considering  $|\vec{v}| \neq c$  is fully expressed using equation 2.15.

$$\vec{L} = \vec{\beta}\gamma c\tau \quad (2.15)$$

where  $\vec{\beta} = \frac{\vec{v}}{c}$ ,  $\vec{v}$  is the particle's traveling velocity and  $\gamma = \frac{1}{\sqrt{1 - \frac{v^2}{c^2}}}$  is a factor relating the motion when it is not moving (rest frame) to a frame where it is moving. Equation 2.15 can also be expressed in as  $\vec{L} = \frac{\vec{p}}{m}c\tau$ , in terms of the particle's momentum  $p$  and mass,  $m$ . Particles with larger mass and produced with a small momentum travel slow and thus might have large distance traveled before it decays. Since decay rate,  $\Gamma$ , depends on the coupling, particle decaying through electromagnetic, weak and strong interactions have very different decay rates. Particles decaying through strong interactions have the largest decay rate and thus shortest lifetime of about  $10^{-17}$  to  $10^{-25}$  seconds.

Particle lifetime may vary from a few femtoseconds ( $1 \text{ fs} = 10^{-15} \text{ s}$ ) to the age of the universe or equivalently its measured distance travelled may vary from a few  $\mu\text{m}$  to billions of km, Ref.[10, 11]. The term *long-lived* particles to refer to particles whose

distance traveled might range from a few  $\mu\text{m}$  to few meters or within the detectable size of an LHC particle detector.

### Neutralino as a Long-Lived Particle

Neutralino being the next-to-lightest-supersymmetry particle (NLSP) decays to a photon ( $\gamma$ ) or Z boson and gravitino ( $\tilde{G}$ ), Ref.[12, 13]. The probability for a neutralino ( $\tilde{\chi}_1^0$ ), produced with energy  $E_{\tilde{\chi}_1^0}$  and mass  $m_{\tilde{\chi}_1^0}$  to travel a distance  $x$  before decaying to a photon and gravitino in the laboratory frame can be expressed as shown in equation 2.16.

$$\mathcal{P}(x) = 1 - \exp\left(-\frac{x}{L}\right) \quad (2.16)$$

where

$$L = \left(c\tau_{\tilde{\chi}_1^0}\right) \cdot (\beta\gamma)_{\tilde{\chi}_1^0} \quad (2.17)$$

Equation 2.17 represents the decay length of the neutralino particle as measured in a particle detector. It depends on two main factors. The boost factor,  $(\beta\gamma)_{\tilde{\chi}_1^0} = \frac{|\vec{p}_{\tilde{\chi}_1^0}|}{m_{\tilde{\chi}_1^0}} = \sqrt{\left(\frac{E_{\tilde{\chi}_1^0}}{m_{\tilde{\chi}_1^0}}\right)^2 - 1}$ , which indicates how fast the neutralino is traveling before it decays. For slow moving neutralino,  $(\beta\gamma)_{\tilde{\chi}_1^0} \ll 1$ . would require This means that neutralino momentum ( $p_{\tilde{\chi}_1^0}$ ) at production from gluino or squarks decays must be much smaller than the neutralino mass,  $m_{\tilde{\chi}_1^0}$ . Therefore the neutralino is said to be a slow neutralino if the ratio,  $p_{\tilde{\chi}_1^0}/m_{\tilde{\chi}_1^0} \ll 1$ . Slow neutralinos are good candidates for detectable long-lived neutralinos. Thus, slow moving neutralino, whose ratio,  $p_{\tilde{\chi}_1^0}/m_{\tilde{\chi}_1^0} \ll 1$  will be good candidates for detectable long-lived neutralinos. The other factor is the inherent long lifetime,  $c\tau_{\tilde{\chi}_1^0}$ , of the neutralino. Neutralinos with  $c\tau_{\tilde{\chi}_1^0} > 1$  are long-lived and would make good candidates for detectable long-lived neutralinos. This inherent neutralino lifetime can be expressed as given in equation 2.18.

$$c\tau_{\tilde{\chi}_1^0} \approx \left(\frac{m_{\tilde{\chi}_1^0}}{\text{GeV}}\right)^{-5} \left(\frac{\sqrt{\mathbf{F}}}{\text{TeV}}\right)^4 \quad (2.18)$$

$$c\tau_{\tilde{\chi}_1^0} \approx C_{grav}^2 \left(\frac{m_{\tilde{\chi}_1^0}}{\text{GeV}}\right)^{-5} \left(\frac{\sqrt{\mathbf{\Lambda} \cdot \mathbf{M}_{mess}}}{\text{TeV}}\right)^4 \quad (2.19)$$

It is important to note that by changing the supersymmetry breaking scale,  $\mathbf{F}$ , the

lifetime of the neutralino also changes. In the SPS8 model, the parameter  $C_{grav}$  is used to adjust the inherent lifetime of the neutralino. Thus, we re-write the neutralino lifetime as given in equation 2.19. This equation is used to simulate physics events with the production and decay of neutralino in CMS detector using Monte Carlo (MC) simulations. The supersymmetry breaking scale  $\Lambda$  determines the mass of gluino ( $\tilde{g}$ ), squarks ( $\tilde{q}$ ) which decay to the neutralino. Therefore the neutralino momentum,  $p_{\tilde{\chi}_1^0}$  is determined by the masses of gluino and squarks. If the gluino or squark decays to the neutralino in association with a many gluons and quarks seen in the detector as *jets*, then the neutralino momentum is small with the ratio  $p_{\tilde{\chi}_1^0}/m_{\tilde{\chi}_1^0} \ll 1$ , this means the neutralino is slow and therefore long-lived. However, if the gluino or squark is decays with less number of jets, then the neutralino momentum is not so small and the neutralino is not very long-lived. Therefore, the neutralino kinematic properties like its momentum, arrival time at the CMS detector as well as the number of associated jets can be influenced by the gluino or squark decay kinematics.

Using the LHC as the proton-proton collider and the CMS detector as the instrument for detecting and measuring the lifetime of delayed photons produced from long-lived neutralino decays. We have simulated neutralino production and decay according to the SPS8 benchmark model, where the neutralino is the NLSP decaying into a photon and the gravitino as LSP. In Figure 2.8 we show some distributions of kinematic properties like the momentum in the transverse plane of the CMS detector (transverse momentum ( $p_T$ ), since particles produced with enough momentum travel and are detected along the transverse plane of the CMS detector) of the neutralino ( $p_T^{\tilde{\chi}_1^0}$ ) and its measured lifetime ( $c\tau_{\tilde{\chi}_1^0}$ ) in the CMS detector. We also made distribution showing transverse momentum of the photon ( $p_T^\gamma$ ) and the measured arrival time of the photon ( $T_\gamma$ ). These distributions are made for different model parameters  $\Lambda$  and  $C_{grav}$ . The CMS Software (CMSSW) package has been used to simulate and study the neutralino production and decay in CMS detector while the root data analysis framework was used to performed some fit analysis on the generated and simulated distributions of the distance traveled by neutralino before decay to extract its  $c\tau_{\tilde{\chi}_1^0}$  produced during the MC generation. The extracted  $c\tau_{\tilde{\chi}_1^0}$  value is compared to theoretical prediction values for consistency check of the simulation process.

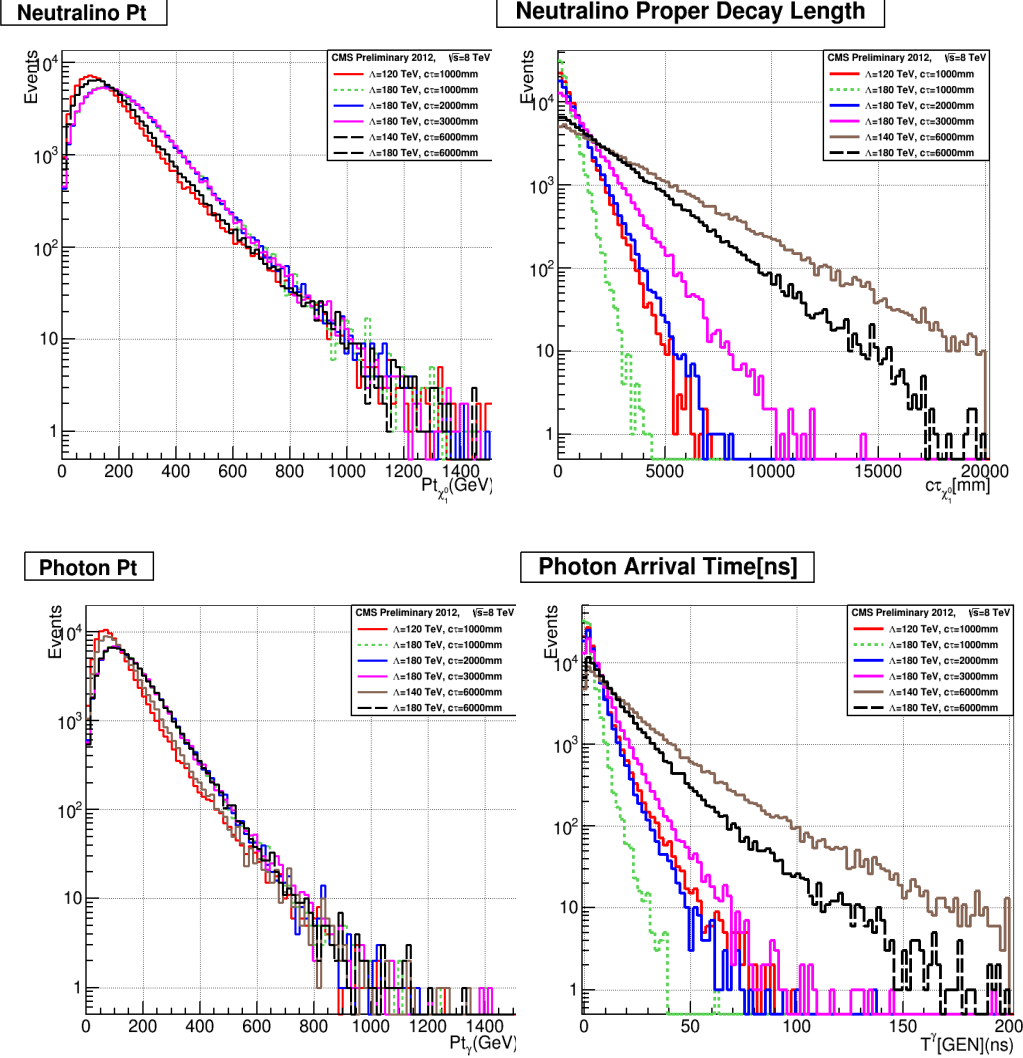


Figure 2.8: Neutralino transverse momentum distribution (top left) and proper decay length (top right) with its decayed photon transverse momentum distribution (bottom left) and time of arrival at ECAL (Bottom right) for GMSB SPS8 model.

## 2.4 Previous Search Experiments

The have been previously other search experiments for neutral long-live particles decaying to photons. Obviously, negative findings from these experiments led to possible

search exclusion regions in terms of the lifetime, mass and cross section of the existence of supersymmetry particles in different supersymmetry models. Results from experiments(DO, CDF, CMS and ATLAS), Ref.[14, 15, 16, 17, 18] of the search for Neutralino NLSP decaying to photon and gravitino interpreted using the SPS8 benchmark model is shown in 2.9. These results show that within the SPS8 model, neutralinos with mass  $m_{\tilde{\chi}_1^0} \leq 245$  GeV and proper decay length  $c\tau_{\tilde{\chi}_1^0} \leq 6000$  mm have not been found at hadron colliders. The diagram on the left of figure 2.9 are exclusion results in the neutralino mass or supersymmetry breaking scale  $\Lambda$  on the horizontal axis and the neutralino lifetime,  $c\tau_{\tilde{\chi}_1^0}$  on the vertical axis from the 7 TeV search analysis by the ATLAS experiment while the diagram on the right is that for CMS experiment. The colored regions on the plots shows the parameter space where these searches have been performed and the findings were negative.

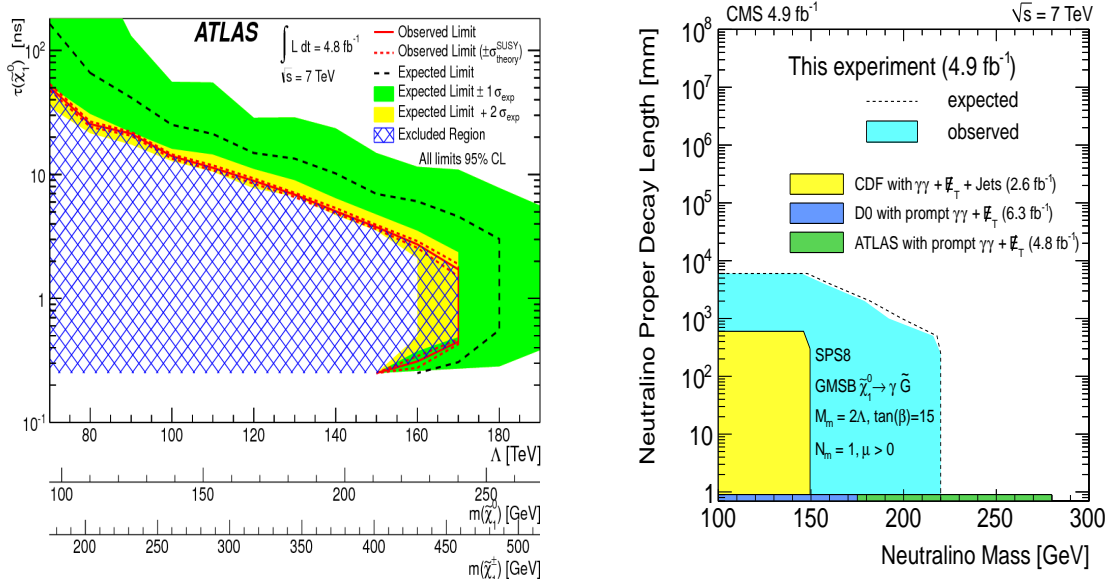


Figure 2.9: Neutralino lifetime and mass upper limit from ATLAS(left) and CMS(right) 7 TeV analysis with non-pointing photons and MET.

## Chapter 3

# Hadron Collider and Detector

This section describes the particle collider and detector. The first section describes the particle accelerator which is the Large Hadron Collider (LHC) and the next section describes the Compact Muon Solenoid (CMS) detector with emphasis to those sections directly relevant to this analysis. A detailed description of the LHC and CMS detector is found in Ref.[19] and Ref.[20].

### 3.1 Large Hadron Collider

#### 3.1.1 Overview

The LHC is a proton-proton and heavy ion collider designed to achieve a center of mass  $\sqrt{S}$  energy of 14 TeV. It is hosted by the European Organisation for Nuclear Research (CERN). Unlike linear colliders, the LHC is a circular collider with nearly 27 km in circumference located at the border between France and Switzerland. It is designed to smash protons and ions against each other controlled by powerful magnets at four main points. The Compact Muon Solenoid (CMS) is one of the multi-purpose particle detectors at each collision point. Fig. 3.1 shows the LHC and the different stages before particle collision.

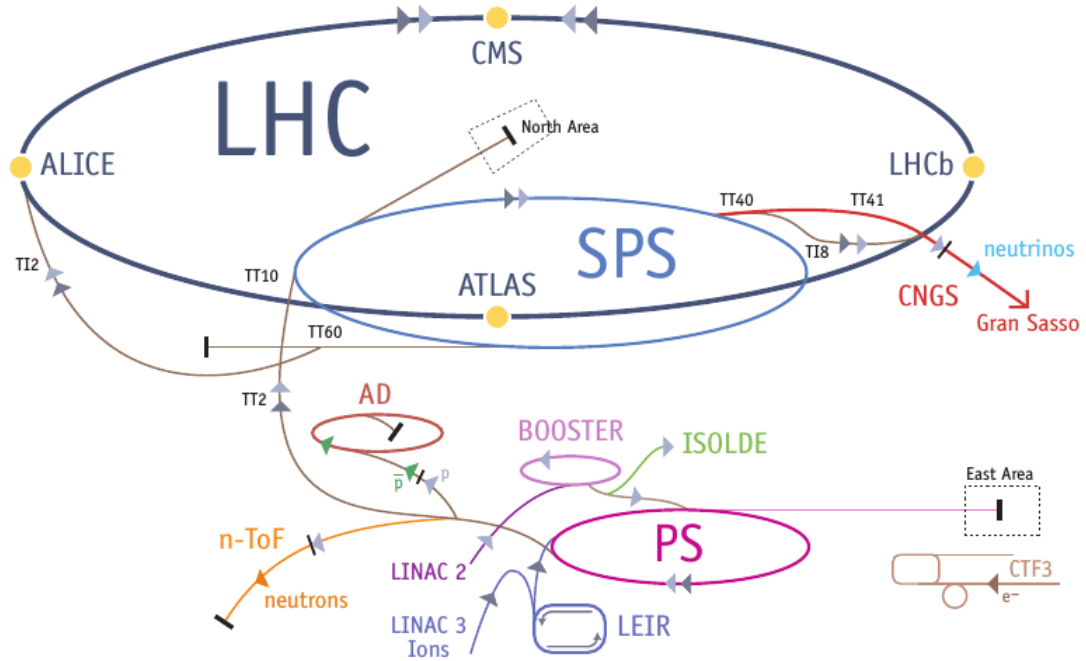


Figure 3.1: Schematic diagram showing the full Large hadron Collider.

### 3.1.2 Colliding Energy

Hydrogen ions also known as protons from hydrogen gass where the orbiting electron has been striped away is inserted into a linear accelerator called *Linac 2*. Using electromagnetic fields in Radio Frequency (RF) cavities, these protons are accelerated to an energy of 50 MeV creating a stream of particles called *particle beams* arranged in packets known as *bunches*. Protons from the Linac2 are injected into the circular synchrotron Booster (PSB). The circular synchrotron accelerator ensures that the protons pass many times through a cavity with their energy slowly increasing each time to reach the design energy. The PSB accelerates the protons up to 1.4 GeV and inject them into the Proton Synchrotron (PS) which increases their energy to 25 GeV. These protons traveling at 99.93% the speed of light are sent to the Super Proton Synchrotron (SPS) and accelerated to an energy of 450 GeV. They are finally transferred into the LHC ring(accelerating in a clockwise and anti-clockwise direction) and accelerated for about 20 minutes to their nominal energy of 7 TeV. By now the protons are traveling with the

speed of 99.9999% the speed of light. Powerful bending magnets are used to keep the beams traveling in the circular LHC ring. The advantage of circular particle colliders over fix target is that, the energy available to make new particles called the *center of mass* (COM) energy, denoted as  $\sqrt{S}$  is simply the sum of the energy of the two beams i.e.  $\sqrt{S} = E_{\text{beam1}} + E_{\text{beam2}}$  compared to  $\sqrt{E_{\text{beam}}}$  for fix target experiments. For the LHC, each beam is designed to have energy of 7 TeV making  $\sqrt{S} = 14$  TeV. In circular colliders, synchrotron radiation (is inversely proportional to the mass of the charge particle to the fourth power) by an accelerating charge particle contributing to loss its energy. This would require a continuous addition of energy after each turn to maintain the beam energy to a stable value. However, since the proton's mass is about 0.938 GeV, and are to be accelerated to about 7 TeV, this loss of energy is not very significant unlike for electrons whose mass is about 0.000511 GeV and the energy loss is more. Thus protons are preferred to electrons for a circular collider. Then again, the debris of particles produced when electrons collide is much less compared to that of protons making analysis in a hadron collider very challenging.

### 3.1.3 Luminosity

In colliding beams experiments, the center of mass energy available for the production of new effects is very important. However, the number of useful interactions producing effects (events) is equally important, especially in cases where the probability (also known as cross section,  $\sigma$ ) of producing rare events is very small. The quantity which measures the ability of a particle accelerator to produce the events from the required number of interactions is called *luminosity*. The luminosity is also the proportionality factor between the number of events per second and the cross section. Luminosity ( $\mathcal{L}$ ) is therefore a measure of the number of collisions that can be produced in a collider per squared area per second. The cross section is calculated from theory while the luminosity depends on factors ranging from the flux i.e. number of particles per second of the beams, the beam sizes at collision, and the frequency of collision. For physics experiments, the integrated luminosity which is total luminosity over a given period of time usually a year gives the amount of data that has been recorded by a given detector.

Using the luminosity ( $\mathcal{L}$ ) and the cross section ( $\sigma_p$ ) of a given process, we can calculate event rate ( $\mathcal{R}$ ) or the number of events per second produced in proton collisions

by the given interaction process. By calculating the event rate, we are measuring a given cross section ( $\sigma_p$ ) through  $(\sigma_p = \frac{\mathcal{R}}{\mathcal{L}}$  in order to prove or disprove theories which make prediction on  $\sigma_p$ .

$$\mathcal{R} = \mathcal{L} \cdot \sigma_p \quad (3.1)$$

In CMS we have a “recorded” and “delivered” luminosity. Delivered luminosity refers to the luminosity delivered by LHC to CMS and one would expect this to be equal to the amount recorded. However, there are instances where the CMS detector is unable to take data either because the data acquisition chain (DAC) or one of the CMS sub-detectors is temporarily down and also trigger dead time. Figure 3.2 shows the total integrated luminosity delivered by LHC and recorded using the CMS detector during the 8 TeV proton-proton collision by the LHC.

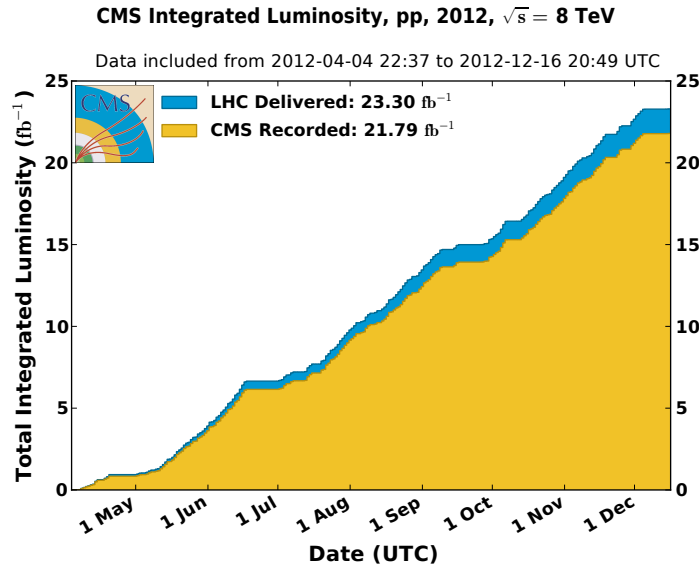


Figure 3.2: Cumulative luminosity versus day delivered to (blue), and recorded by CMS (orange) during stable beams and for p-p collisions at 8 TeV center-of-mass energy in 2012.

### 3.1.4 LHC Bunch Structure

Each LHC proton bunch is placed inside an RF buckets during beam filling. The filling scheme is such that not all RF buckets have proton bunches. Those empty buckets or beam gaps are necessary to avoid parasitic collision near IP and to make room for beam

dump and beam halos known as beam cleaning. The separation in time between two buckets/bunches filled or unfilled is approximately 2.5 ns. There are about  $10^{11}$  protons per bunch during filling and acceleration. However, during filling and eventual bunch splitting at PS, it is possible that some empty buckets are filled with a much smaller proton population compared to the main bunch. These buckets with few protons can be either trailing the main bunch by  $\Delta t = 2.5, 5.0, 7.5, \dots$  ns, or leading the main bunch by  $\Delta t = -2.5, -5.0, -7.5, \dots$  ns. If these less populated bunches are 2.5 to 3.0 ns spaced in time from each other, they are referred to as *satellite* bunches and if 5.0 ns, they are referred to as *ghost* bunches. Figure 3.3 shows ghost and satellite bunches and a main proton bunch.

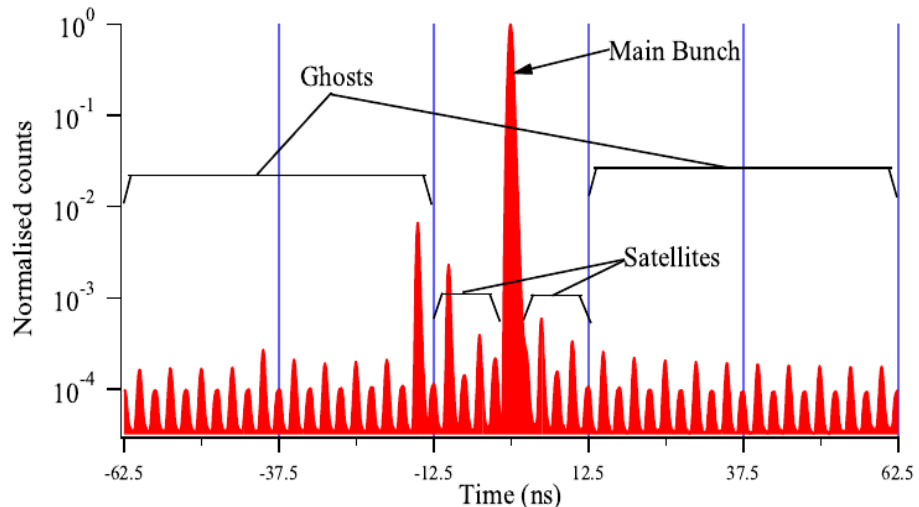


Figure 3.3: Longitudinal Profile taken with Longitudinal Density Monitor (LDM) detector showing definition of Ghost/Satellite bunches with respect to main bunches.

The presence of ghost/satellite bunches increases the uncertainty in LHC luminosity measurements and can also generate proton-proton interactions near but not at the collision region. Effects on ghost/satellite bunches on instantaneous luminosity measurements have been studied using CMS, ATLAS and ALICE detectors. Their results showing clear observation of physics events produced from ghost and satellite bunch collisions is shown in figure 3.4. CMS uses energy deposits in the endcap calorimeters to observe time space which is consistent with the expectation from ghost/satellite bunches while in ATLAS uses the Longitudinal Density Monitor (LDM) detector to

study ghost/satellite bunches.

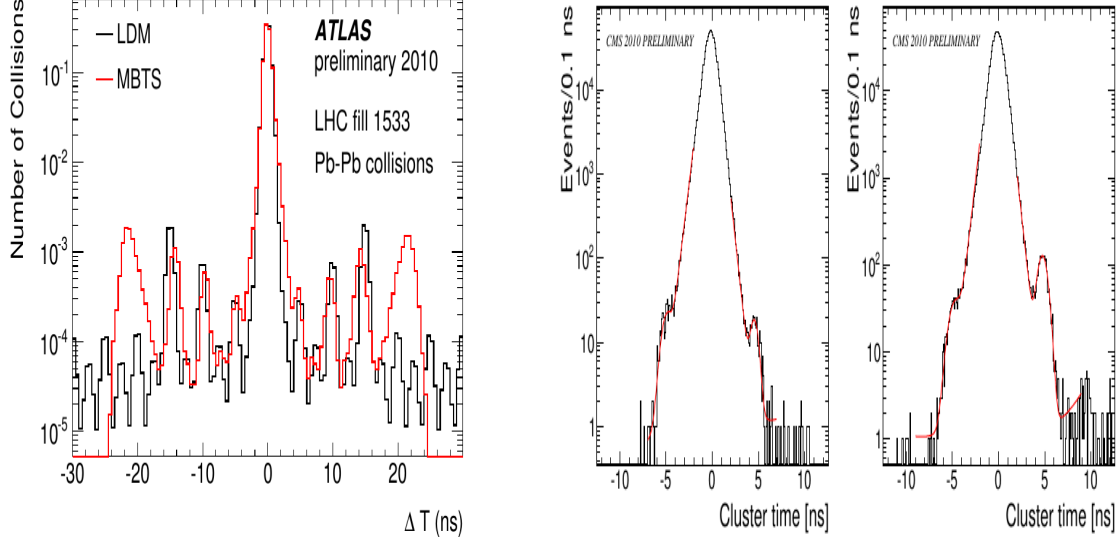


Figure 3.4: (left) Arrival time distribution(red) of ATLAS MBTS for LHC fill 1533 during 2010 Pb-Pb run and LDM profile(black) for Beam2(same for Beam1).

(Right) Timing of Clusters in the CMS endcap calorimeters for fill 1089:Left: EEP detector(left side of IP  $z > 0$ ) Right: EEM detector( right side of IP,  $z < 0$ ). Plots from ATLAS Ref.[28] and CMS, Ref.[29]

Table 3.1 gives a summary of the LHC design conditions compared to the conditions used during the LHC RUN 1 operation.

| LHC Operation Parameters 2010-2013  |                      |                       |                      |                       |
|-------------------------------------|----------------------|-----------------------|----------------------|-----------------------|
| Parameter                           | 2010 value           | 2011 Value            | 2012/13 Value        | Design Value          |
| Beam energy[TeV]                    | 3.5                  | 3.5                   | 4.0                  | 7                     |
| $\beta^*$ in IP 5[m]                | 3.5                  | 1.0                   | 0.6                  | 0.55                  |
| Bunch spacing [ns]                  | 150                  | 75/50                 | 50                   | 25                    |
| Number of bunches                   | 368                  | 1380                  | 1380                 | 2808                  |
| Protons/bunch                       | $1.2 \times 10^{11}$ | $1.45 \times 10^{11}$ | $1.7 \times 10^{11}$ | $1.15 \times 10^{11}$ |
| Normalised emittance[mm.rad]        | $\approx 2.0$        | $\approx 2.4$         | $\approx 2.5$        | 3.75                  |
| Peak luminosity[ $cm^{-2}s^{-1}$ ]  | $2.1 \times 10^{32}$ | $3.7 \times 10^{33}$  | $3.7 \times 10^{33}$ | $1 \times 10^{34}$    |
| Evts/bunch crossing                 | 4                    | 17                    | 37                   | 19                    |
| Stored Beam energy(MJ)              | $\approx 28$         | $\approx 110$         | $\approx 140$        | $\approx 362$         |
| Int. Luminosity by CMS[ $pb^{-1}$ ] |                      |                       |                      | -                     |
| Circumference[km]                   | 26.659               | 26.659                | 26.659               | 26.659                |
| Dipole Magnet B[T]                  | 8.33                 | 8.33                  | 8.33                 | 8.33                  |

Table 3.1: LHC operation parameter conditions during RUN 1, 2010-2013

## 3.2 Compact Muon Solenoid

### 3.2.1 Overview

The Compact Muon Detector (CMS) is a modern particle detector design for many different particle detection capability. It is one of the general purpose detectors located at one of the proton-proton collision points along the 27 km LHC ring. Its main feature is the presence of a superconducting solenoid of 6 m internal diameter providing a field of 3.8 T for measuring a charge particle's momentum as the particle bends under the influence of this field traveling in the detector. This magnetic field encloses an entirely silicon pixel and strip tracker detector used for vertex finding and for detecting and reconstructing the tracks of charged particles, a lead-tungstate scintillating-crystals electromagnetic calorimeter (ECAL) and a brass-scintillating sampling hadron calorimeter (HCAL). Very long lived particles like muons are measured in gas-ionization detectors embedded in the flux-return iron-yoke located at the outermost section of the detector. It has a simple cylindrical structure consisting of barrel and endcap detectors and an extensive forward calorimetry and detectors to provide a near  $4\pi$  solid angle coverage assuring good hermetic particle detection. The CMS apparatus has an overall length of 21.6 m, a diameter of 14.6 m, and weighs 12,500 tons. Figure 3.5 shows the CMS detector indicating the different sub-detectors and their material design type. We provide a performance summary and material type of each sub-detector in Table 3.2 of the CMS detector. The CMS uses a coordinate system with the origin coinciding with the center of the detector where proton-proton or nominal collision occurs. This point is commonly referred to as the *interaction point* (IP). The direction of  $x$ ,  $y$ , and  $z$ -axes are as shown in figure 3.6. However, for particle identification, CMS uses a more convenient coordinate system based on the polar coordinates. In this polar coordinate system, the azimuthal angle,  $\phi$ , is measured in the  $x - y$  plane, where  $\phi = 0$ , is the  $x$ -axis and  $\phi = \pi/2$ , the  $y$ -axis. The radial distance in this plane is denoted  $R$  and the polar angle  $\theta$  measured from the  $z$ -axis is related to *pseudo-rapidity*,  $\eta$ , through the relation;  $\eta = -\ln \tan(\frac{\theta}{2})$ . The coordinate system  $(\eta, \phi)$  and its radial distance  $R$  identifies a point in the cylindrical volume of the CMS detector. In the coming sections, we describe the geometry, material characteristics and functionality of the CMS subdetectors used in our analysis.

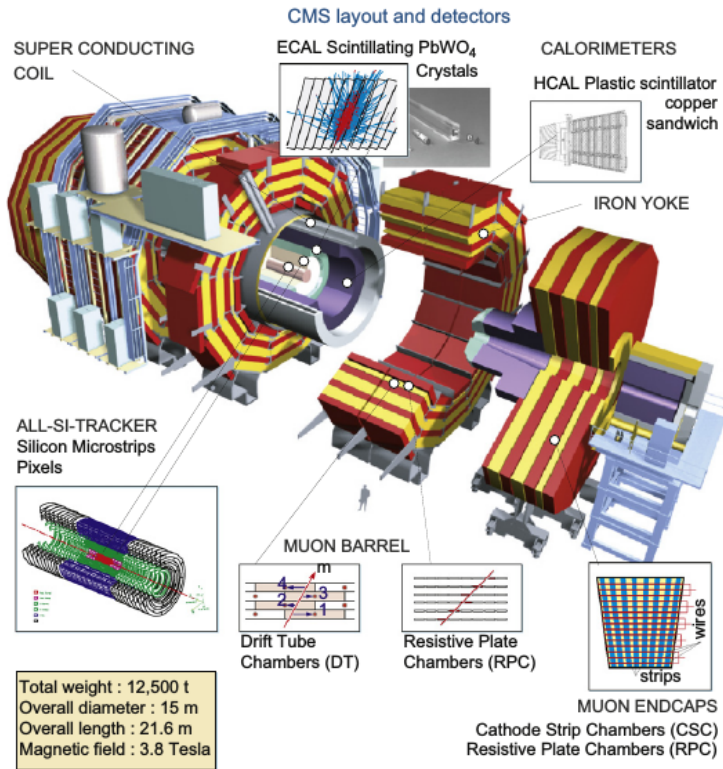


Figure 3.5: CMS Detector showing the different subdetectors and their material.

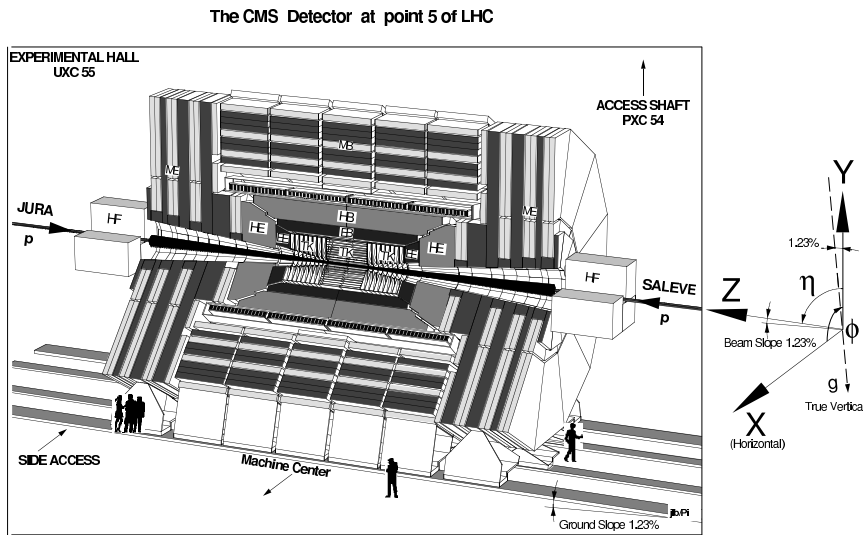


Figure 3.6: CMS detector schematic view with definition of  $x - y - z$  coordinates.

### CMS Detector and Resolution

| Subdetector    | Quantity            | Resolution   | Uses                                 |
|----------------|---------------------|--|--------------------------------------|
| Tracker        | Momentum[GeV/c]     | $\sigma_T/p_T \approx 1.5 \times 10^{-4} p_T + 0.005$                                    | Silicon Pixels and Strips            |
| ECAL           | Energy[GeV]         | $\sigma/E \approx 3\%/E + 0.003$   | PbWO <sub>4</sub> Crystals           |
| ECAL           | Time[ns]            | $\sigma(\Delta t) = \frac{N}{A_{eff}/\sigma_n} \oplus \sqrt{2}\bar{C}$                   | PbWO <sub>4</sub> Crystals           |
| HCAL           | Energy[GeV]         | $\sigma/E \approx 100\%/E + 0.05$  | Brass + Scintillator                 |
| Muon Chambers  | Momentum[GeV/c]     | $\sigma_T/p_T \approx 1\% \text{ at } 50 \text{ GeV to } 10\% \text{ at } 1 \text{ TeV}$ | inner tracker + Muon Systems         |
| Magnetic field | B-field strength[T] | 3.8 T + 2 T  | Solenoid + Return Yoke               |
| Triggers       | On/Off-line         | Levels   | L1(On-line)<br>+HLT(Off-line)(L2+L3) |

Table 3.2: CMS detector material, Ref.[20], and resolution(Time resolution:  $N \approx 35$  ns,  $\bar{C} \approx 0.070$  ns Ref. [37])

#### 3.2.2 Calorimeter

A CMS calorimeter absorbs a good fraction of energy of an incident particle and produces a signal with an amplitude proportional to the energy absorbed. This absorption is through the cascade production of secondary particles with energy of the incident particle directly proportional to the number of secondary particles produced. There are two types of calorimeters choices used in the CMS detector; the *Electromagnetic calorimeter* (ECAL); for absorbing the energy of electromagnetic particles such as photons and electrons and a *Hadronic calorimeter* (HCAL) made of more than one type of material for stopping and absorbing the energy of hadrons such as kaons and pions through strong interactions. The combined calorimeter detectors of CMS covers a region in  $|\eta| < 5$  making it nearly hermetic for good missing energy measurements. The ECAL

and HCAL are arranged in a nested fashion shown in figure 3.7 so that electromagnetic particles can be distinguished from hadronic particles by comparing the depth of the particle shower penetration in both calorimeters.

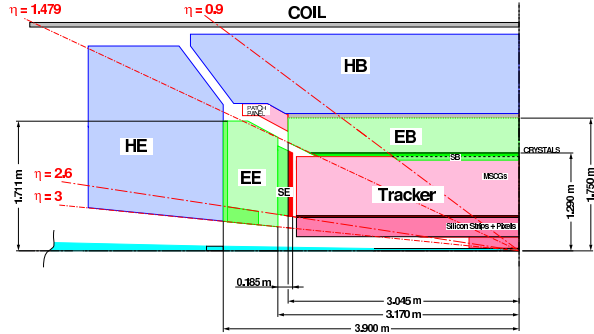


Figure 3.7: Schematic diagram of CMS calorimetry system with HCAL enclosing ECAL in the Barrel and Endcap regions.

### Electromagnetic Calorimeter

The electromagnetic calorimeter (ECAL) detects photons and electrons. High energy photons and electrons are detected through their interaction with the lead tungstate ( $\text{PbWO}_4$ ) crystals. During this interaction which happens either through electromagnetic showering or electron-positron pair production (*bremsstrahlung*), the incoming photon or electron deposit practically almost all of its energy. There are 75848 crystals in total mounted in a cylindrical geometry, with a barrel (EB) and an endcap (EE) structure. The choice of  $\text{PbWO}_4$  crystals as calorimetry material by CMS for operation in the LHC environment is because of its a high density ( $8.28 \text{ g/cm}^3$ ), short radiation length ( $X_0=0.89 \text{ cm}$ ) and a small Molière radius (22 cm). In a high radiation dose and fast timing (25 ns proton bunch spacing) environment like the LHC,  $\text{PbWO}_4$  crystals is preferred to other crystal materials for its high radiation resistance and a scintillation decay time which is comparable to the LHC bunch crossing interval of 25 ns and about 80% of the light is emitted in 25 ns. The probability of an electromagnetic object with high energy to interact either through *Bremsstrahlung* or *pair production* with the material in ECAL is proportional to the nuclear charge,  $Z$ , of the material.  $\text{PbWO}_4$  is a high  $Z$  material and this makes it once more the preferred material choice for electromagnetic calorimetry by CMS. The small Molière radius ensures that on average about

95 % of the electromagnetic shower energy is contained within a crystal crystal volume of about 9 crystals. This reduces the transverse spread of the electromagnetic cascade from multiple scattering of electrons and helps improve on the estimation of the transverse position of impact of an incident particle. It also provides a fine granularity for measuring the particle's energy by providing fewer overlap of particle signals. Its dense nature also allows for the electromagnetic shower to develop early and therefore likely to be fully contained within a compact device like CMS.

The EB section of the ECAL covers a pseudo-rapidity of  $|\eta| < 1.479$ . It has 61,200 crystals providing a granularity of 360 degree fold in  $\phi$  and  $(2 \times 85)$ -fold in  $\eta$ . The crystals are mounted in a quasi-projective geometry so that their axes make an angle of 3% with respect to a line vector from the nominal interaction vertex in  $\eta$  and  $\phi$  directions. This avoids cracks aligned with a particle's trajectory. A crystal in EB is approximately  $0.0174 \times 0.0174$  in  $\eta - \phi$  or  $22 \times 22 \text{ mm}^2$  at its front face and  $26 \times 26 \text{ mm}^2$  at its rear face. Each crystal is 230 mm long corresponding to about  $25.8 X_0$  radiation lengths. The crystal's radial distance measuring from the center of the face of the crystal to the beam line is 1.29 m. A number of crystals are placed in a thin-walled alveolar structure made with aluminum forming a *submodule*. Each submodule is arranged into 4 modules of different types according to their  $\eta$  position. There are about 400 to 500 crystals in each module and these 4 combined make one *supermodule* containing 1700 crystals. To reduce crystal reflective lost, the aluminum surface is coated to avoid oxidation leading to coloration. On the rear end of each EB crystal, two *Avalanche Photodiodes* (APD) is glued to collect the scintillating light from the crystals converting light into charge current which is further collected by the read-out electronics.

The endcap sector covers a pseudo-rapidity region of  $1.479 < |\eta| < 3.0$  with a Preshower (ES) detector made of silicon strip sensors interleaved with lead placed immediately in front of it. The purpose of the preshower is to identify photons from the decay of neutral pion,  $\pi^0 \rightarrow \gamma\gamma$  and also to help separate photons producing electrons through pair production from photons not producing electrons before their arrival at the EE. The endcap located on the  $+z$  side of the nominal interaction is denoted EE+ while the other located on the  $-z$  side is denoted as EE-. The longitudinal distance between the IP and the center of the surface of the EE crystals is 3.154 cm. Each endcap is divided into two halves called *Dees* with each Dee holding 3662 crystals. Crystals in EE with identical shape

are grouped into  $5 \times 5$  units called *supercrystals* (SC). The crystals in the SC form an  $x - y$  grid. Each crystal is 220 mm ( $24.7 X_o$ ) in length and has a front face and rear cross section of  $28.62 \times 28.62$  square mm and  $30 \times 30$  square mm, respectively. Vacuum Phototriodes (VPT) instead of APDs is glued on the rear face of each crystal for scintillating light conversion into electrical signals. The VPT is used in the EE because of its high resistance to radiation and smooth operation in a strong magnetic field environment. These APDs and VPTs are used because of their high gain relative to regular photodiodes with no gain and the fact that they are not affected by the high magnetic field. Although the light yield for  $\text{PbWO}_4$  crystals is rather low ( $\approx 70$  photons/ MeV), these photo-detectors have internal gain (50 for APDs and 10 for VPTs) and quantum efficiency of 75 % for APDs and 20 % for VPTs of the emission wavelength. This makes it possible that signals from incident particles with energies of a few to high GeV longer than noise.

The signals from the APDs and VPTs are digitized by voltage-sensitive analogue-to-digital converters and through fibre-optic links transported as light signals to the counting room located adjacent to the experimental cavern.

The energy resolution and geometry structure of the ECAL ensures that the photon or electron's arrival energy, time, position and even the direction through the shape of its electromagnetic shower in the crystals can be identified and measured with good precision.

### **Hadronic Calorimeter**

The CMS Hadron Calorimeter (HCAL) is comprised of four distinct subdetectors: the Barrel (HB), the Endcap (HE), the Outer Barrel (HO), and the Forward (HF). Unlike the ECAL, the HB, HE and HO subdetectors are scintillator-sampling calorimeters with embedded wavelength shifting fibers (WLS). HB, HE and HO uses brass plates as the inactive material and plastic scintillator with WLS as the active material. The brass plate is used for absorbing the hadronic shower which comprise of an *electromagnetic*(particles like  $\pi^0$ s,  $\eta$ s and other mesons generated in the absorption process and decay to  $\gamma$ s which develop electromagnetic (em) showers) and *non-electromagnetic* components. The plastic scintilator is divided into 16  $\eta$  sectors resulting in segmentation of  $\Delta\eta \times \Delta\phi = 0.087 \times 0.087$ . It was chosen for its long-term stability and moderate

radiation hardness. energy. The scintillating light through the WLS brings the light to hybrid photodiodes (HPDs) in the HB and HE. HPDs which have high electrical noise and will be replaced with silicon photon multipliers (SiPM) which have low noise during the current CMS detector upgrade. The HB and HE combine cover a region in pseudo-rapidity of  $|\eta| < 3$ . The HB covering the region  $|\eta| < 1.3$ , is divided into two-half barrel (HB+ and HB-) sections each composed of 18 identical  $20^\circ$  wedges in  $\phi$ . Each wedge is made of flat brass alloy and steel(only front and back plates) absorber plate. HE covers  $1.3 < \eta < 3.1$  and has plastic scintillation tiles with granularity of  $\Delta\eta \times \Delta\phi = 0.087 \times 0.087$  for  $|\eta| < 1.6$  and  $\Delta\eta \times \Delta\phi = 0.17 \times 0.17$  for  $|\eta| > 1.6$ . The HO is an extension of HB outside the solenoid and thus utilizes the solenoid coil as an additional absorber. It is used to identify the starting shower and to measure the shower energy deposited after HB. The first active layer of the scintillating tiles is situated directly behind the ECAL in order to actively sample low energy showering particles from the support material between the ECAL and HCAL.

The HF occupies a pseudo-rapidity region of  $3 < |\eta| < 5$ . Its purpose is to provide a closer to  $4\pi$  hermetic phase space coverage required for missing transverse energy calculation or MET. MET is the established signal for very weakly interacting particles like neutrino and supersymmetric particles like gravitino which travel through the detector undetected. HF consists of radiation hard quartz fibers embedded in steel absorbers running parallel to the beam axis. The signal from Cherenkov light emitted in the quartz fibers in response to charged particles makes it possible to detect all charge particles in the forward region. The HF calorimeter has long and short fibers for better sampling and to distinguish showers generated by electrons and photons from those generated by hadrons. The choice of quartz fibers is because of its high resistance to the high radiation in the forward detectors and its fast production of light through Cherenkov process.

For  $|\eta| < 1.48$ , the HCAL cells map on to  $5 \times 5$  ECAL crystal arrays to form calorimeter towers projecting outwards from near the nominal interaction point. In each tower, the energy in ECAL and HCAL cells is summed to define the calorimeter energy tower. The energy ratio of an HCAL tower to an ECAL in a calorimeter energy tower can be used to improve photons and electron identification.

### 3.2.3 Muon Chambers

Muons unlike electrons and hadrons do not deposit most of their energy in the calorimeters. They are capable of traveling across the entire CMS detector into the muon chambers. Muons produce tracks which run across the CMS detector starting from the silicon pixel and strip subdetector closest to the IP called the *Tracker* and depositing very little fraction of their energy in the calorimeters unto the muon chambers. The muon chambers use the process of ionization and a 2 T magnetic field from the return iron yokes (bending the tracks of charge particles) to measure the momentum of charged particles. The three different types of muon chambers used by the CMS are: the drift tubes (DT) chambers in the barrel, cathode strip chambers (CSC) in the endcaps and resistive plate chambers (RPC) glued to the DT and CSC chambers. Four layers or stations of DT/RPC and CSC/RPC are embedded in an interleaved style with the iron yoke for track reconstruction and triggering. Figure 3.9 is a longitudinal view of the CMS detector showing the position of the muon stations. The DT and CSC record track segments characterized by the position of the track and the bending angle. This information is used to determine the precise transverse momentum and charge of particles during particle reconstruction. The RPCs(DTs and CSC will also be used after the current detector upgrade) are dedicated L1 trigger chambers used to determine the candidate muon's approximate transverse momentum and proton bunch crossing number. The RPC has a timing resolution of about 3 ns.

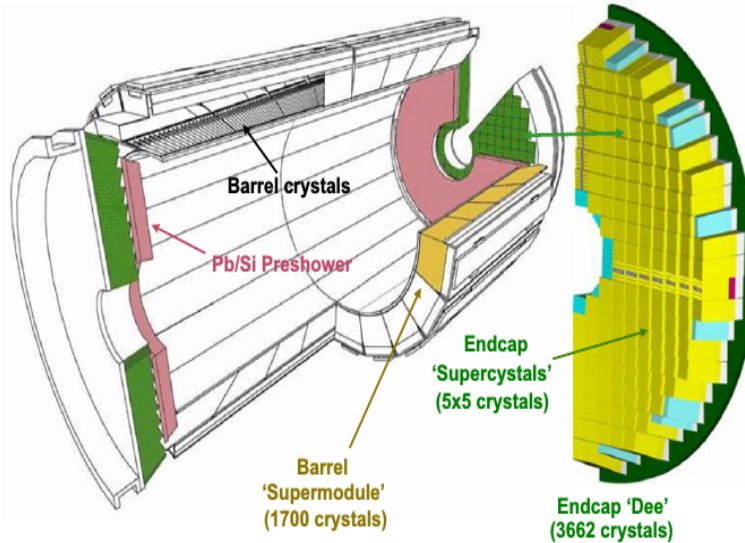


Figure 3.8: Layout of the CMS electromagnetic calorimeter showing the arrangement of crystal modules, supermodules in the barrel with the preshower in front of endcap with supercrystals.

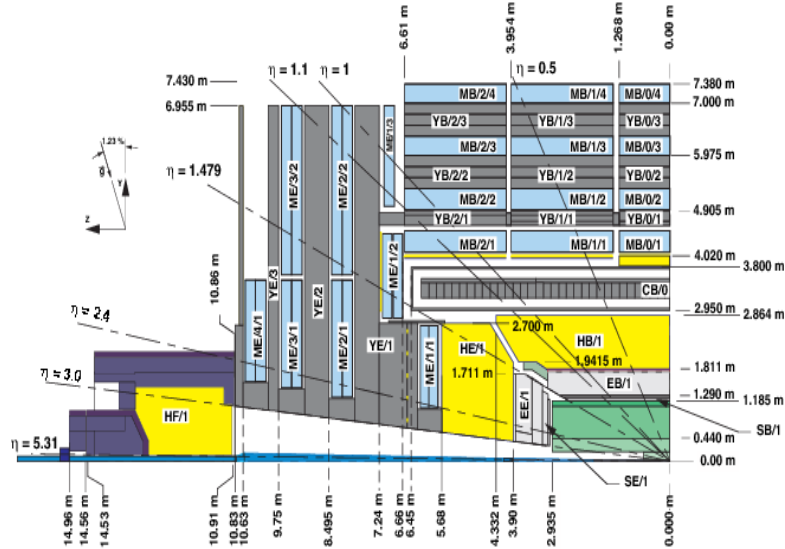


Figure 3.9: Cross section view showing the coverage range of CMS sub-detectors and their longitudinal distance from the IP.

### 3.2.4 Triggering

In CMS, there are a billion interactions including *pile up* (PU) happening each second. This means data from each 25 ns proton-proton collision has to be processed and stored before the next collision happens. Also, since not all these collisions produce interesting physics events, we have to be capable of selecting only interesting physics events produced from proton-proton collisions with sufficient energy. The process of selecting such interesting events is called *triggering*. CMS uses a two level triggering system for selecting interesting events produced with enough energy from collisions. The comprise of the *Level-1* (L1) and *High Level Triggers* (HLT) triggers.

The L1 triggers is a hardware designed electronics system implemented in FPGA and ASIC technology and uses information from the calorimeter, muon trigger and a global trigger board. The global trigger board makes the final decision based on the calorimeter and muon triggers to reject or keep an event for further processing at the HLT trigger. The L1 trigger is responsible for selecting the best 100,000 events/second from the initial 1 billions events/second produced.

The HLT is a software comprised of implemented selection algorithms running on a farm of more than 1000 standard computers. These complex algorithms include instructions like, match tracks to hits from the muon chambers, select energy deposits above a certain threshold in the calorimeters with no tracks for electromagnetic objects, and begins the first step of event selection. Just like the L1 trigger, the HLT uses assimilated and synchronized information from different parts of the CMS detector to create the entire event. By the time this selection process is complete, there are now only 100 events/second with the remaining 99,900 thrown away. Taking an average event size to be 1 Megabyte, in a stable and effective LHC proton collision period of a year or  $10^7$  seconds, CMS produces about a Petabyte of data which is stored and used later for offline physics analysis.

## Chapter 4

# Timing Reconstruction and Calibration

### ECAL Timing Overview

An electromagnetic particle's arrival time at ECAL from proton-proton ( $pp$ ) collisions can be measured using it's energy and time recorded by ECAL subdetector crystals. The energy recorded by each crystal is called a *hit*. Using this hit, we can calibrate the time of each of the 75848 ECAL crystals to ensure that the arrival time of an electromagnetic particle of an event is accurately measured. Crystal time calibration means defining the same reference time used by each crystal for measuring the particle's arrival time. This can be achieved by using an electromagnetic particle like a photon, produced from a  $pp$  collision at IP, and whose trajectory or path traveled from IP to the surface of a crystal and traveling with the speed of light is a straight line. For such a particle, its time-of-flight (TOF) is the ratio of the distance traveled to the speed of light. The photon time measured by each ECAL crystal is assumed to be the same for every other crystal and defines the absolute or reference time for every other similar electromagnetic particles. The time needed to transfer the recorded signal from the front-end detectors to the back end readout electronics is also assumed to be the same for all crystals. Taking the TOF into account, we define the crystal time,  $\langle t \rangle \approx 0$  as the reference time for the time measurement of the photon by each crystal. Thus, if a crystal is properly calibrated, then the average time for hits belonging to the same

event must be zero, i.e.,  $\langle t \rangle_{\text{many hits}} \approx 0$ .

We use for the time of an electromagnetic object like a photon, either, the time of the crystal with the highest hit energy which we call the *seed crystal* or an error weighted average or mean time of the individual time measured by crystals belonging to the photon object(a single photon is also called a *super cluster* which is made from many crystals. A supercluster can also be made of many smaller clusters called *basic clusters*). The seed time is denoted  $t_{\text{seed}}$  and  $t_{\text{Ave}}$  is the average time. Equation 4.1 is an expression for the average time.

1. **seed time:** The time of the highest energy crystal or hit in the highest energy basic cluster (about 9 crystals) of the photon super cluster (about 25 crystals). It is denoted  $t_{\text{seed}}$ .
2. **Average or mean time:** This is the error weighted average time of all the crystals in the photon seed basic cluster. It is denoted as  $t_{\text{Ave}}$  or  $t_{\text{mean}}$ .

$$t_{\text{Ave}} = t_{\text{mean}} = \frac{\sum_{i=1}^N \frac{t_{\text{reco},i}}{\sigma_i^2}}{\sum_{i=1}^N \frac{1}{\sigma_i^2}} \quad (4.1)$$

where  $N$  is the number of crystals of the seed basic cluster of photon super cluster,  $t_{\text{reco},i}$  and  $\sigma_i$  is the reconstructed time and uncertainty or error of the time reconstructed for each crystal respectively.

Therefore, the arrival time of a photon or an electromagnetic object,  $t_\gamma$  or  $t_{e^\pm}$ , can either be given as  $t_{\text{seed}}$  or  $t_{\text{Ave}}$ . The definitions  $t_{\text{seed}}$  and  $t_{\text{Ave}}$  have similar performances and also advantages and disadvantages. We explore these in the analysis section of this thesis. Before we continue, let us describe in detail how a crystal time is actually recorded by the ECAL detector. We first describe the electronics read out sequence of the ECAL and continue with how we extract the timing from the electronic signals recorded.

## 4.1 Electromagnetic Calorimeter Readout Chain

The ECAL electronics readout system fully described in [31] is a light-to-light system. Energy from an incoming electromagnetic object is absorbed and converted into scintillating light by PbWO<sub>4</sub> crystals. The scintillating light from these crystals is received and converted into photocurrent by Avalanche Photo-Diodes (APD) in EB and Vacuum Photo-Triodes (VPT) in EE. The relatively low light yield of the crystals requires a pre-amplifier which converts the photocurrent into a voltage waveform. This pre-amplifier also has an internal pulse shaping and the acquired pulse shape is digitized over a full dynamic range by a floating-point analog-to-digital (ADC) conversion system. The digitized data of each signal is converted into an optical data stream which is transported off the detector through optical fibers to the upper-level off-detector where the formation of trigger tower energy sums, pipelining (temporal storing of data until receipt of first level trigger decision) and transmission of triggered data to the data acquisition system is performed. The ECAL full readout chain can be divided into an *on-detector* and *off-detector* electronics. Both electronic systems are connected by 100 m radiation hard optical fiber links for transporting the optical data stream.

The on-detector electronics reads a trigger tower consisting of  $5 \times 5$  crystals arranged in  $\eta \times \phi$  grid in barrel (EB) and  $x - y$  grid in endcap (EE). Five Very Front End (VFE) boards (reading out data from 5 crystals each), one Front End board (FE), two (EB) and six (EE) Giga Optical Hybrids (GOH), one Low Voltage Regulator (LVR) board and a Mother Board (MB) make up the complete on-detector electronics. Electrical Signals from the APDs are accepted by the VFE equipped with a Multi-Gain Pre-Amplifier (MGPA), a 12-bit Analogue to Digital Converter (ADC) and a buffer. The MGPA (an Application Specific Integrated Circuit (ASIC) developed in 0.25  $\mu\text{m}$  technology), pre-amplifies, shapes and then amplifies the signals through three amplifiers with gains of 1, 6 and 12. For the VPT (EE), these signals first pass through a High Voltage (HV) filter card which acts as a moderator separating very high voltages caused by the increase radiation in the EE. The full scale of the APDs and VPTs are 60 pC and 12.8 pC corresponding to  $\approx 1.5$  TeV and 1.6-3.1 TeV respectively. The full shaping of the signal takes about 40 ns. The noise for gain 12 is about  $8000e^-$  for APD configuration and about  $4000e^-$  for VPT configuration. The 3 analog output signals

of the MPGA are digitized in parallel by the multichannel 40 MHz, 12-bit ADC. This ADCs have an effective number of bits of 10.9. The highest non-saturated signal is selected as the output signal and reported as 12 bits of the corresponding ADC with 2 bits coding the ADC number. It is possible, that when the signal is saturated, a wrong signal amplitude can be produced leading to some amplitude dependence of the readout time. This effect has been studied for Gains 1 and 6 transitions and the relevant correction factors for adjusting timing measurements due to this effect validated and applied. The figures in 4.1 is a schematics picture showing the readout chain of the FE with its MPGA and ADCs. The shaping and digitization process of a sample pulse shape (see figure 4.2) is also shown. Since the trigger decision processing requires more than one bunch crossing (BX)(1 BX=25 ns), the signal data is pipelined during the trigger latency of  $3\ \mu s$ .

To protect the electronics from extreme radiating, a radiation-hard buffer adapts a low voltage differential output signal (LVDS) of the ADC to input into the FE. Signals from five identical channels are integrated and read into VFE card with a Detector Control Unit for measuring APD leakage currents. The noise from each VFE is typically 1.1, 0.75, 0.6 ADC counts for gains 12, 6 and 1 respectively. This would be about 40 MeV for gain 12. Digitized data from 5 VFE cards are fed into each FE through the LVDS and stored in 256-word-deep dual-ported memories called pipelines. Data pipelines can be stored for up to 128 bunch crossings. The FE is base on a ASIC called FERNIX holding and the logic is to calculate the energy of 5 channels once every bunch crossing. This energy is summed in strips of 5 crystals along  $\phi$ . This means each VFE is serviced by a FERNIX chip. In the case of the EE, the five strip energy sum are transported by GOH to the off-detector electronics Trigger Concentration Card (TCC) while for EB, there is a sixth FERNIX which sums the five strips energy sums and calculates an electromagnetic bit which is used to identify electromagnetic shower candidates on the basis of their shower profile in a trigger tower. The trigger tower ( $5 \times 5$  crystals) energy sums and the electromagnetic bit is transmitted to the TCC through the GOH. This process is referred to as Trigger Primitive Generation (TPG). Once a Level-1 trigger signal is received, the ten 40 MHz samples for each channel are transmitted to the off-detector electronics Data Concentration Card (DCC) using an identical GOH. This takes about  $7.5\ \mu s$ . The VFE and FE cards are controlled using a 40 MHz digital optical

link system controlled by the off-detector Clock and Control System (CCS).

The Off-detector electronics consist of different types of electronic boards (the Clock and Control System (CCS), Trigger Concentration Card (TCC) and Data Concentration Card (DCC) modules) sitting in an 18 VME-9U crates and a 1 VME-6U crate holding the Selective Read-Out Processor (SRP). This system is serving both the trigger and the Data Acquisition Systems (DAQ) paths. In the DAQ path, the DCC performs data read-out and data reduction based on flags of the SRP. While in the trigger path, at each bunch crossing, the trigger primitive generation which began in the FE is finalized and synchronized or time aligned in the TCC before being transmitted to the regional calorimeter triggers. The trigger primitives each referring to a single trigger tower (25 crystal data) consists of the summed transverse energy deposits and the electromagnetic bit characterizing the lateral shower profile of the electromagnetic shower. The accepted signal for accepted events is returned from the global trigger after about  $3 \mu\text{s}$  and the selected events are read into the data acquisition system to the filter farm where the even rate is further reduced using data from the full detector.

In the regional calorimeter, the ECAL trigger primitives together with the HCAL trigger primitives are used to compute the electron/photon and jet candidates as well as their transverse energy. The resulting physics objects after passing through the HLT trigger are transferred to the various tier systems for offline full event reconstruction. The ECAL also has a laser calibration systems where laser light is delivered directly to the PbWO<sub>4</sub> crystals using optical fibers. The laser data is used for energy and time calibration of crystals and hardware system. The crystals are energy calibrated because of the decrease in optical transmission due to the formation of color centers in the crystal. The formation of color centers is caused by irradiation. Time calibration using laser data can be performed in case there are hardware timing offset especially during long short down maintenance period of the CMS detectors.

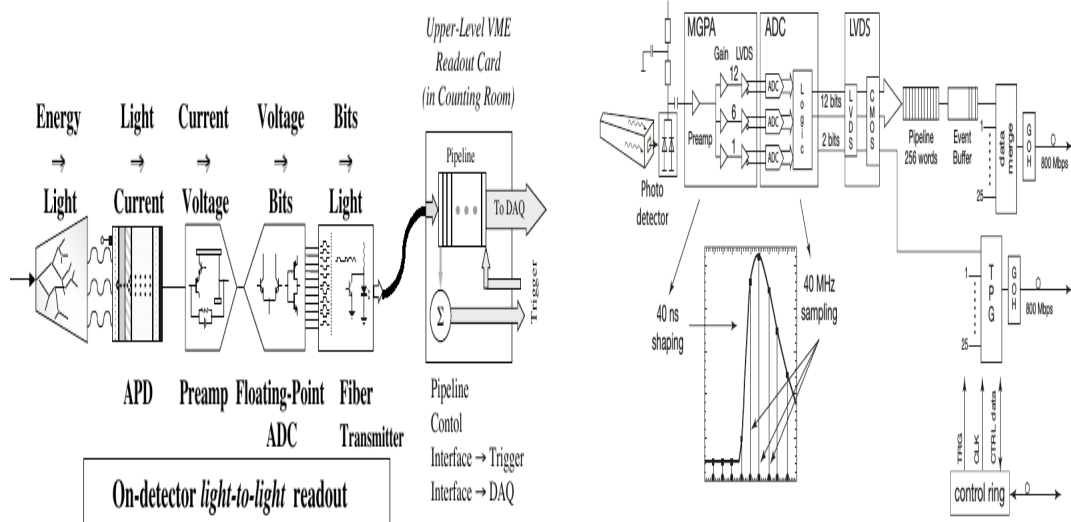


Figure 4.1: Schematic diagram of the CMS ECAL ReadOut Chain.

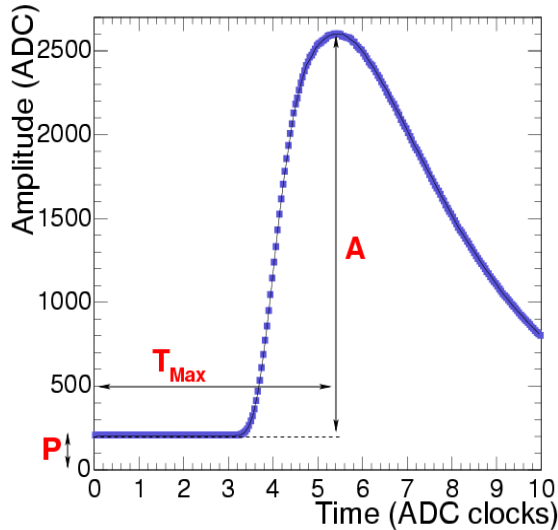


Figure 4.2: Typical pulse shape of a given signal showing crystal signal.

## 4.2 Timing Extraction

Using the pulse shape from a single crystal produced by an arriving photon or electron, the photon's energy deposited on each crystal is obtained from the amplitude of the

pulse shape while it's arrival time is extracted using 10 samples created by sampling the pulse shape with an ADC clock of sampling frequency, 40 MHz. The distribution of these 10 samples along the pulse shape is shown in the left plot in figure 4.3. The value  $\mathbf{P}$  in figure 4.2 is the pedestal or noise read in ADC counts in the absence of a signal. A timing algorithm is employed to extract the time. The objective of this algorithm is to use the maximum amplitude value of the pulse,  $\mathbf{A}_{\text{MAX}}$ , and its corresponding time value of the ADC time,  $\mathbf{T}_{\text{MAX}}$  to reconstruct an event time. Finding the true  $\mathbf{A}_{\text{MAX}}$  is archived using an energy reconstruction algorithm. Extracting of the arrival time is by comparing the pulse shape of a channel obtained during proton-proton collision to a reference pulse shape obtained during early LHC *test beam* results. This reference pulse shape has been obtained from measurements using synchronous LHC events. Figure 4.3(*Left*) shows a distribution of  $A/A_{\text{MAX}}$  on the vertical axis against  $T - T_{\text{MAX}}$  on the horizontal axis obtained from test beam experiments.  $T$  is an arbitrary time measurement and  $\mathbf{T}_{\text{MAX}}$  is the time when the pulse reaches its maximum value,  $\mathbf{A}_{\text{MAX}}$ .

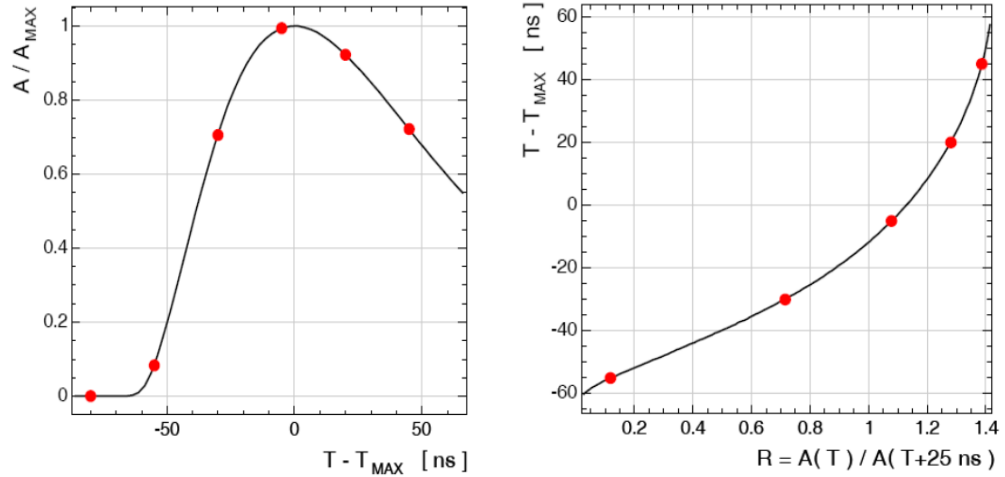


Figure 4.3: *Left*: A measured ECAL pulse shape for a single channel. *Right*:  $T - T_{\text{MAX}}$  Vs  $R(T)$  showing the distribution of  $T(R)$ . Solid line is reference shape or shape from test beam while dots correspond to a 10 discrete samples corresponding to signal from proton-proton collision.

The test beam comparison is realized through an analytic fit to the 10 digitized samples. However, performing this fit directly on the  $A(T)$  distribution to obtain  $\mathbf{A}_{\text{MAX}}$  and  $\mathbf{T}_{\text{MAX}}$  is cumbersome and technically inefficient since the amplitude of each sample

depends on the pulse shape, the  $\mathbf{A}_{MAX}$  value and also the relative position of  $\mathbf{T}_{MAX}$  between each sample point. This relative position or phase is referred to as “ $T_{MAX}$  phase”. In order to minimize the fit dependence on  $A_{MAX}$  and the  $T_{MAX}$  phase, a new variable not sensitive to this phase, defined as,  $R(T) = A(T)/A(T + 25 \text{ ns})$ , is used and the analytic fit is performed on the distribution of  $T - T_{MAX}$  against  $R(T)$ . This  $T(R)$  distribution is independent of  $A_{MAX}$  and can be very well described using a polynomial of order 7. A distribution of  $T(R)$  is shown in figure 4.3(*Right*) with both the four to five samples points (dots) obtained from the ratio  $R_i = A_i/A_{i+1}$  from each consecutive pair of samples and the reference pulse shape (continuous line). Each point  $R_i$  gives a quick accurate measurement of  $T_{MAX,i} = T_i - T(R_i)$ . The uncertainty,  $\sigma_i$ , on each measurement is a product of the derivative of the function  $T(R)$  and the uncertainty on the value of  $R_i$ . The uncertainty on the value of  $R_i$  depends on three separate uncertainties: the noise fluctuation,  $\sigma_n$  of each sample, the uncertainty in the estimation of the pedestal value which is always subtracted from the measured value and the truncation during 12-bit digitization. These uncertainties are uncorrelated and can be added in quadrature. The reconstructed time and its error of a hit (fraction of energy deposited on a single crystal) is determine according to equation 4.2 by taking into consideration the different uncertainties,  $\sigma_i$  of each point,  $R_i$ .

$$T_{MAX} = \frac{\sum \frac{T_{MAX,i}}{\sigma_i^2}}{\sum \frac{1}{\sigma_i^2}} \quad ; \quad \frac{1}{\sigma_T^2} = \sum \frac{1}{\sigma_i^2} \quad (4.2)$$

The sum is over all the 4 or 5  $R_i$  ratios and the assumption is that the weights are uncorrelated.

### 4.3 Timing Resolution

Using the reconstructed time for each channel,  $\mathbf{T}_{MAX}$ , we can measure how reliable is using the ECAL detector to measure the arrival time of a photon or electron. This reliability can be quantified using the *timing resolution*,  $\sigma(t)$ . The timing resolution for ECAL can be parametrized and expressed as a sum in quadrature (uncorrelated) of three major terms contributing to the uncertainty in time measurement. These three contributions are: First, the *Noise* ( $N$ ) term, from electronic noise, coherent movement

of the baseline and effects arising in addition to the main or hard proton-proton collision, other soft or less energetic collision producing events called *pile up* (PU) events. Second, the *Stochastic* term ( $S$ ), from fluctuations in the photon collection time because of the finite time during PbWO<sub>4</sub> scintillation. Finally the *Constant* term ( $C$ ) whose contribution is independent of the energy deposited but rather from effects correlated with the point of shower initiation within the crystal and systematics in the extraction of the time due to different pulse shape for each channel. The timing resolution,  $\sigma(t)$ , with all these parameters can be expressed as given in equation 4.3.

$$\sigma^2(t) = \left( \frac{N}{A/\sigma_n} \right)^2 + \left( \frac{S}{\sqrt{A}} \right)^2 + C^2 \quad (4.3)$$

$A$  is the measured amplitude corresponding to the energy deposited and  $\sigma_n$  is the intrinsic noise for individual channel.  $\sigma_n$  has a value of  $\approx 42$  MeV and 140 MeV in the barrel and endcap respectively.  $N = 33$  ns has been measured from Monte Carlo (MC) simulation studies. Contribution from the stochastic term, ( $S$ ) is considered small, with value of  $S < 7.9$  ns·MeV<sup>1/2</sup>.

To measure the timing resolution, a simple experiment was performed in which electron beams with energies between 15 GeV (GeV = Giga electron volts =  $10^6$  eV, 1 eV =  $1.602 \times 10^{-19}$  joules (J) in energy units) and 250 GeV was directed unto each crystal in a supermodule. The timing resolution measurement is obtained by extracting from the measured distribution of the difference in timing between two crystals sharing energy and from the same electromagnetic shower. The advantage of this approach is that, the contribution from poor synchronization is less as synchronization effects do not affect the spread. The average time method was not used as it is affected by synchronization effects. There are other studies where the time difference between two groups of crystals, about,  $5 \times 5$  crystals called basic clusters of an electromagnetic shower was used.

Neglecting the stochastic term since its contribution is negligible, the timing resolution from two objects (crystals or basicclusters) can be expressed as given in equation 4.4. It is this approach which we employ in future studies of the ECAL timing resolution.

$$\sigma^2(t_1 - t_2) = \left( \frac{N}{A_{eff}/\sigma_n} \right)^2 + 2\bar{C}^2 \quad (4.4)$$

In equation 4.4,  $A_{eff} = A_1 A_2 / \sqrt{A_1^2 + A_2^2}$ ,  $t_{1,2}$  and  $A_{1,2}$  correspond to the times

and amplitudes of the two objects and  $\bar{C}$  is their residual contribution. We measure the timing resolution by using the standard deviation of a Gaussian fit to the time distribution from each slice in  $A_{eff}/\sigma_n$  distribution. The resulting distribution of  $\sigma(t_1 - t_2)$  of the extracted standard deviation of each slice against  $A_{eff}/\sigma_n$  is fitted to extract the noise and constant term. The result is shown in Figure 4.4. The noise factor  $N = (35.1 \pm 0.2)$  ns and  $\bar{C} = (20 \pm 4)$  ns from the fit gives the values measured from the test beam experiment.

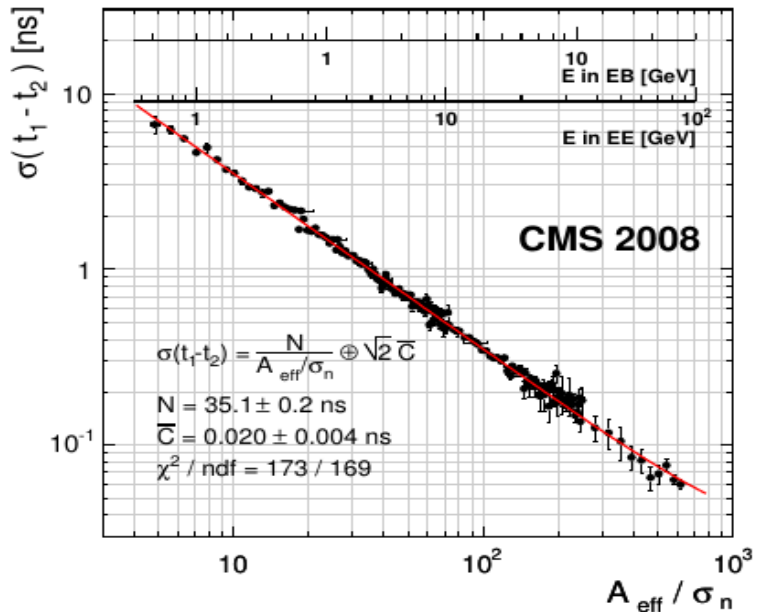


Figure 4.4: Deviation of the timing difference as a function of  $A_{eff}/\sigma_n$  between two crystals sharing an energy in the same electromagnetic shower obtained during electron testbeam measurements. The single crystal energy scales for barrel (EB) and endcap (EE) is overlaid. The fitted results give  $N = (35.1 \pm 0.2)$  ns and  $\bar{C} = (20 \pm 4)$  ns.

A timing resolution better than 100 ps for energy values  $A_{eff}/\sigma_n$  greater than 400 ADC counts is obtained. This demonstrates that for a perfectly calibrated ECAL crystals and energy deposits of  $E > 20$  GeV in the barrel, we can obtain a resolution better than 100 ps.

### 4.3.1 Timing Calibration Procedure

Timing calibration is performed such that photons traveling along a straight path with speed close to the speed of light,  $\beta \approx 1$ , produced from proton-proton collisions at IP will arrive at the surface of ECAL crystals with an average time of 0 ns. This means, photons or electrons arriving at an ECAL crystal with significantly and positively large arrival time, have either been produced from massive particles traveling with very small velocity (slow moving particles,  $\beta \ll 1$ ) or were produced from a decay point and traveled a path which significantly deviates from the obvious straight path connecting the IP to the crystal. Large arrival time photons or electrons could also be produced in the decay of temporarily stopped particles inside the CMS detector. To reduce contributions from photons with mis-reconstructed or mis-measurement time, we time calibrate all the 75848 ECAL PbWO<sub>4</sub> crystals. Timing calibration also ensures the synchronization of all the component objects of a given event and assigns that event to the correct LHC proton-proton collision or bunch crossing. The presence of the “ $T_{MAX}$  Phase”, the difference in pulse shape between each crystal, variation in time of flight by a few nanosecond (ns) and the different intrinsic delays among channels allow for timing calibration at two separate levels. At the level of the front end electronics (FE) consisting of  $5 \times 5$  crystals, one is capable of performing an initial internal timing synchronization by adjusting in steps of 1.04 ns among these crystals. Determining the values of adjustments to be made is referred to as *Hardware Synchronization*. Offline, during event reconstruction, we can find and assign timing constants such that the measured crystal time for photon objects is on average zero for true collision events arriving in a straight path from IP.

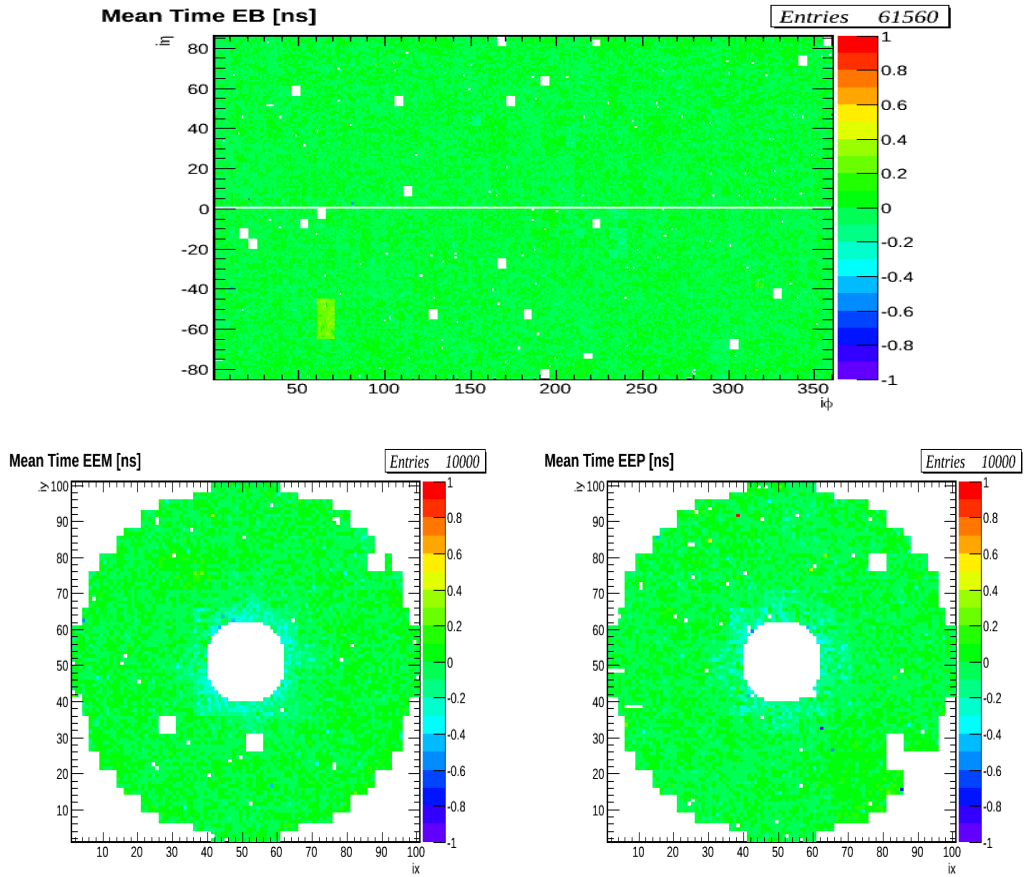
### 4.3.2 Offline Timing Calibration

The purpose of the offline calibration is to provide timing adjustments constants for each channel (crystal). These constants are derived from proton-proton collision data to adjust for global phase shift in timing measurements caused by shifts in the CMS clock relative to the LHC bunch crossings and de-synchronizations introduced during hardware interventions during detector repairs. The global timing shifts caused by CMS clock timing drifts can be about 1 ns while that caused by hardware intervention can

be 3 to 5 ns. The calibration constants obtained for each crystal are of opposite sign to the average time measured from the reconstructed hits of each crystal. The calibration procedure begins with identifying timing shift reported in the CMS or ECAL detector running electronic (e-Log) book or the CMS or ECAL data acquisition monitoring (DQM) and followed by using reconstructed crystal hits or rechits from recently recorded or prompt data to measure the calibration constants for each channel. The validated calibration constants in an XML files are uploaded into the online configuration database with existing hardware settings for reprocessing of CMS full datasets used for physics analysis. This process is performed throughout the entire LHC proton-proton collision period each year. At the end of each calibration process, the set of calibration constants developed for that period of time is called its *interval of validity* (IOV). The data used in measuring the timing constants is specified by run range of events signifying a period over which proton-proton collisions occurred. During the entire LHC run period in 2011, a total of 17 IOVs were developed while during 2012 LHC run, a total of 44 IOVs were produced. The raw dataset used in producing the calibration constants consists of mostly superclusters with crystal hits from Level-1 triggered events of loosely triggered photons, electrons and hadrons with large electromagnetic contributions. Datasets with such events are called *ElectronHad* or *PhotonHad*. Rechits from these events must pass a selection criteria which include, the event time (an average over it's rechits) must be smaller than 5 ns, rechits must belong to a basic cluster whose transverse energy is atleast 2 GeV, the signal amplitude must not be lower than 26(47) or 100 (in LHC 2012) ADC counts (corresponding to an energy of about 1(3) GeV ) for rechits in EB(EE), the reconstructed rehit time must be within 5(7) ns from either side of zero in EB(EE) and to reduce the presence of anomalous crystal hits, the ratio of the sum of energies of the north, south, east and west neighboring crystals excluding the crystal with the highest energy to that of the energy of the highest energy crystal must be greater than 5% or equivalently  $1 - E_4/E_1 < 0.95$  (the *swiss-cross* variable). This swiss-cross variable is very useful for rejecting events with anomalous crystal energy deposits. The selected rechits are used to make a timing distribution for each channel requiring each channel to have at least 10 rechits.

After extracting the average time per crystal, the reverse of its value measured is the time calibration constants or inter-calibration coefficient used for timing alignment. The

variance represents the spread in the measurement of the calibration constant. For channels with less than 10 valid rechits, the average time of all the other channels is assigned to them as their inter-calibration coefficient. We validate these constants obtained by performing a closure test which involves applying the reversed values of these constants to the same or different set of events and showing that the measured average time over rechits per channel is 0 ns to within the accuracy of the calibration method and small event migration in the event sample. The event migration effects are of the order of 10 ps. The figures 4.5 show two dimensional distribution maps of the mean time for each crystal for all the 61,200 crystals in EB and 14648 crystals in EE showing the mean time distribution before (*top 3 plots*) and after (*bottom 3 plots*) calibration. Further details of the full IOVs produced for the entire LHC Run 1 can be found here [34].



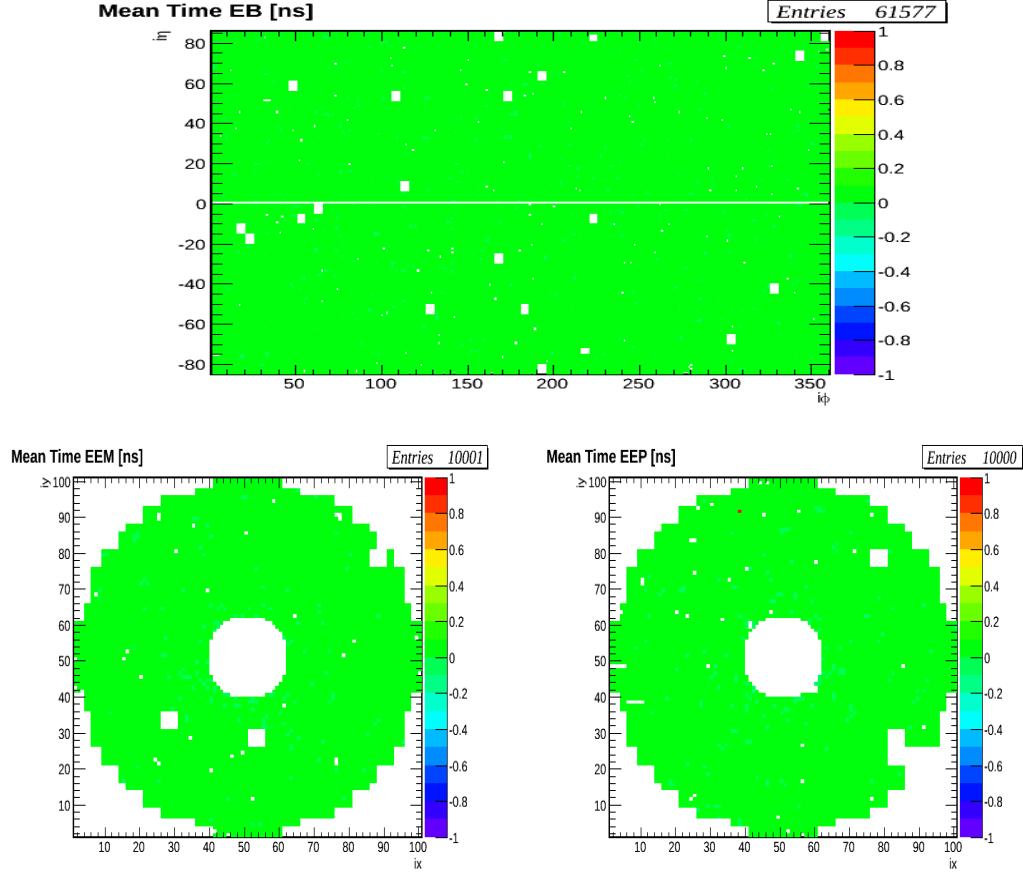


Figure 4.5: *Top 3*: Timing calibration maps showing the distribution of mean time for each channel/PbWO<sub>4</sub> crystal in EB (top) and EE (below: EE-(left), EE+(right)) before calibration. *Bottom 3*: Timing calibration maps showing the distribution of mean time after calibration. After calibration most crystals have an average time of zero(Green).

### 4.3.3 Hardware Timing Calibration

It is well known that timing offsets can be introduced during hardware repairs of ECAL front end electronics. These timing offsets are not easily adjustable during offline reconstruction as our method of offline timing calibration simply adjusts for the timing latency settings of the front end electronics using the online database. Hardware settings for readout electronics with timing offsets not properly aligned or calibrated can contribute to worsening of the timing resolution. The traditional method of correcting for this hardware timing offsets or latency during LHC stable proton beam collision has

been, in cases of an observed timing offset is to record enough data with the maladjusted hardware settings with timing offset, stop the entire CMS data taking process while LHC proton collisions are still ongoing, use the collected data to extract the hardware timing offsets, use these extracted timing offsets to adjust the hardware settings and finally continue with recording data with the CMS detector. These timing offsets are spotted and extracted during Data Quality Monitoring (DQM) and data certification hardware readout electronics performance routines. Although this method is reliable, it encourages long and intermittent data recording downtime as stopping the ECAL section of the CMS detector in order to adjust the settings of the hardware readout electronics leads to lost in data recording time which in some cases if the reason for reduced luminosity recorded by CMS compared to luminosity delivered by the LHC during LHC stable proton beams. To reduce this lost, we need an alternative method of adjusting the hardware timing offsets while reducing CMS data recording downtime. Our alternative approach to investigating and adjusting the hardware latency settings for timing offsets after the CMS or LHC machine maintenance intervention during technical stop or machine development was to use laser data instead of proton-proton collision data for performing timing adjustment. ECAL uses lasers to study and adjust for depreciated crystal energy resolution caused by loss in crystal transparency due to radiation.

The ECAL laser system comprise of two lasers, a 440 nm wavelength (close to peak emission for PbWO<sub>4</sub> crystals) laser for monitoring crystal transparency lose and a 796 nm wavelength laser for monitoring readout electronics chain from APDs to ADCs. Both lasers have jitter of less than 4 ns every 24 hours run. To account for this jittery effect, the timing from the laser is averaged over 600 event pulses. The time for each crystal from laser is expected to be the same as the time from data and is represented as  $T_{MAX}^{APD}$ . The ECAL laser system is also equipped with a fast acquisition card called MATAcq. The time for each channel recorded using the Matacq is also averaged over 600 event pulse denoted as  $T_{Matacq}$ . The difference in  $T_{MAX}^{APD} - T_{Matacq}$  between these two times averaged over the 25 crystals in a Clock and Control Unit (CCU) gives the time for each CCU,  $t_{CCU} = \langle T_{MAX}^{APD} - T_{Matacq} \rangle$ . In order to calculate the timing shift of 25 crystals belonging to the same Front End (FE) electronics, we monitor for any changes to this average value before ( $t_{CCU}^B$ ) and after ( $t_{CCU}^A$ ) hardware intervention during detector maintenance. The difference,  $\Delta t_{CCU} = t_{CCU}^A - t_{CCU}^B$ , after correcting for any global

shift, and averaged over all the 25 crystals, i.e.  $\langle t_{CCU}^A - t_{CCU}^B \rangle$ , gives the timing shift and calibration constant for that CCU and is done the same way for all the 68 CCUs in a given supermodule (SM) or front end detector (FED). Any global timing shift of all the crystals in a given FED is due to the laser light distribution in-homogeneity or evolution of the laser pulse due to different optical fiber supply of laser light to each CCU. Each FED or SM has 1,700 PbWO<sub>4</sub> crystals. The plots in figure 4.6 show our current observation status after monitoring for any shift in time within each CCU using laser. It shows the distribution of the CCU timing difference,  $\Delta t_{CCU}$  with its root mean squared (RMS) value for each CCU before and after machine intervention. Considering the subtraction of the global shift per FED also reduces the possibility of false timing shift in a given CCU. Using the average time subtraction method with laser data, we are able to measure each CCU timing shift to within 0.2 (0.5) ns EB (EE) in precision. This tool and procedure allow for adjusting the hardware timing settings during CMS data recording without the need for collision data. However some validation studies for this method is yet to be performed. In summary, we use crystal time from laser data to measure possible hardware timing offsets and use these timing offsets to provide new hardware settings prior to proton-proton collision. This adjustment can be performed online or *in-situ* by using the ECAL readout electronics condition database system. The full procedure including technical details for performing hardware latency adjustments online using collision data or laser data is well described in [35].

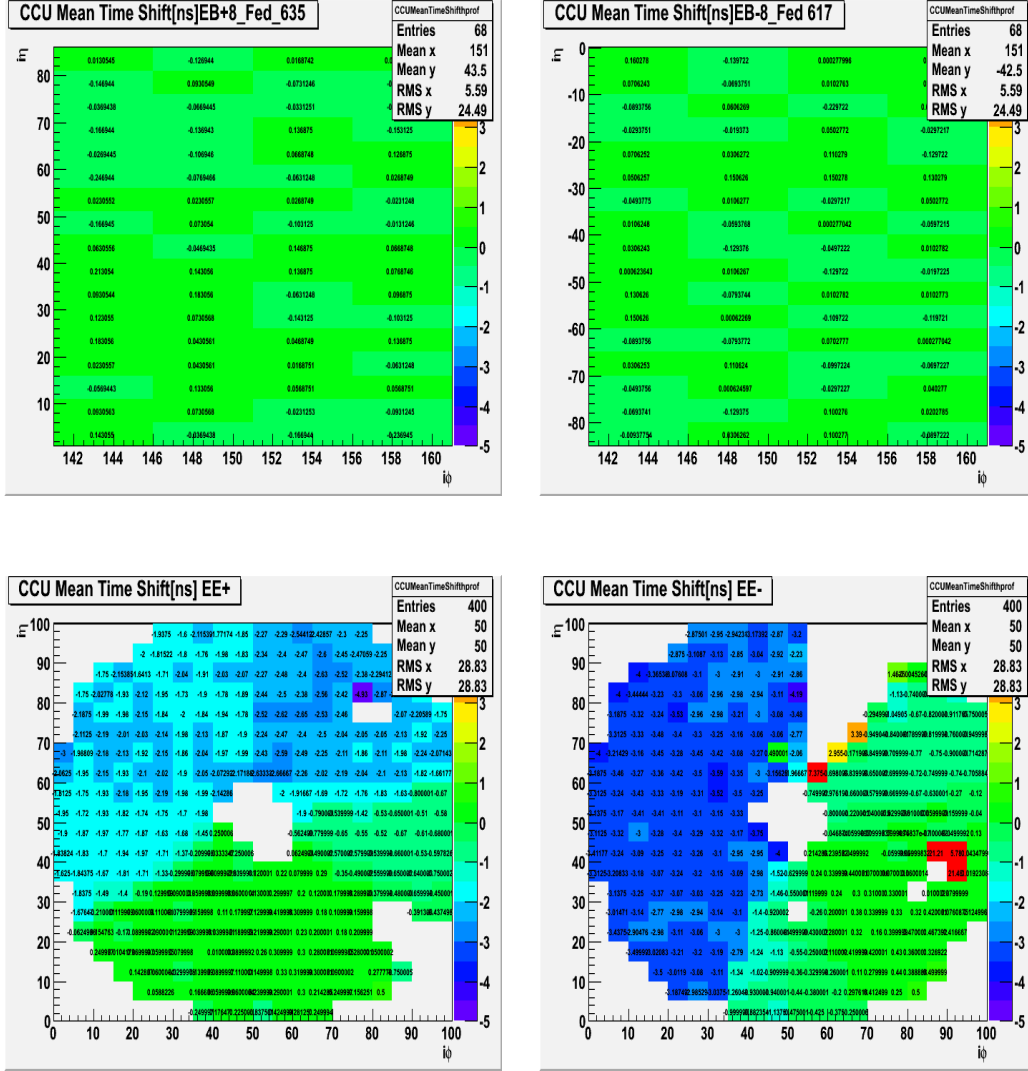


Figure 4.6: *Top:* Crystal mean time distribution for crystals in readout electronics  $EB \pm 8$ . Crystal time obtained from Laser data. *Bottom:* Clock and Control Unit (CCU) mean timing shift distribution of readout electronics of  $EE+$  and  $EE-$ . The adjustment for global timing shift per FED due to difference in light source for each CCU has been shown to reduce the possibility of CCU showing false timing shift. The figures show  $\Delta t_{CCU}$  distributions after the global shift has been removed.

#### 4.3.4 Timing Bias

The ratio algorithm described in Section 4.2 for extracting the amplitude and time of an event signal from ten digitized samples of a crystal or channel is assumed to perform

efficiently well for all energies of the hits. However, during LHC Run 1 proton-proton collision, it has been observed that this is not the case, especially for very energetic particles. An inherent timing bias is introduced by the MGPA for incoming electromagnetic particles with energy above the gain transition point. The energy deposited by an incoming particle on a crystal is recorded as an ADC count,  $A$ , which is the signal amplitude of the recorded pulse shape. This ADC count can be converted into energy in GeV through some conversion factors and adjustments. The full conversion from ADC counts to GeV of a crystal energy is expressed using equation 4.5.

$$E_i = G \cdot S_i(t) \cdot C_i \cdot A_i \quad (4.5)$$

Where  $G$  is an ADC-to-GeV conversion factor equal to 0.039(0.063) in EB(EE).  $C_i$  is the inter-calibration coefficients accounting for individual channel response and  $S_i(t)$  is the correction term (usually from laser data) accounting for radiation-induced channel response.  $S_i$  changes over time. The Gain 1 transition point is at 4096 ADC counts corresponding to 159.744 GeV in EB and 258.048 GeV in EE. The subsequent Gain 6 and 12 transitions are at energy values of TeV energy level. The bias in timing introduced by these gain transitions cannot be calibrated at hardware, so we developed a method of adjusting the timing measurements for the timing bias at the CMS event reconstruction level. Using reconstructed hits with similar selection as our offline timing calibration, selected hits are also required to be part of a basic cluster (usually  $3 \times 3$  or  $5 \times 5$  matrix of crystals). These hits must have amplitude with channel noise consideration above 10 ADC counts. We reject hits with very large timing biased and large swiss-cross variable beyond our selection threshold (0.99). A distribution of the hit time against its amplitude is plotted and then sliced in bins of amplitude. Bins containing at least 7 hits are fitted using a Gaussian function constrained within  $\pm 7$  ns. The average(mean) and standard deviation(RMS) from these distributions is plotted against their corresponding amplitude or energy to give a distribution of mean and standard deviation against amplitude. This procedure is performed for different *Modules* or pseudo-rapidity ( $\eta$ ) range starting from  $\eta = 0$  which is *Module* 1 in barrel to  $\eta = 3$  for high-eta in end-cap. Figure 4.7 shows the mean against energy distribution for different reconstruction CMS Software (CMSSW) release versions where these timing bias corrections have been

applied (CMSSW5XY) and have not been applied (CMSSW44X) during object reconstruction.

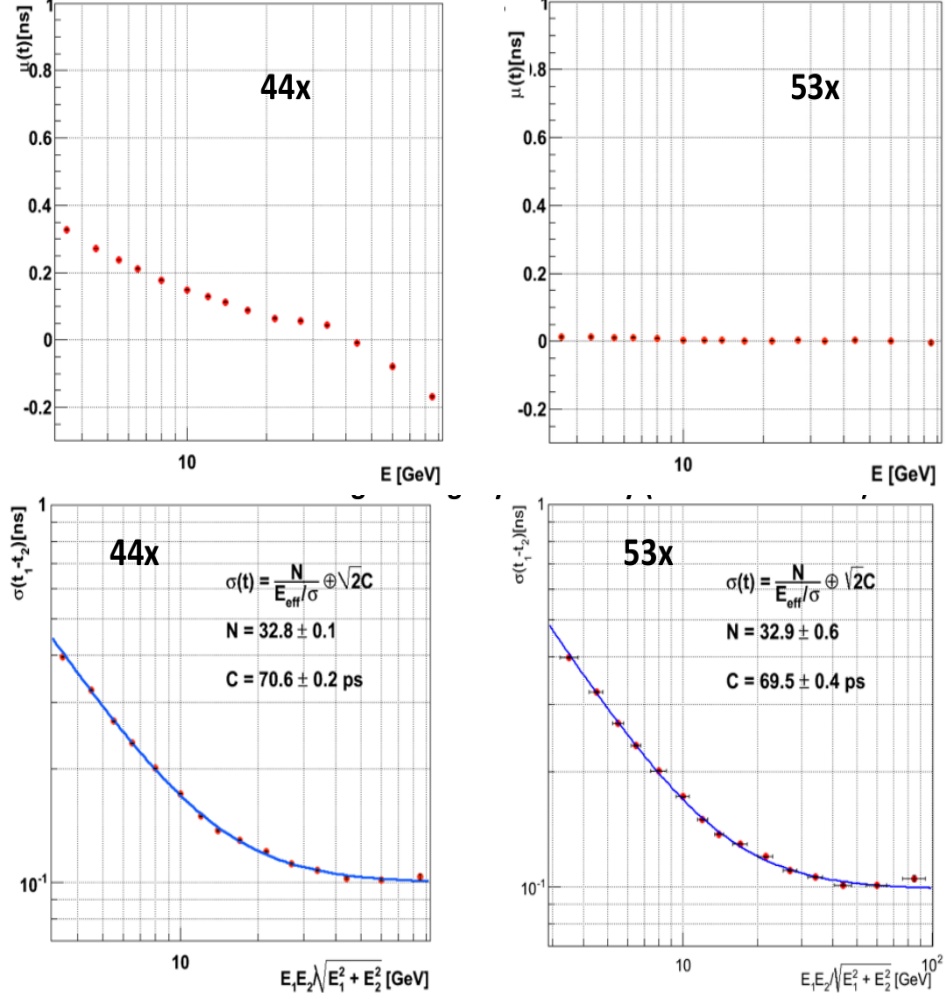


Figure 4.7: Distribution of mean time ( $\mu$ , top row) and timing deviation ( $\sigma$ , bottom row) as a function of crystal energy for EB prior (left) and after (right) timing bias corrections depending on amplitude have been applied.

We investigated for dependence of the timing measurements on the crystal position in ECAL from  $\eta = 0$  to  $\eta = 3.142$ . The results in figure 4.8 show no crystal position or  $\eta$  dependence. There are other timing biases of the order of about 100 ps have been observed in the difference in time for crystals belonging to different electronics. Such timing bias are not yet understood.

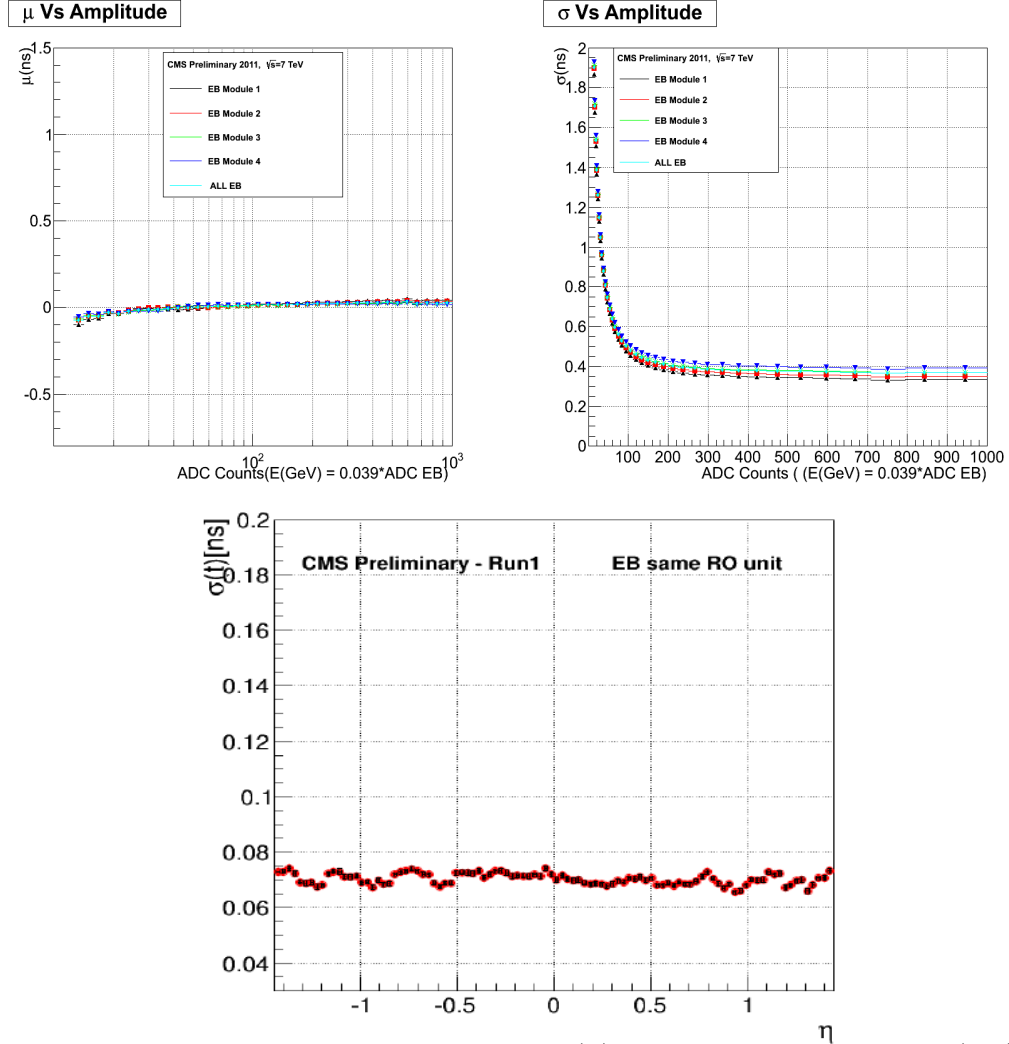


Figure 4.8: *Top row:* Distribution of mean time ( $\mu$ ) as a function of amplitude (left) and resolution ( $\sigma$ ) as a function of amplitude (right) for different pseudo-rapidity regions in the barrel. *Bottom:* All modules in EB combined timing resolution as a function against  $\eta$  crystals in the same readout electronics in barrel (EB).

## 4.4 Electromagnetic Calorimeter Timing Performance

We study the performance of timing measurements by ECAL crystals using well studied physics processes like the decay of a Z boson to an electron pair, i.e.  $Z \rightarrow e^-e^+$ . We use the difference in the arrival time of both electrons at ECAL crystals, which in principle should be zero, to evaluate ECAL timing measurement performance. This performance is expressed by using the standard deviation,  $\sigma_{eff}$ , of the difference in arrival time of both electrons. The crystal arrival time for each electron is the time of the seed crystal ( $t_{seed}$ ) of the electron energy super cluster. The difference in the seed time between both electrons after correcting for contributions from the bending of the electron travel path inside a strong CMS magnetic field of 3.8 T,  $t_{electron1} - t_{electron2} = t_{seed1} - t_{seed2}$ , gives a good estimate of the timing resolution performance of the ECAL crystals. Figure 4.9 shows time difference of both electrons adjusted for time of flight corrections while figure 4.10, shows the time resolution obtained from the time distribution of the seed crystal time without correcting for the bending of the flight path contributions.

Despite this good timing resolution of about 232 ps in EB and 384 ps in EE, there are other sources contributing to poor timing resolution compared to test beam results of  $\leq 100$  ps. These sources include, displaced collisions because “partons” (quarks inside a proton) in the proton bunches did not collide at exactly the same nominal interaction point (IP), the fact that proton-proton collisions developed over the full duration due to overlap of the proton bunches and timing biases from different electronics and crystal-to-crystal intercalibration.

Without adjusting for contributions from individual proton collisions across the entire proton bunch luminous region of nearly 5.5 cm(referred here as *proton collision time* of about  $\sigma(t_{colision}) = \sigma(t_Z) = 183$  ps) the measured ECAL timing resolution is 232 ps in EB and 384 ps in EE. When adjusted for this contribution, the timing resolution is about 142 ps for EB and 338 ps in EE. The electrons used for this study has been selected such that they have a transverse energy bigger than 10 GeV and reconstruct the Z mass, within,  $60\text{ GeV} < m_{inv}(e_1, e_2) < 150\text{ GeV}$  to make a good Z boson candidate.

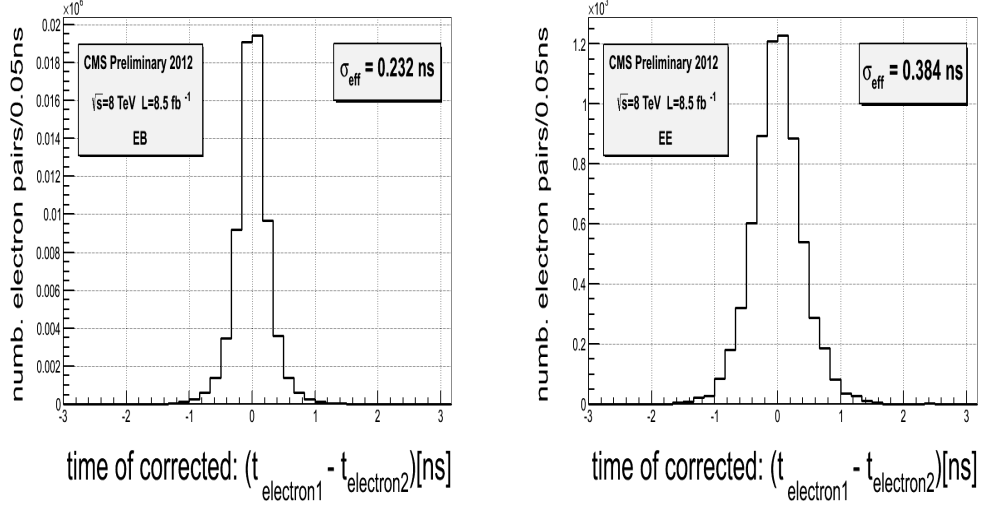


Figure 4.9: Ecal time difference between the two reconstructed electrons in  $Z \rightarrow e^-e^+$  decay. The electron time is the seed (crystal with highest energy deposit) time with additional correction due to the time of flight of the electron in EB and EE

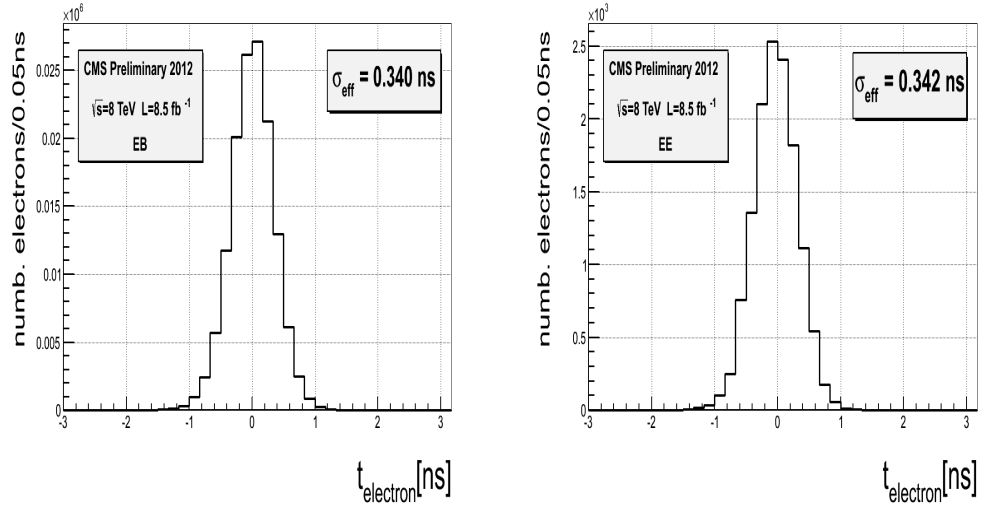


Figure 4.10: Ecal absolute time of a single reconstructed electron in  $Z \rightarrow e^-e^+$  decay. The electron time is the seed (crystal with highest energy deposit) time of the electron in EB and EE

In Figure 4.11, we show the comparison of ECAL timing resolution obtained using

events with  $Z \rightarrow e^-e^+$  the case where both crystals belong to different frontend electronics (*right*) to where both crystals belong to the same electronics(*right*) and observe the 100 ps bias due to different electronics. The timing resolution from LHC RUN1 shown in figure 4.11 compared to timing resolution from test beam shown in figure 4.4, shows that we are yet to achieve the level of ECAL timing resolution obtained during test beam. Nevertheless, the current timing resolution of  $\sigma(t) \leq 400$  ps is good for using ECAL timing measurements to study physics processes with photons and electrons produced from the decay of long-lived particles. Table 4.1 shows the summary of the ECAL timing resolution comparing the absolute and single precision timing resolution studied using events with Z decay for 2011 and 2012 of the entire LHC Run 1.

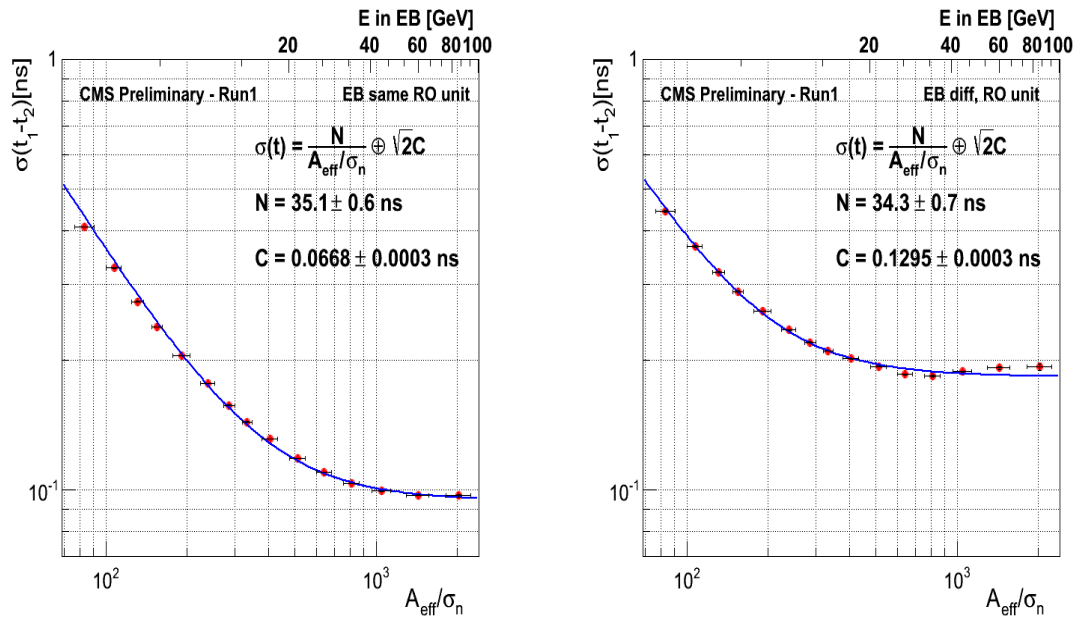


Figure 4.11: Timing resolution from: *left*: Two most energetic crystals in the same readout unit, *right*: Two most energetic crystals belonging to different readout units, as a function of effective amplitude( $A_{\text{eff}} = A_1 A_2 / \sqrt{A_1^2 + A_2^2}$ ) normalized to noise in EB. Both crystals are from reconstructed electrons in  $Z \rightarrow e^-e^+$  events.

**ECAL Timing Resolution**

| <b>2011</b> |                                     |   |
|-------------|-------------------------------------|---|
|             | <b>Absolute Time</b>                | <b>Single Precision</b>                             |
|             | $\sigma_{eff}(t_{seed})[\text{ps}]$ | $\sigma_{eff}(t_{e1} - t_{e2})/\sqrt{2}[\text{ps}]$ |
| <b>EB</b>   | 376                                 | 190   |
| <b>EE</b>   | 356                                 | 282   |
| <b>2012</b> |                                     |   |
|             | <b>Absolute Time</b>                | <b>Single Precision</b>                             |
|             | $\sigma_{eff}(t_{seed})[\text{ps}]$ | $\sigma_{eff}(t_{e1} - t_{e2})/\sqrt{2}[\text{ps}]$ |
| <b>EB</b>   | 340                                 | 164   |
| <b>EE</b>   | 342                                 | 272   |

Table 4.1: ECAL timing resolution absolute time and single precision for 2011 and 2012 of LHC Run 1

# Chapter 5

## Event Reconstruction

### 5.1 Physics Object Reconstruction

Event reconstruction is the process of constructing physics candidate objects like electrons, photons, muons, jets using raw data in the form of digitized hits or *digsis* from the DAQ. An event together with its constituent physics objects is reconstructed using information from all CMS subdetectors with some selection requirements. The reconstruction is implemented in a software. Reconstruction begins with local reconstruction performed with hits from a particular subdetector called *rechits* then proceeds to a global and final reconstructions where rechit information from the entire CMS detector is used. Rechits are typically position measurements (from hits in strips or pixels) in tracking type subdetectors (Muon chamber and Tracker) and energy deposits or hits from calorimetry subdetectors (ECAL and HCAL). For example, in the tracker, the local reconstruction algorithm search for pixel or strips with hits exceeding a threshold and use them as seeds for clusters in the calorimeters while in the Muon Cathode Strip Chambers (CSCs),local reconstruction provides position and time of arrival of muon hits from the distribution of charge induced on the cathode strips. For Electromagnetic (ECAL) and Hadronic (HCAL) calorimeters, local reconstruction identifies, the position, arrival time and energy of localized electromagnetic and hadronic energy depositions respectively. The typical software package for local reconstruction in the tracker is the *RecoLocalTracker* since for reconstructing tracks only local modules of the tracker subdetector are used. During global reconstruction, rechits from several subdetectors

combined serves as input for producing higher-level objects like charge particle tracks using clustering, tracking and fitting algorithms. For example, in ECAL and HCAL, global reconstruction provides tracks links matching to clusters in ECAL and HCAL energy clusters to produced Calorimetric Towers (CaloTower) which have definite position in  $(\eta, \phi)$  plane in the calorimetric systems. These calotowers are fed into Jet reconstruction for reconstructed *jets*. In the Tracker, global reconstruction uses tracker hits and track segments for *Kalman fitter* algorithm which builds particle trajectories with selections in the form of a  $\chi^2$  cut applied to reject hits unlikely to be associated with tracks. The final and full reconstruction combines these reconstructed objects from individual subdetectors to produce higher-level reconstructed objects used for high-level triggering and physics analysis. Additional selection requirements may be applied to arrive at candidate physics objects like an electron, a photon and jet(s) belonging to a proton-proton collision event.

### 5.1.1 Supercluster Reconstruction

The basis of all object reconstruction is the supercluster or basic cluster. Electromagnetic showers of photons and electrons are deposited in several crystals. Usually about 94% (97%) of the incident energy is deposited in a  $3 \times 3$  ( $5 \times 5$ ) matrix crystals in the  $(\eta, \phi)$  plane. The presence of 3.8 T magnetic field, material in front of the calorimeter causes bremsstrahlung electrons and converted photons to deposit their energy in calorimeter in the form of small clusters spread in  $\phi$ . This energy is recovered using clustering algorithms where by starting with a seed crystal containing the maximum of energy, superclusters (clusters of cluster) are built within a narrow window in  $\eta$  by summing the crystal energy along the  $\phi$  which is the direction of energy spread due to the magnetic field. Figure 5.1 shows a simple picture how these super clusters are built.

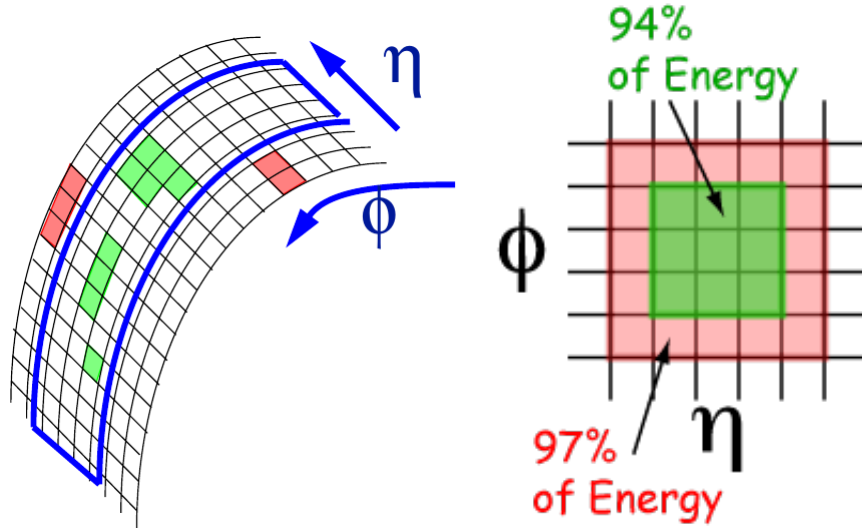


Figure 5.1: Superclustering algorithm in ECAL for both hybrid (EB) and island (EE) clustering algorithms.

There are two major clustering algorithms used:

- **Hybrid Superclusters:** This algorithm is used to make super-clusters in the barrel (EB). It takes advantage of the  $\eta - \phi$  geometry of barrel crystals by taking a fixed 3 or 5 crystals in  $\eta$  and dynamically search and sum separate crystals energy along  $\phi$ . The Hybrid algorithm takes advantage of our knowledge of the lateral shower shape along the  $\eta$  direction. The supercluster is made of basic clusters. The figure 5.2 shows an example of how the hybrid clustering algorithm performs clustering.

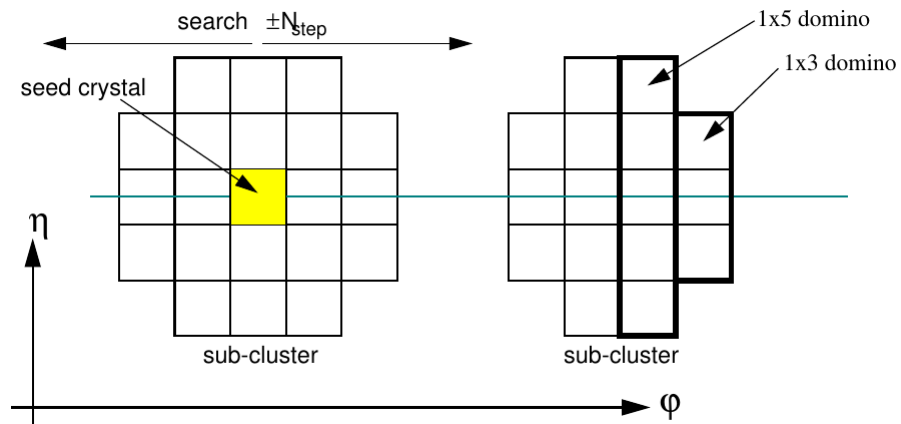


Figure 5.2: Superclustering in ECAL for hybrid clustering algorithm in barrel.

- **Island Basic cluster or Superclusters:** After Local reconstruction leading to the production of *EcalRecHits*, the island algorithm is applied in both barrel and endcap (EE)to produce superclusters. This algorithm begins by finding the seed crystal with a local energy maximum above a certain threshold. from the seed position, adjacent crystals are examined starting fist along  $\phi$  and then in  $\eta$  adding crystal energy to cluster until a crystal belonging to another cluster or crystal that has no readout is reached. For each crystal to be added to the cluster, the crystal must contain a rechit with positive energy, the crystal has not been assigned to another cluster and the previous crystal added in the same direction has higher energy. These non-overlapping clusters are then made into superclusters. A search is performed for the most energetic cluster and then collect all the other narrow window clusters in  $\eta$  and wide window in  $\phi$ . The figure in 5.3 provides a pictorial view of how the island algorithm works.

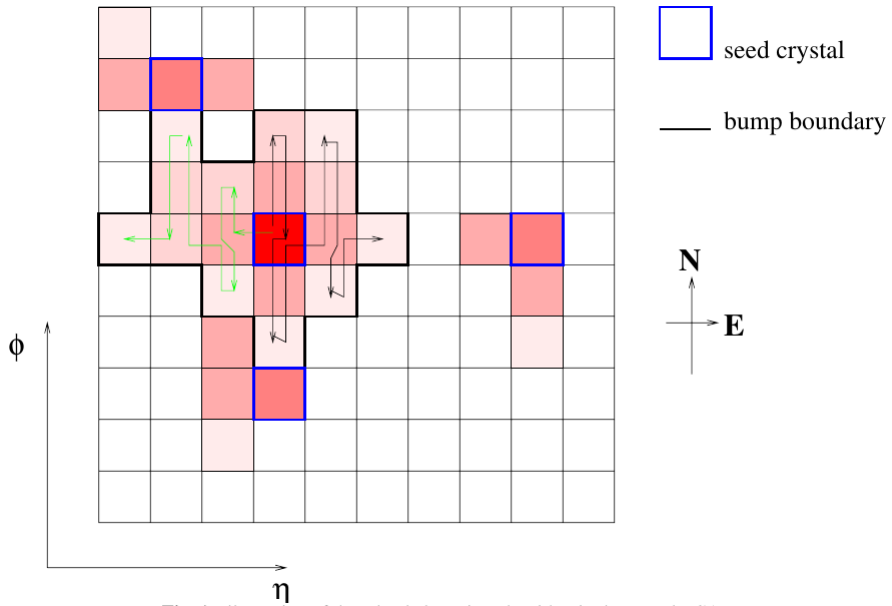


Figure 5.3: Superclustering in ECAL for Island clustering algorithm in barrel.

### 5.1.2 Vertex and Track Reconstruction

The reconstruction of track candidates of a charge objects such as an electron begins by selecting an initial parameter which a pair or triplet of hits constraint by the interaction region or a given beam spot in the pixel detector. This if followed by the search of other pairs of hits in pairs of tracker layers as well as hit pairs in the strips or strips an pixels to allow for reconstruction of vertices beyond the pixel volume. To prevent the combination factor and reduce fake rates when using the Combinatorial Track Finder (CTF), hits are selected in a small restricted region in  $\phi$  compatible with a super-cluster in the ECAL. This seeding strategy is known is *tracker-driven*. Another powerful approach is to start with the ECAL super-cluster and match the seed super-cluster hits back towards hit in the tracker particular the pixel. It is term *ECAL-driven* seeding and this super-cluster-driven pixel seed finding presents advantage for comparable reconstruction efficiency and increasing the purity by reducing the presence of fake tracks in the sample of candidate tracks. This is particularly useful for electron reconstruction and is used by the Higher Level Trigger (HLT) for tagging primary electron-like objects.

In selecting the seed cluster, the cluster which initiates the bremsstrahlung recovery procedure, this seed is required to have a minimum Transverse Energy ( $E_T$ ) of 1 GeV is  $E_T > 1$  GeV. This requirement allows the reconstruction of electron super-cluster for with low Transverse Momentum ( $p_T$ ). In a study using back-to-back  $e^+e^-$  events, a supercluster reconstruction efficiency of about 93% is achieved for electron  $p_T^e = 10$  GeV/c when  $E_T^{seed} > 1$  GeV. Using this seed cluster, the hits in the pixel layer are predicted by the propagation of an energy weighted mean position of the super-cluster backward through the magnetic field under the charge hypothesis( positive or negatively charged particle) towards the pixel detectors. A first compatible hit is looked for in the inner most (barrel) of the pixel detector within a loose  $\Delta\phi$  window adapted to the uncertainty of  $\phi$  measurement of the super-cluster ( $\phi_{SC}$ ) and loose  $\Delta z$  interval adapted to the spread of the interaction vertices. In case no hit is found in the innermost pixel layer, the first hit is looked for in the next-to-innermost layer. Once a compatible hit is found, a new estimate of the  $z_0$  on the  $z$  coordinate of the primary track vertex is calculated by combining the pixel hit found and the information from the calorimeters in the  $RZ$  plane. Using this predicted trajectory, we propagate once more to look for the second pixel hit in the next pixel layer(s).

Starting from this seed ( pair hits), a trajectory is created. This trajectory creating begins by first searching for the next silicon layer hits, then extrapolation is performed using a model based on the non-gaussian nature of energy losses by Bethe and Heitler, then Gaussian Sum Filter (GSF) algorithm is used to perform a fit on the track. This procedure is repeated until the last trackers layers unless no hit is found on the subsequent layers. If many hits are found on a compatible layer, many candidate tracks are built in parallel and using the  $\chi^2$  from the GSF fit, the best two GSF track candidates with the smallest  $\chi^2$  are selected and kept. A minimum of five hits is required to create a track. The difference between electrons and photons at this stage is that photons because they are neutral have no pixel hits and as a result have no reconstructed tracks. Thus, from the ECAL driven track reconstruction, super-clusters with no pixel matched seeds fall into the photon candidate sample collection. However, 50% of the time photons due to the tracker material will convert into  $e^+e^-$  conversion pairs. These are known as *converted photons*. These converted photons are usually low  $p_T$  photons and don't always travel to the ECAL but those that do and if happen to arrive late can be candidates for clear signal of physics beyond the SM. Because electrons have a GSF tracks , they are normally referred to as GSF electrons. Using the selected GSF tracks, important particle kinematic information such as the vertex pseudo-rapidity ( $\eta$ ), the track  $p_T$  and the vertex  $\phi$  coordinate are well measured with good resolution.

The primary interaction vertex in an event is reconstructed from a collection of tracks. A group of tracks in clusters based on the  $z$  coordinate position of their track with respect to the point of closest approach to the beamline. The track clusters, as previously mentioned are fitted with an adaptive vertex fitter and the tracks are assigned weights between 0 and 1 based on their closeness in proximity to the common vertex. This ensures a dependence on the primary vertex resolution to the number of tracks used in the fitting and  $p_T$ . This primary vertex resolution dependence on the number of tracks is studied using tracks in an event with just one vertex while for  $p_T$ , the resolution is studied for a number of tracks with different average  $p_T$  of tracks in the vertex. It is important to recall that tracks can only be reconstructed up to  $|\eta| < 2.5$  which defines the tracker volume, beyond which these objects are assumed to have no tracks.

### 5.1.3 Photon or Electron Identification

Electron and photon identification depends of the ability to reject minimum biased events, underlying events or Pile Up (PU) produced from multiple proton-proton interactions, electrons embedded in hadronic showers or Jets and anomalous events. Pre-selections are applied at the level of track seeding and clusters so as to reject tracks from underlying or low energy proton-proton collision events called Pile Up (PU). Based on kinematic and nature of electromagnetic showers in the ECAL, some variables have been developed and their performance studied for optimal identification and isolation of electrons and photons. This is in compatibility with the fact that the two electron reconstruction algorithms compliment each other in specific  $p_T$  range. The tracker seed driven algorithm is more suitable for low  $p_T$  electrons as well as better performance for electrons inside jets while ECAL seed driven algorithm which selects seeding clusters with transverse energy  $E_T > 1 \text{ GeV}$  is optimised for isolated electrons  $p_T > 10 \text{ GeV}/c$  up to  $p_T$  relevant for the mass of  $Z$  or  $W$  bosons.

The goal of the ECAL is to obtain the best estimate of energy deposited by an electron or photon in the ECAL,  $E_{e/\gamma}$ . This from the detector point of view, the energy deposit is given as:

$$E_{e/\gamma} = F_{e/\gamma} \cdot [G \cdot \sum_i S_i(t) \cdot C_i \cdot A_i] \quad (5.1)$$

where  $A_i$  is the signal amplitude in ADC counts,  $C_i$  is the inter-calibration coefficient,  $S_i(t)$  is the time-dependent corrections for response variable usually obtain from laser,  $G$  is the global scale calibration allowing one to move form energy in ADC counts to GeV and  $F_{e/\gamma}$  is the particle energy corrections for geometric, clustering and other effects. The sum is over all the crystals belonging to the photon or electron super-cluster. In order to measure and reconstruct the true energy of the detected particle, energy corrections depending on  $\eta$  such as  $F_{e/\gamma}$  are applied at the level of super-cluster reconstruction to account for detector effects hence better identification of particles, in this case electrons and photons. Figure 5.4 shows energy scale and resolution obtained when these energy corrections are applied compared with when no corrections are applied. Figure 5.5, shows the scenario for applying these corrections at the level of super-cluster reconstruction which at this stage are only electromagnetic objects.

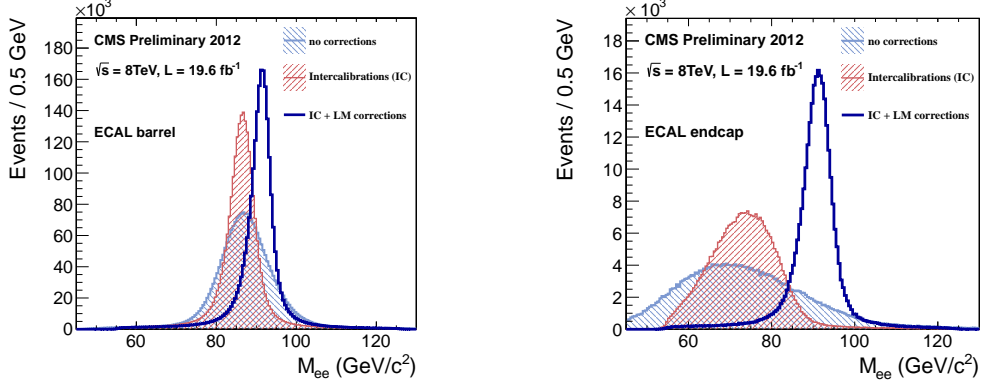


Figure 5.4:  $Z \rightarrow e^+e^-$  mass plot showing resolution and energy scale that is obtained from applying energy scale corrections to account for intrinsic spread in crystal and photo-detector response and time-dependent corrections to compensate for channel response loss for EB (right) and EE (left)

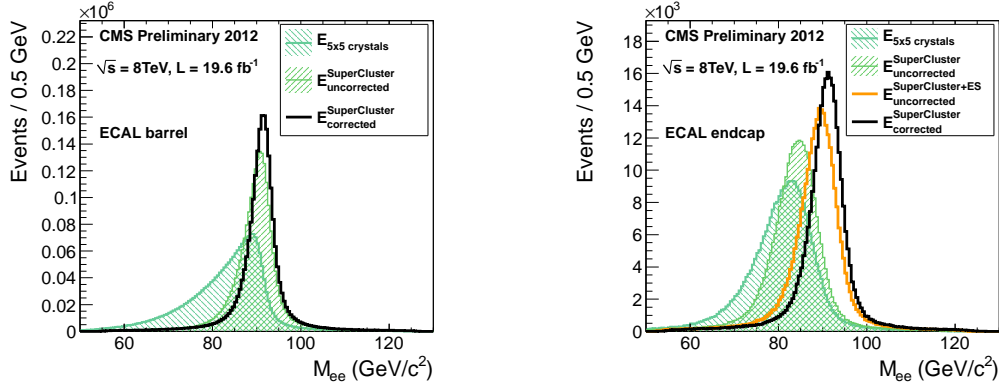


Figure 5.5: Super-clusters showing resolution and energy scale that is obtained from applying energy scale corrections for EB (right) and EE (left)

With these electron or photon candidates, further selections using variables constructed from information on the spread of the electromagnetic shower in  $\eta$  and  $\phi$ , the ratio of the energy deposited in ECAL and HCAL, the track  $p_T$  and ECAL  $E_T$  to further identify photons and electrons. Pre-electron candidates based on cut elections such as minimum transverse energy,  $E_T > 4$  GeV,  $\eta$  and  $\phi$  geometrical matching;  $\Delta Eta < 0.02$ ,  $\Delta\phi < 0.1$  and a cut on Ratio of hadronic to electromagnetic energy cluster:  $H/E < 0.2$  is enough to suit physics analysis, however, additional elections and identification criteria are added depending on the purpose of the particular analysis to fully defined an electron or photon. These identifications and isolation criteria can also be categorised

in terms of flavours as being very loose (VL), loose (L), medium (M) and tight (T). The typical variables used for electron and photon identification are defined as follows:

- Ratio of energy of HCAL behind super cluster to super cluster energy:  $H/E$
- Energy momentum matching variables between energy of the super cluster or of the super cluster seed and electron track measured momentum at the vertex or at the calorimeter:  $E/p_{in}$ ,  $E_{seed}/p_{in}$ ,  $E_{seed}/p_{out}$
- Geometrical matching between the electron track parameters at the vertex extrapolated to the super cluster and the measured super cluster position:  $\Delta\eta_{in}$ ,  $\Delta\phi_{in}$ .
- Calorimeter shower shape variables: the width of the ECAL cluster along the  $\eta$  direction computed for all the crystals in the  $5 \times 5$  block of crystals centered on the highest energy crystal of the seed cluster,  $\sigma_{in,\eta}$  and the ratios of the energy sums over  $3 \times 3$  and  $5 \times 5$  matrices centered on the highest energy crystal of the seed cluster:  $R_9 = E_{3 \times 3}/E_{5 \times 5}$  or  $R_9 = \sum E_9 / \sum E_{Supercluster}$ . This  $R_9$  variable makes a good separation between unconverted photons (energy not spread in tracker) and converted photons (energy spread by B-field before reaching ECAL).
- Bremsstrahlung fraction:  $(track\ momentum\ at\ vertex - track\ momentum\ at\ ECAL) / track\ momentum\ at\ vertex$ .
- $1/E(\text{Super cluster}) - 1/p(\text{track at vertex})$

Due to the very high photon conversion rate s as a result of the tracker material in front of the ECAL cuts like:

- Calorimeter shower shape:  $R_9$
- Impact parameter:  $d0$ , minimum separation of the electron track computed with respect to the reconstruction vertex.
- Missing Hits: Number of cross layers without a compatible hits in the back-propagation of the track to the beam-line.

Isolation variables in addition to the identification variables are used to improve on the performance of identification. Below are the following isolation variables as defined and used by the CMS:

### **Electron Photon Isolation**

- Tracker Isolation: sum of  $p_T$  of tracks with  $p_T > 0.7 \text{ GeV}/c$  and maximum distance to the vertex of 0.2 cm in a cone of 0.3 with an inner veto cone of 0.04.
- ECAL Isolation: sum of energy of ECAL RecHits with a Jurassic footprint removal (Jurassic width of about 1.5 crystals) in a cone of 0.4 with veto cone of 3 crystals. A RecHit noise cut of 0.08 GeV in energy (E) in barrel and 0.1 GeV in transverse energy ( $E_T$ ) in the endcap is applied.
- HCAL Isolation: sum of HCAL Calorimeter Towers in a 0.4 cone with a 0.15 veto cone.

In general the major difference between an electron and a photon as identified by the CMS detector is that electrons which have no pixel strip hits are automatically classified as photon candidates and further isolation and shower shape variables are used to arrive at the ultimate photon as required by a given analysis. Table ?? shows the Simple Cut-based selection criteria variables and cut thresholds used to identify electrons and photons in the CMS detector.

### **Particle Flow Algorithm**

An alternative criteria for reconstructing and identifying physics objects in the CMS detector which is now widely acceptable is the *particle flow* (PF) algorithm.

The particle flow algorithm takes into consideration information from every sub-detectors like the tracker, ECAL, HCAL and muon section before identifying a particular physics objects. The goal of this algorithm is to reconstruct higher level physics objects like Jets, missing transverse energy (MET), and the identification of tau ( $\tau$ ) and b-jets by making use of the content of these objects in terms of more fundamental objects like electrons and photons or super clusters and tracks. The algorithm constitutes of steps like calorimeter clustering, tracking and extrapolation to calorimeters, muon identification, electron pre-identification, linking of topological elements and finally particle

identification and reconstruction. The result is a list of reconstructed particles consisting of photon, charge hadron, neutral hadron, muon and electron. From this list high level objects such as jets, MET and taus can be reconstructed. In the case of electrons reconstructed using the PF algorithm, tracks, electron energy seeds, 4-momentum, super cluster energy calibration, Bremsstrahlung tracks are used as base objects to reconstruct the entire electron. The PF is very useful in MET reconstruction where information about all the particles making up a single event is necessary to calculate MET.

### Simple Cut Based Electron Photon Identification

| ID Variable                        | Electron             | Photon  |
|------------------------------------|----------------------|---|
| $H/E$                              | 0.05(EB), 0.10(EE)   | 0.05  |
| $ \Delta\eta_{in} $                | 0.005(EB), 0.007(EE) | 0.015(EB)   |
| $ \Delta\phi_{in} $                | 0.09(EB), 0.09(EE)   | N/A   |
| $\sigma_{i\eta i\eta}$             | 0.01(EB), 0.03(EE)   | 0.011(EB),<br>0.03(EE)                                    |
| Pixel Veto                         | No                   | Yes   |
| $ d0 (vertex)$                     | 0.02(EB), 0.02(EE)   | Veto  |
| $ dZ (vertex)$                     | 0.1(EB), 0.1(EE)     | 0.02 (cm)(Veto)   |
| $ 1/E - 1/p $                      | 0.05(EB), 0.05(EE)   | N/A   |
| PF isolation / $p_T$ (cone dR=0.3) | 0.15(EB),0.10(EE)    | N/A   |
| ECAL Isolation                     | same                 | $4.2 + 0.006 * E_T^\gamma +$<br>$0.183 * \rho(\text{EB})$ |
| HCAL Isolation                     | same                 | $2.2 + 0.0025 * E_T^\gamma +$<br>$0.062 * \rho$           |
| TRACK Isolation                    | same                 | $2.0 + 0.001 * E_T^\gamma +$<br>$0.0167 * \rho$           |
| Rho corrected PF photon isolation  | N/A                  | $1.3 + 0.005 * p_T^\gamma(\text{EB})$                     |

Table 5.1: Simple Cut-Based criteria for High energy electron and photon identification in CMS

### 5.1.4 Muon Reconstruction

The are three different types of muons reconstructed using the muon system detection all making up one huge collection of muons. They are Stand-alone, Global and Tracker Muons. Reconstructed hit positions within each DT and CSC are matched to form “segments” which are then collected and matched to generate seeds used as starting point for actual track fit of DT, CSC, and RPC hits. The resulting product of the fit in the muon spectrometer is a “stand-alone muon”. “Global muons are formed when these stand-alone muon tracks and matched to tracker tracks in the tracker while ”tracker muons“ are muon objects reconstructed starting form silicon tracker tracks compatible with segments in the muon chambers. Using muon isolation variables defined using the calorimeter and tracker tracks, a collection of muon objects is identified in CMS. Thus is summary, stand-alone muons contain only hit position information from the muon chambers, global muons contain this information in addition to tracker information while Tracker muons are muons reconstructed starting with information from the inner tracker which is matched with calorimeter and muon chamber information. Using the beam spot as a constraint ensures that muons produced from proton-proton collision are distinguished from those produce from cosmic rays known as *cosmic muons* or from beam splash/gas 150 m upstream proton beam dump known as *beam Halos*. The 2 T **B**-field with a multi-stage flux-return yoke shields the muon detectors from hadrons ensuring that the measured particles can be identified as minimum ionizing muons. The barrel muon detector consists of 4 stations forming concentric cylinders  $|\eta| < 1.2$  around the beam line while the endcaps system consists of 468 cathode strip chambers (CSC) arranged in groups as 72 ME1/1, 72 ME1/2, 72 ME1/3, 36 ME2/1, 72 ME2/2, 36 ME3/1, 72 ME3/2and 36 ME4/1 and the 72 ME4/2. A muon in pseudo-rapidity range of  $1.2 < |\eta| < 2.4$  crosses a total of 4 CSCs. Muons in the encaps-barrel overlap region;  $0.9 < |\eta| < 1.2$  are detected by both the barrel drift tubes (DT) and endcaps CSCs while in bother barrel and endcaps RPSc are used for triggering. RPCs are capable of tagging the time of an ionizing event in a much shorter time than the 25 ns between 2 consecutive LHC Bunch Crossings as a result triggering based on RPC can be used to unambiguously identify the relevant Bunch Crossing to which a muon track is associated even in the presence of high rate and background expected in the LHC.

### Cosmic and Halo Muons

Muons produced centrally or from proton-proton collision are reconstructed a bit different from other muons. Halo muons originating from machine-induced particles travelling along the beam line and cosmic muons originating from cosmic rays require global information in order to distinguish them from centrally produced muons. Both cosmic and halo muons are considered to be background muons in most physics analysis. The stand-alone muon reconstruction software suited from reconstructed muons from proton-proton collision assumes these muons to be moving radially outward in seen in figure ?? while cosmic muons originate from the outside of the CMS detector and can traverse only a small part of a detector depending on its energy and direction. Figure 5.6 show an illustration of different trajectories for the different types of muons.

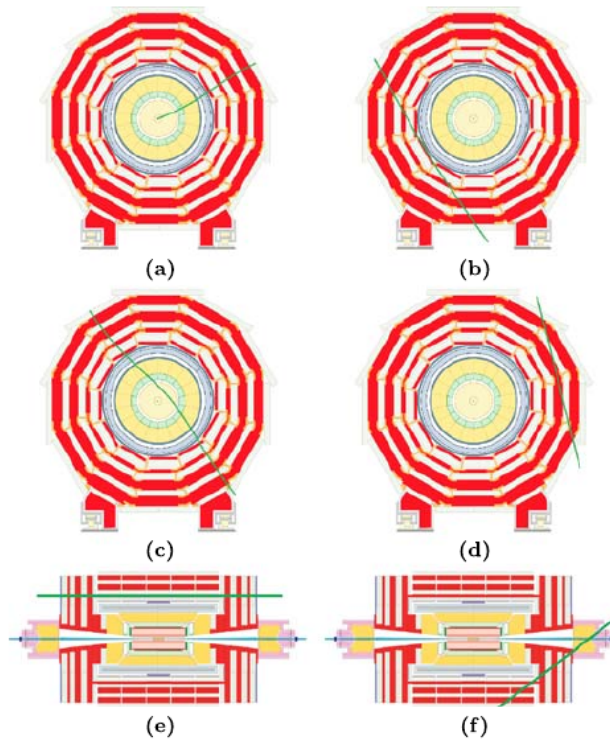


Figure 5.6: Illustration of the differences between proton-proton collision muons, cosmic and halo muons. (a) Muons from collision propagating from the center and moving outwards in a well defined pattern, (b) Cosmic muons penetrating the detector and leaving signals in opposite hemispheres of the muon system, (c) Cosmic muons leaving signals in the tracker and opposite hemispheres, (d) cosmic muons entering and leaving the detector without passing through the muon detector layers, (e) beam halo muons penetrating the detector and leaving signals in the endcaps and (f) Cosmic muons entering the detector through the endcap and leaving through the barrel and which can happen in a vice-versa manner.

A new stand-alone and global muon reconstruction software with the assumption that muons originate from outside the CMS detector and according to the properties of cosmic and halo muons has been optimised to reconstruct and identify both cosmic and halo muons which are used studies involving calibration and aligning the muon detectors.

### 5.1.5 Jet Reconstruction

Jets are experimental signatures of quarks and gluons produced in high energetic processes such as hard partons scattering in proton-proton collisions or gluon radiation processes. CMS reconstructs four types of jets which each combine individual contributions from sub-detectors to form inputs to a jet clustering algorithm. The four types of jets include Calorimeter jets, Jet-Plus-Track (JPT) jets, Particle-Flow (PF) jets and track jets. The clustering algorithm is the Anti- $k_T$  clustering algorithm with a size parameter of  $R = 0.5$ . Calorimeter jets are reconstructed using energy deposits in the combine ECAL and HCAL calorimeter cells called calorimeter towers. A calorimeter tower is a single or group of HCAL cells with their geometrically corresponding ECAL crystals. In order to suppress both noise and contributions from event pile-up (additional proton collisions within the same bunch crossing), thresholds are applied to both the individual cells when building the calorimeter towers as well as a transverse energy ( $E_T$ ) cut on the calorimeter tower energy. Typical  $E_T^{towers} > 0.3 - 0.7$  GeV is often used. Of particular importance to our analysis is the Particle Flow jets (PFJ). PFJ are reconstructed using the PF algorithm. The PF algorithm uses as input a list of reconstructed particles which include charge hadrons from tracks in central tracker, photons and neutral hadrons reconstructed from energy clusters in the HCAL and ECAL,

neutral particles as clusters separated from extrapolated position of tracks in calorimeters and electrons from tracks matched to clusters in the calorimeters. The PF algorithm exploits the high granularity in ECAL to precisely measure charge hadrons and photons inside jets, which makes up a larger portion of the jet energy. The quality of the jet is determined by variables making up the "Jet ID". For example, a high quality jet is required to have an electromagnetic energy fraction (EMF),  $EMF > 0.01$ , within the ECAL fiducial region  $|\eta| < 2.6$ ; the number of calorimeter cells containing more than 90% of jet energy must be  $n_{jet}^{90} > 1$ ; and the fraction of jet energy in the hottest Hybrid Photo Detector (HPD) unit of HCAL readout within a jet must be  $f_{HPD} > 0.98$ ; the charge hadron fraction  $CHF > 0.0$  if within  $|\eta| < 2.4$ , neutral hadron fraction  $NHF < 1.0$ , charge electromagnetic fraction  $CEF < 1.0$ , and neutral electromagnetic fraction  $NEF < 1.0$ . These requirements are used to remove fake jets arising from spurious energy deposition in a sub-detectors. Because the measured jet energy is usually different (usually unwanted energy) from the true corresponding particle jet energy due to miss-reconstruction, non-linear response of the calorimeters, electronic noise and additional energy contributions from PU, jet energy corrections during jet energy calibration (JEC) are applied to correct for this energy miss-match between the reconstructed measured jet energy and the true energy of the jet particle. This JEC to determine the jet absolute response is a source of systematic uncertainties in a given physics analysis.

### 5.1.6 Missing Transverse Energy Reconstruction

In CMS, quantities such as *transverse momentum* ( $p_T$ ), *transverse energy* ( $E_T$ ) and *transverse missing energy* ( $E_T^{\text{miss}}$  or MET) are used to distinguish a particle's quantities in the transverse plane( $x - y$  coordinate) from those along the longitudinal direction( $z$  coordinate) or beam line. In addition to these transverse quantities, cone-like structure with the cone radius is defined as

$$\Delta R = \sqrt{\Delta\eta^2 + \Delta\phi^2}$$

are used to measure the distance between two objects in the  $\eta - \phi$  plane. These cone-like structures are used for particle isolation and identification purposes.

A typical collider detector can only be nearly hermetic despite its nearly  $4\pi$  solid angle coverage as there is always room for passage of the colliding beams. As a result the use of the total energy balance constraint is not very useful since low  $p_T$  energetic interaction products moving in the forward direction can always escape detection. Thus, although these forward moving particles can carry significant longitudinal momentum (momentum along the direction of the beams), their transverse momentum (momentum transverse to the direction of the beam),  $p_T$  is always smaller than their total momentum. In the case of the CMS detector which has pseudo-rapidity  $|\eta| < 5.0$ , therefore only particles with  $|\eta| > 5.0$  can escape detection, as we can easily find that the  $p_T$  of any given particle in CMS detector given as  $p_T = E/\cosh \eta < E/\cos(5) < 0.013 \times E$ . Thus even if the particle carried the whole 7 TeV energy of a single proton beam, its  $p_T < 100$  GeV/c. Partons inside a protons which collide to produced moving particles typically have only a fraction of the energy of the colliding proton. Each fraction is determine by parton distribution function (PDF). PDF are rapidly falling functions, thus a typical momentum for forward moving particles in hard collisions on interests for physics goals of an experiment is significantly less than the full beam energy. As a result, the transverse momentum carried away by particles beyond the acceptance of a calorimeter is very small, thus the detector allows for a precise test of 2-D momentum conservation of the plane perpendicular to the direction of the beams. In the case of the CMS detector, this plane in the  $x - y$  plane. Thus the measurement in the calorimeter of a significant imbalance in the transverse momentum will indicate the production of a weakly interacting particle in the collision. Among SM particles, such an imbalance would indicate the presence of e neutrino or a muon which deposits a very small amount of energy in the calorimeters. However, the momentum of the muon can very precisely be measured using information from the tracker and muon chambers, and the calorimeter based missing transverse momentum can be measured and corrected for the muon's presence. Thus only the neutrino would truly escape detection, and its presence would be inferred from the remaining imbalance in the total transverse momentum as measured in the calorimeter and muon detectors. Other extensions of the SM, also predict the existence of other weakly interacting stable and quasi-stable particles, thus if an excess of events with a significant amount of transverse momentum imbalance is observed after accounting for all the SM processes, it would constitute a strong evidence

for new physics beyond the SM. In the case of the minimal GMSB, the gravitino ( $\tilde{G}$ ) would be the new physical particle. Thus the total transverse momentum imbalance or *missing transverse momentum* is an important variable to use in the search of new physics particles. On the other hand, poorly reconstructed objects, detector malfunctions, electronic noise and miss-measured transverse momentum can all lead to missing transverse energy thus mimicking the signal for new physics. Thus careful studies of the performance of the missing transverse energy variable in identifying neutrinos in the SM with high efficiency and accuracy is needed in order to depend on the use of it. The missing transverse momentum represented as the Missing transverse energy or MET ( $E_T^{\text{miss}}$ ) which is itself a scalar quantity defining the magnitude of the missing transverse momentum which has both direction ( $\phi_{E_T^{\text{miss}}}$ ) and magnitude  $E_T^{\text{miss}}$ . The missing transverse energy is defined as the magnitude of the negative transverse vector sum over all energy deposits in uncorrected, projective Calorimeter Towers produced in a given event:

$$E_T^{\text{miss}} = \left| - \sum_n (E_n \sin \theta_n \cos \theta_n \hat{\mathbf{i}} + E_n \sin \theta_n \sin \theta_n \hat{\mathbf{j}}) \right| = |\not{E}_T^x \hat{\mathbf{i}} + \not{E}_T^y \hat{\mathbf{j}}| \quad (5.2)$$

Where  $n$  is the sum over all calorimeter input objects including energy deposits in towers, reconstructed hits or generator -level particle energies. The  $E_T^{\text{miss}}$  values in physics processes of interest include processes with small  $E_T^{\text{miss}}$  such as the decay of  $W$  bosons and top in the SM to large  $E_T^{\text{miss}}$  as in the decay of SUSY particles. Thus in order to use small  $E_T^{\text{miss}}$  for searches, SM processes like QCD, JEC and low energy resolution must be well understood while to use large  $E_T^{\text{miss}}$  for searches, machine induced background processes and poor event reconstruction which processes with sources of large  $E_T^{\text{miss}}$  must equally be well understood.

## 5.2 Anomalous Signals

Neutrons and charged hadrons such as protons may by pass the PbWO<sub>4</sub> without scintillating and striking and thus directly ionizing the silicon of the APDs to produce anomalous signals. These kind of events produced large isolated energy deposits thus

are referred to as "punch through" events or "spikes". Because of the lack of scintillation, they appear much earlier (negative) in Ecal time and often populate the earlier time of the rechit time distribution. Their energy deposit ranges from a few GeV to ECAL saturation energy of  $\approx 1.7$  TeV. Since they do not electromagnetically shower in PbWO<sub>4</sub>, their electromagnetic energy shower shape is very isolated, meaning only one or two crystals may make up their energy cluster. Spikes may also have positive time and thus appear late or delayed in their arrival at ECAL which is seen in the tails of the rechit time distribution. Their late arrival time is due to the slow propagation of neutrons through the CMS detector. A lot of test beam, collision data and simulation study has been performed to study and analyse the characteristics and rejection of spikes as seen in here [40]. As a result, most of the results presented in this thesis are taken directly from [40] or redone for 2012 dataset which this analysis is based upon. It has been observed through studies using minimum bias data set( highly populated with neutrons and charged hadrons) at different center of mass energy, that the number of spikes increases with the proton collision rate as well as the charged tracks per event i.e there is a strong linear correlation between spike rate and the center of mass energy of pp collision. The reason for this is because more neutrons and charged hadrons with enough energy are produced which "punch through" the APD and produce hikes in the rechit energy profile as read from the APDs. It is understandable that spike production is most common in the barrel compared to the endcap. Thus with increases rate of proton collision and  $\sqrt{S} = 8$  TeV, it is imperative to have robust variables which can identify and reject spikes in the barrel in this analysis. The above studies show that variables defined using timing and EM energy deposits are reliable. Other variables using the timing pulse shape and EM shower profile can be used in addition to identify and rejects spikes with efficiency of 90 to 95%.

Rejection of spikes is done at online( CMS Level-1 trigger level) as well as offline and analysis level.

At online, the strip Fine-Grained Veto Bit(sFGVB) is set to 0 or 1 use to flagging an object as either a spike or a good event respectively. A detail of this can be found in [41]. For example if the sFGVB is set to 0 and the trigger tower(  $5 \times 5$  crystals) transverse energy is below 12 GeV, the energy deposition is considered spike-like and the corresponding tower will not contribute to CMS triggering of that event. The sFGVB

was implemented in 2011 data taking process and was measured to reject over 95% of spikes with transverse energy greater than 8 GeV (12 GeV) in 2011(2012). The figure **Figure of sFGVB** shows the difference between an good EM-cluster and a spike-like cluster at sFGVB level.

At Offline, variables making using of the single(at times double) channel(crystal) energy deposit and early arrival time of spikes are defined. In figure **Figure of Swiss X and Rechit Time**, we show the difference between spikes and normal events energy clusters explaining the variables used to identify spikes in the offline. The topological variable constructed as  $1 - \frac{E_4}{E_1}$  also known as "Swiss-cross" where  $E_1$  is the energy deposit of the central( highest energy) crystals and  $E_4$  is the sum of the energy of the neighbouring crystals in an  $\eta - \phi$  plane is used for identifying isolated spikes. The figure **Figure of Spike energy topology and Distribution of SwissX** shows the construction of the swiss-cross variable as well its distribution in data and simulation events. The peak at 1.0 in data of the distribution is due to the presence of spikes. A cut in Swiss-cross  $> 0.95$  rejects more than 99% of isolated spikes with transverse energy greater than 10 GeV with very little impact on the efficiency of selecting electromagnetic EM showers. Other topological energy deposit variables such as  $1 - \frac{E_2}{E_6}$  and  $1 - \frac{E_2}{E_9}$  where  $E_2$  is the sum of the energy of two crystals sharing the energy deposited and  $E_6(E_9)$  is the sum of the neighbouring 6(pairs-of)(9) crystals in the  $\eta - \phi$  plane. The  $1 - \frac{E_2}{E_6}$  variable is used for the identification of isolated spikes whose energy deposit spread in two adjacent crystals while the  $1 - \frac{E_2}{E_9}$  is used to identify non-isolated spikes or spikes which are found embedded in a normal Ecal supercluster.

The figure **Put figure of di-spike and non-Isolated spike construction and distribution** A cut on  $1 - \frac{E_2}{E_6}$  ( $1 - \frac{E_2}{E_9}$ ) greater than 0.95 ( 0.98 for tight) gives an efficiency close to 95% for events with transverse energy greater than 10 GeV for rejecting spikes with very little effect on normal EM shower reconstruction.

Another very important variable used for rejecting spikes with greater efficiency is rechit ECAL timing. Spikes and EM energy deposits show very distinct signal pulse shapes. Since spikes do not in the PbWO<sub>4</sub>, when the pulse shape is fitted to extract the timing of a signal, the spikes appear "early" due to faster rise time of the spike pulse. The figure **Fig of spike pulse shape and rechit time distribution for data and simulation** shows the comparison between the pulse shape for a spike candidate pulse and

and true PbWO<sub>4</sub> scintillated event. The adjacent plots shows the distribution of the rechit time for simulation( where there are no anomalous signals) and collision data where anomalous signals have a significant contribution to out-of-time signals.A cut on timing of  $\pm 3$  ns gives greater than 90% efficiency for rejecting spikes however, in this thesis, we do not employ this timing cut as we are actually searching for delayed objects whose timing can be beyond the  $\pm 3$  ns window.

However, it is worth noting that, these anomalous signals if not rejected will lead to a biasing in the reconstruction of other physics variables such as missing transverse energy(  $E_T^{\text{miss}}$ ) as well as being miss-identified as a possible signal for delayed photons. Infact the spike rate per bunch crossing as observed in [41] was approximately  $1 \times 10^{-3}$  in collisions bunch crossings while in non-collision bunch crossing is of the order of  $2 \times 10^{-6}$  in non-collision bunch crossings. This spike rate from non-collision rate is obtained from cosmic muon data recorded during June-August 2009 while the spike rate for collision is obtained from Minimum biased( Soft proton-proton) collision events data. Thus, in this thesis, we have restricted ourselves to using only the energy topological variables discussed in previous paragraphs to identify and reject anomalous signals.

### 5.3 Using Timing for Event Cleaning

Energy RecHits and clusters used in the reconstruction of higher level objects are required in addition to cluster cleaning conditions, to pass certain selection criteria using transverse energy and ECAL timing. For the case of photon, electron, PF jets and  $E_T^{\text{miss}}$  reconstruction, the basic and super-clusters are required to be seeded by seed crystals whose time is within approximately 3 ns in the barrel and 7 ns in the end-caps. These are called *in-time* RecHits. These RecHits are the standard RecHits used in the reconstruction for most physics objects used in physics where timing is not an important variable. The choice for using timing, is because, timing combined with other topological variables is an excellent variable to identifying and rejecting readout electronic crystals with large noise, poorly reconstructed RecHits, RecHits from anomalous signals, RecHits from machine induced events and cosmic muons as well as improved timing calibration. However, for physics analysis like our case of searching for long-lived particles, this cleaning procedure is not useful. As rejecting RecHits with time more

than 3 ns also known as *Out-Of-Time* RecHits will remove super clusters from potentially delayed electrons and photons which defines the signal for new physics. Thus in this analysis, we combined all classes of RecHits, and do not reject RecHits with large reconstructed time except if the time is well beyond expected time for physics objects produced in proton-proton collisions within the required Bunch Crossing time spacing of 25 ns or 50 ns. The electromagnetic objects in this analysis are reconstructed from the combined sample of time cleaned and unclean RecHits. All other RecHit cleaning is applied except that which involves RecHit timing information.

## Chapter 6

# Search Analysis for Long-Lived Particles

### 6.1 Analysis Strategy

Our analysis performs a search for delayed isolated photons produced with large transverse momentum. It is possible, at least in theory, that events with such photons are produced from the decay of a lightest neutralino,  $\tilde{\chi}_1^0$ , produced from the cascade decay of gluinos and squarks or other massive supersymmetry particles or an entirely new particle. Within the context of supersymmetry, in addition to the delayed high  $p_T$ , isolated photon, an associated gravitino,  $\tilde{G}$ , also produced in neutralino decay, is very weakly interacting with detector material. As a result, its presence is indirectly inferred using missing transverse momentum whose magnitude is  $E_T^{\text{miss}}$ , as being part of the possibly observed event. Observing such an event at the LHC, using the CMS detector, would represent a clear signal for new physics as such events are not expected to be produced from standard model interactions. However, from an experimental point of view, using timing measurements from ECAL sub-detector in making such observations must be handled with ultimate care as there could be many different sources of isolated, high  $p_T$  and even delayed photons due to timing miss-measurements and poor event reconstruction. A few of these sources which have been identified are high  $p_T$ , isolated and delayed photons from timing miss measurements and miss-identification, photons produced from cosmic and other proton beam related activities like *beam halo* muons

producing photons through the process of *bremstrahlung* in the ECAL, and obviously detector effects like high  $p_T$  neutrons by-passing the PbWO<sub>4</sub> crystals and hitting directly the photo-detectors, APD and VPT, mimicking the behavior of isolated, delayed and high  $p_T$  photons. The latter kind of photons are called *spikes*. These photons can be identified as isolated, having high  $p_T$  with ECAL time measurements showing that they arrive early as well as late compared to "normal" photons produced at the nominal proton-proton interaction region whose average arrival time at ECAL is 0 ns. These different sources of background makes it challenging to distinguish a possible signal photon from the separate background photons. Thus, estimating the background contributions to possible signal events sample requires using true proton-proton collision events rather than simulated events which do not accurately mimic proper timing measurements for this kind of background events as is normally the case in most physics analysis. Nevertheless, as it is with most hadron collider physics analysis, exploring the use of the number of jets in the event selection can most often reduce dramatically the background contamination to possible signal sample. It is not different with this analysis, where we have employed *jet multiplicity* both as a possible signal definition requirement for the production of high  $p_T$  isolated and delayed photons but also as a detector variable for reducing and at times discriminating background from possible signal events. Our motivation is to perform a model independent search while at the same time guided by SUSY models such as SPS8 benchmark model and GGM, where the production of a high  $p_T$  isolated, delayed photon in association with a number of jets and large  $E_T^{\text{miss}}$  constitutes a typical new physics event which could be produced at the LHC. Thus, our simulated events from SPS8 or GGM model, serves both as a guiding model for understanding a possibly observed event with a new physics signature and also for setting limits on some fundamental parameters with respect to these models in case we observed no significant excess over SM prediction.

A typical signal event considered in this analysis for the existence of a neutral massive long-lived particle decaying into a photon, is the detection of a late photon arriving at crystals in the ECAL sub-detector of CMS associated with jets and large  $E_T^{\text{miss}}$ . In the SPS8 model with R-parity conservation (RPC), the neutralino ( $\tilde{\chi}_1^0$ ) is the long-lived neutral particle and decays into a high  $p_T$  isolated and late arrival photon in association with at least two jets and a weakly interacting gravitino ( $\tilde{G}$ ) in a signal event. The jet

multiplicity is from jets produced in the cascade decay of possibly higher mass SUSY particles into the neutralino. The gravitino ( $\tilde{G}$ ) presence is inferred using the transverse momentum imbalance whose magnitude is  $E_T^{\text{miss}}$ . Using this signal events signature, we divide our data samples into possible signal regions (SR) and control regions (CR) and use these CRs for estimating background contributions from beam related activities, miss reconstructed standard model processes and detector effects. We also use events with negative photon time as a control sample for studying veto methods for rejecting and estimating background contribution from non-collision events.

### 6.1.1 Signal and Background Modelling

We begin generating signal events according to the SPS8 GMSB model by producing Supersymmetry Les Houches Accord (SLHA) files using the SUSY software package *ISASUSY*,[54]. *ISASUSY* contains the program *ISAJET* which is used to determine SUSY mass spectrum and decay parameters according to a given SUSY model. The input to *ISAJET* are the fundamental parameters  $\{\Lambda, M_{\text{mess}}, N_5, \tan(\beta), sgn(\mu), C_{\text{grav}}\}$ . According to the SPS8 benchmark model, we have chosen,  $sgn(\mu) = 1$ ,  $\tan(\beta) = 15$ ,  $N_5 = 1$  and  $M_{\text{mess}} = 2\Lambda$  allowing  $C_{\text{grav}}$  and  $\Lambda$  as the free parameters to study the different life time and mass of the neutralino. The output of *ISAJET* is a SLHA file that has the SUSY mass spectrum and decay rates and branching ratios according to the SPS8 model. *HDECAY* is used as the tool for simulating the decay of SUSY particles including the neutralino to gravitino. The neutralino can also decay into  $Z$  bosons, *Higgs* and  $e^+e^-$  with a gravitino but with about 83 to 94% of its decay into  $\gamma + \tilde{G}$ . 97 to 99% of all the events contain at least a single photon. These SLHA files containing information about the SUSY mass spectrum and decay rates is fed into a *PYTHIA6*, [55], proton-proton collision event generation interface of the CMS software (CMSSW) event generation and reconstruction software. In our case **CMSSW\_5\_3\_2\_patch7** version of the software is used. The center of mass energy for these proton-proton collisions  $\sqrt{8}$  TeV for generating these SUSY events. Production, interaction and decay of these events in the CMS detector is simulated using the GEANT4 package,[56]. Since a possible background process to our analysis is miss-measurement of the timing of photons produced by Standard Model processes like multi-jets and  $\gamma+$  jets processes produced

from strong interactions described by quantum chromodynamics (QCD), we also generate and simulated at leading order cross-sections using PYTHIA 6 and GEANT4 a small sample of these events for determining an estimate of time miss-measurement of our signal Monte carlo events. Digitization and event reconstruction in terms of its constituent objects like jets, photons, muons and electrons, after production and decay in the full CMS detector is later again performed during analysis using the CMSSW software.

### Simulated Signal Events

Our signature for signal events within the SPS8 benchmark model are events containing the following:

- at least one energetic delayed photon,
- a number of high transverse momentum jets,
- large missing transverse momentum,

### Simulated Background Events

QCD multi-jets and  $\gamma +$  jet(s) events with high  $p_T$  photons with miss reconstructed photon time is a possible background source. In order to understand and calibrate for any such miss measurements, we use simulated or Monte Carlo  $\gamma +$  jet(s) events to perform such a study and for sanity check with MC time measurements. Events with  $W$  and  $Z$  decay and  $t\bar{t}$  with large missing transverse momentum, jets and miss-reconstructed photons could also possibly contribute to background, however, these processes produced mostly in-time events with rarely any photons with large late times. Thus, we consider this background to be negligible and do not perform any MC studies for them.

#### 6.1.2 Datasets

The dataset used in this analysis was produced during proton-proton collisions of LHC Run 1 in 2012 with the center of mass energy,  $\sqrt{S} = 8$  TeV. The CMS detector recorded data equivalent to total integrated luminosity of  $19.1 \text{ fb}^{-1}$ .

## Data

These datasets contain events with at least a single photon triggered. Only datasets for which the luminosity-sections are certified as GOOD are used. The *jason* file with this good luminosity sections is **Cert\_8TeV\_PromptReco\_Collisions12\_JASON.txt**. Table 6.1 shows the dataset and their corresponding integrated luminosity as used in this analysis.

| Dataset   | Recorded Luminosity [fb <sup>-1</sup> ] |
|---|---|
| /Run2012B/SinglePhoton/EXODisplacedPhoton-PromptSkim-v3 | 5.1                                     |
| /Run2012C/SinglePhoton/EXODisplacedPhoton-PromptSkim-v3 | 6.9                                     |
| /Run2012D/SinglePhoton/EXODisplacedPhoton-PromptSkim-v3 | 7.1                                     |
|   |   |
| /SingleElectron/Run2012A-22Jan2013-v1/AOD               | 5.2                                     |
| /DoubleElectron/Run2012C-22Jan2013-v1/AOD               | 4.8                                     |

Table 6.1: Dataset and corresponding integrated luminosity totaling 19.1 fb<sup>-1</sup> used in this analysis

## Background and Signal Monte Carlo

The Monte Carlo (MC) samples are produced taking into account the Summer 2012 prescriptions carrying information on the calibration and alignment conditions of the CMS detector with pile up (PU) conditions at 8 TeV. We generate QCD events at leading order (LO) cross-section ( $\sigma$ ) and normalized to the 19.1 fb<sup>-1</sup> integrated luminosity. The official CMS MC production events for signal GMSB contains 50000 events. Performing a quick sanity check by measuring and comparing the generated neutralino lifetime ( $c\tau$ ) to its lifetime from SLHA files produced with ISAJET, we observed that most of the generated neutralino events had their lifetimes reduced by a factor of about 3. In order to extend our study to longer neutralino lifetimes, we produced private GMSB samples, generated and simulated with the same conditions as the official CMS samples but having correctly produced and measured neutralino lifetimes thus extending the GMSB sample to include neutralinos with long lifetimes. These combined GMSB MC samples from private and official simulations allow our search analysis to scan neutralino ( $\tilde{\chi}_1^0$ ) lifetimes,  $c\tau$  from 250 mm to 12000 mm for each  $\Lambda_m$  point with  $\Lambda_m$  ranging from

100 TeV to 180 TeV as shown in table 6.2. Table 6.3 also show the  $p_T$  range for the processed QCD samples.

| $\Lambda$ [TeV] | $c\tau$ (mm) | $\sigma_{LO}$ (pb) | Number of Events | Branching Ratio |
|-----------------|--------------|--------------------|------------------|-----------------|
| 100             | 250-12,000   | 0.368              | 50,000           | 0.9444          |
| 120             | 250-12,000   | 0.133              | 50,000           | 0.9042          |
| 140             | 250-12,000   | 0.0574             | 50,000           | 0.8711          |
| 160             | 250-12,000   | 0.0277             | 50,000           | 0.8464          |
| 180             | 250-12,000   | 0.0145             | 50,000           | 0.8282          |
| 220             | 250-12,000   | 0.0044             | 50,000           | 0.8282          |
| 260             | 250-12,000   | 0.0015             | 50,000           | 0.8282          |
| 300             | 250-12,000   | 0.0008             | 50,000           | 0.8282          |

Table 6.2: The signal GMSB SPS8 MC samples for difference  $\Lambda$  and Branching Ratios used in this analysis

| $\hat{p}_T$ | $\sigma_{LO}$ (pb) | Number of Events |
|-------------|--------------------|------------------|
| 50 ~ 80     | 3322.3             | 1995062          |
| 80 ~ 120    | 558.3              | 1992627          |
| 120 ~ 170   | 108.0              | 2000043          |
| 170 ~ 300   | 30.1               | 2000069          |
| 300 ~ 470   | 2.1                | 2000130          |
| 470 ~ 800   | 0.212              | 1975231          |

Table 6.3: The  $\gamma+$  jets samples used in this analysis

## 6.2 Event Selection

The major background events to this analysis are events which are not produced from the nominal proton-proton collisions. These events can be separated into three major categories; *Halo* muons, *Spikes* and *Cosmic muons*. In addition to these events, there are also QCD events which mimic the  $\tilde{\chi}_1^0 \rightarrow \gamma + \tilde{G}$  decay due to photon miss reconstruction and measurement of fake  $E_T^{\text{miss}}$ . Contribution from  $\gamma+$  jets events can also be regarded as background events especially in cases there is a real isolated photon and a fake  $E_T^{\text{miss}}$

due to miss identification of jets as photons. Even though the event topology for most  $\gamma +$  jets events is quite different from that of GMSB signal events.

Another possible background contribution, in addition to QCD multi-jets events, events from ElectroWeak (EWK) decay including  $W \rightarrow e + \nu$  and  $t\bar{t}$  decays, where the top ( $t$ ) decays to a  $b$  quark and a  $W$  100% of the time. The electron is miss reconstructed and thus miss identified as a photon and real  $E_T^{\text{miss}}$  is measured due to the presence of the neutrinos ( $\nu$ ). We can easily reduce this background by requiring high jet multiplicity events since most of these EWK and QCD events contains low number of high  $p_T$  jets in them. In order to maintain a high background rejection and good signal selection efficiency, we select events with at least two jets. This helps to reduce EWK and other low jet multiplicity backgrounds contributions prior to additional photon quality selections based on the isolation and electromagnetic shower profile. Using ECAL time measurements, our signal acceptance regions are events with photons whose time is between  $3 < t_\gamma < 13$  ns. This cuts allows us to avoid events with high spike contamination.

In addition to collision backgrounds mentioned in the previous section, non-collision originated background events like Cosmic muons, beam halo muons and ECAL spikes contain photons with large reconstructed time and large  $E_T^{\text{miss}}$  measurements.  $E_T^{\text{miss}}$  measurements includes  $p_T$  from all reconstructed particles in an event with the assumption that these are events from the nominal proton-proton collision. However, not all events are produced from collision. Cosmic muons, beam halo muons, spikes, ECAL and HCAL noise can all contribute to the total sum of the measurable event  $p_T$  imbalance. In some events these provide the major contributions to  $E_T^{\text{miss}}$  calculations. We begin by selecting events with at least a good vertex, quality jets, satisfying ECAL spike cleaning, DT time cosmic muon cleaning and CSC tight halo-muon cleaning criteria. This event selection criteria is very useful in reducing contributions from non-collision events.

A typical diagram showing both non-collision and collision backgrounds in neutralino production and decay from LHC proton-proton collision within the CMS detector is shown in figure 6.1. A typical GMSB decay of the neutralino is also shown in this

diagram indicating the two different sources for delayed photon produced from this decay.

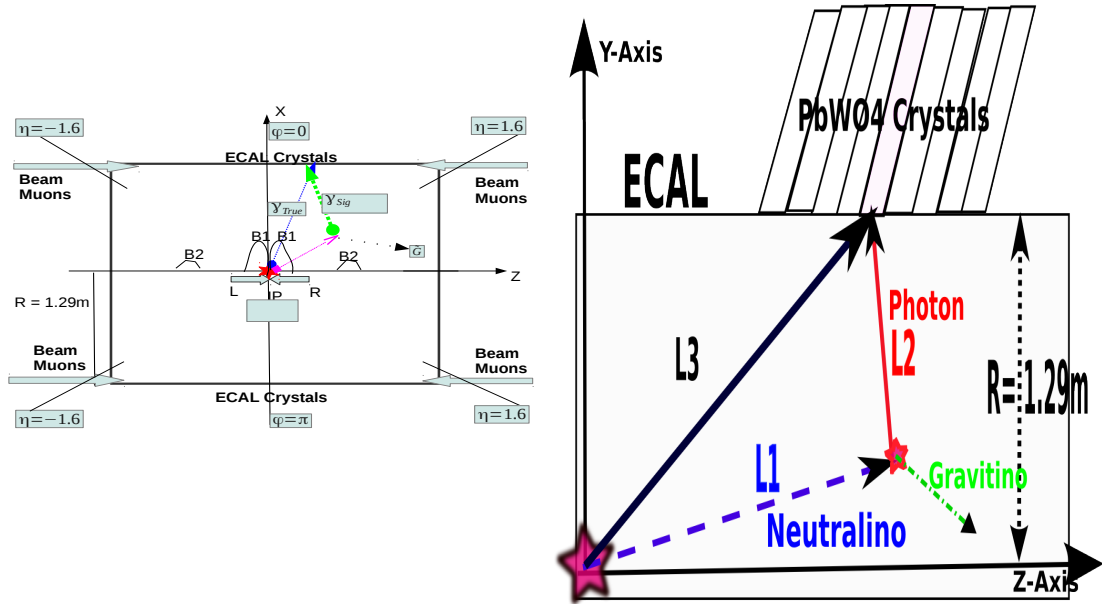


Figure 6.1: Schematic diagram showing  $\tilde{\chi}_1^0 \rightarrow \gamma + \tilde{G}$  decay topology within the ECAL volume of the CMS detector. Proton beams are also shown showing the possible production of collision and non-collision delayed photons

### 6.2.1 Trigger

Our pre-event selection begins online by selecting only events which pass our online higher level trigger (HLT). The HLT trigger used for our  $\sqrt{S} = 8$  TeV proton-proton collision analysis is the `HLT_DisplacedPhoton65_CaloIdVL_Isol_PFMET25` seeded by `HLT_L1SingleEG12` level 1 trigger. It was developed primarily for the study of displaced photons. To avoid bias in event selection towards any particular model, this trigger only requires that an accepted event contains an isolated photon with a  $p_T$  threshold of 65 GeV/c and  $E_T^{\text{miss}}$  above 25 GeV. The photon shower shape must also satisfy  $0.1 < 0.S_{\text{Minor}} < 0.4$ . We study our trigger efficiency and turn-on curve (efficiency becomes close to 100%) for selecting events with delayed photon candidates. In order to avoid any correlation between the photon and  $E_T^{\text{miss}}$  variables, we study efficiency for each variable separately using another trigger `HLT_Photon50_CaloIdVL_Isol`.

The selected photon candidates for studying this HLT photon efficiency must pass our offline photon selection candidate criteria shown in table 6.4. The HLT photon selection efficiency for  $p_T$  is defined as the fraction of offline reconstructed photons to those triggered by *HLT\_IsoPhoton50* photon candidates within  $\Delta R < 0.5$ . Similarly, the  $E_T^{\text{miss}}$  HLT efficiency is defined as the fraction of events containing at least a jet and  $E_T^{\text{miss}}$  more than the HLT required  $E_T^{\text{miss}}$  of 25 GeV. The results of the trigger efficiency measurements are shown in figure 6.2 against photon  $p_T$  and  $E_T^{\text{miss}}$ . These efficiency studies are made using the *HLT\_Photon50\_CaloIdVL\_IsoL* trigger which has no  $E_T^{\text{miss}}$  and jet multiplicity requirement as the denominator and the *HLT\_DisplacedPhoton65\_CaloIdVL\_IsoL\_PFMET25* as numerator. A *SinglePhoton* dataset is used to verify these efficiency while and GMSB and  $\gamma +$  jets samples is used to derive any correction factors between data and MC events.

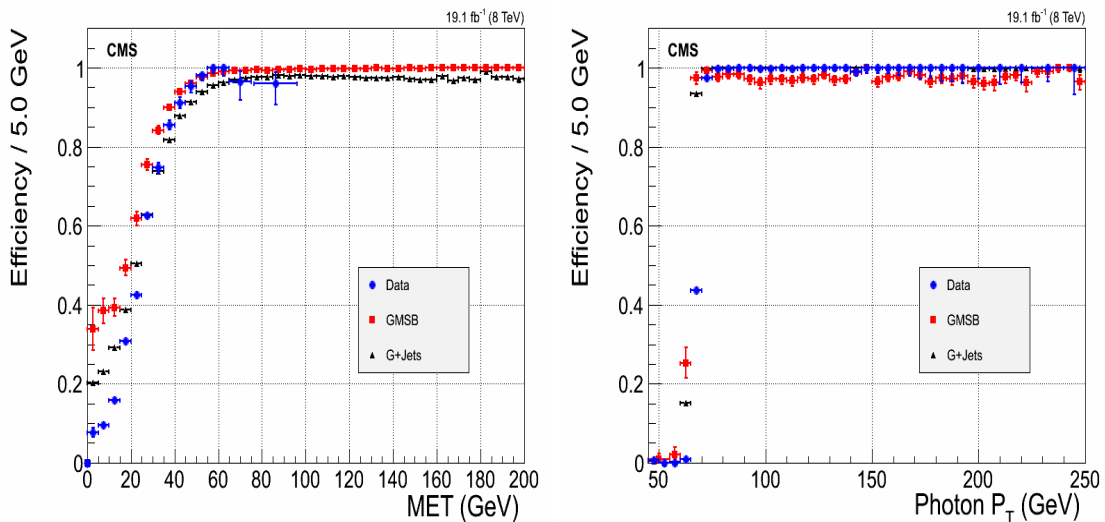


Figure 6.2: Trigger efficiency turn-on curves for photon  $p_T$  and  $E_T^{\text{miss}} > 25$  GeV (left) and for  $E_T^{\text{miss}}$  with photon  $p_T > 80$  GeV/c (right). The  $\gamma +$  jets samples require photon  $p_T > 170$  GeV/c for selecting events with true  $E_T^{\text{miss}}$ .

### 6.2.2 Offline Selection

Our offline event selection requires candidate events in addition to passing our HLT trigger, contain at least a single photon, a jet and  $E_T^{\text{miss}}$ . The photon object collection used in our analysis is an extended collection of standard CMS Egamma photon

objects collections to include events classified as “*out-of-time*”. This classification was performed during the official CMS supercluster reconstruction process. This enlarged photon sample include events like spikes, ECAL noise, photons from beam halo and cosmic muons and detector malfunctions. It is also entirely possible that this collection also contains true candidate delayed photons which is our signal events. The selected photons are required to pass the photon selections criteria in table 6.4.

| <b>Photon Identification and Selection Criteria</b>                 |  |
|---|--|
| <b>Criteria</b>   | <b>Requirement</b>                       |
| Event leading photon must have $p_T(\gamma^1)$                      | $> 80 \text{ GeV}$                       |
| Other photons in event must have $p_T(\gamma^{>1})$                 | $> 45 \text{ GeV}$                       |
| $ \eta_\gamma $ , (Barrel Only),                                    | $< 3.0 (< 1.5)$                          |
| $S_{\text{minor}}$  | $0.12 \leq S_{\text{Minor}} \leq 0.38$   |
| $\mathbf{H}/\mathbf{E}$   | $< 0.05$                                 |
| $\Delta R(\gamma, \text{track})$                                    | $> 0.6$                                  |
| HCAL Iso  | $< 4.0$                                  |
| ECAL Iso  | $< 4.5$                                  |
| Track Iso   | $< 0.2$                                  |
| Photon Isolation cone size $\Delta R(\gamma, \text{otherparticle})$ | $< 0.4$                                  |
| Topological Spike cuts  | $1 - E_6/E_2 < 0.98, 1 - E_4/E_1 < 0.98$ |

Table 6.4: The photon identification and selection criteria used in this analysis

The presence of jets as associated particles from gluino cascade decay and the gravitino ( $\tilde{G}$ ) from neutralino decay,  $\tilde{\chi}_1^0 \rightarrow \gamma + \tilde{G}$  requires jet identification and  $E_T^{\text{miss}}$  or  $\cancel{E}_T$  selection criteria as well. Our jet and  $E_T^{\text{miss}}$  or  $\cancel{E}_T$  selection criteria is based on the particle-flow (PF) algorithm. Additional  $\cancel{E}_T > 65 \text{ GeV}$  due to the flatness of the HLT trigger efficiency against  $E_T^{\text{miss}}$  (see figure 6.2). Table 6.5 show a summary the jet identification and selection criteria with the threshold requirements used in this analysis.

### Jet PF identification selection criteria

| Criteria  | Requirement        |
|---|--------------------|
| Jet $p_T$   | $> 35 \text{ GeV}$ |
| Number of Jet constituents  | $> 1$              |
| Charge EM energy fraction (CEF)   | $> 0.99$           |
| Neutral Hadron energy fraction (NHF)  | $< 0.99$           |
| Neutral EM energy fraction (NEF)  | $< 0.99$           |
| If $ \eta $ of jet is $> 2.4$ , Charge Hadron energy fraction (CHF)   | $> 0$              |
| If $ \eta $ of jet is $> 2.4$ , Charge multiplicity (NCH)   | $> 0$              |
| $\Delta R(\gamma, \text{jet}) = \sqrt{(\phi_\gamma - \phi_{\text{jet}})^2 + (\eta_\gamma - \eta_{\text{jet}})^2}$ | $> 0.3$            |

Table 6.5: The Jet ID selection used in this analysis

### $E_T^{\text{miss}}$ Corrections

During the official CMS electromagnetic supercluster reconstruction, timing cuts of  $|t_{RECO}| > 3.0 \text{ ns}$  in EB is used for cleaning “out-of-time” events. As a result, the  $p_T$  contribution from out-of-time photon events is not included in the calculation of  $E_T^{\text{miss}}$  or  $\cancel{E}_T$ . This introduces a difference in the calculation of  $\cancel{E}_T$  for “in-time” events ( $|t_\gamma| < 3.0 \text{ ns}$ ) and “out-of-time” events ( $|t_\gamma| > 3.0 \text{ ns}$ ). Since the out-of-time photon  $E_T$  is not included in the sum total transverse momentum of an event to derived the total transverse momentum imbalance, we correct for this, by adding the out-of-time photon  $E_T$  to the PF-MET measured during CMS  $\cancel{E}_T$  reconstruction. We defined an additional variable,  $\cancel{E}_T^\gamma$ , accounting for this correction and use this variable in our event selection criteria.

1.  $\cancel{E}_T$ : PF-MET,  $\cancel{E}_T$  from CMS standard  $E_T^{\text{miss}}$  measurements.
2.  $\cancel{E}_T^\gamma$ : PF-MET with photon  $E_T$  added i.e  $\cancel{E}_T^\gamma = \cancel{E}_T + E_T$  of the out-of-time photon.

Our signal event selection criteria is defined as events with  $\geq 1 \gamma + \geq 2 \text{ jets} + \cancel{E}_T^\gamma > 60 \text{ GeV} + \cancel{E}_T > 60 \text{ GeV}$

We use a control sample to perform a closure test of our background estimation procedure. The selection criteria is events with  $\geq 1 \gamma + \leq 1 \text{ jet} + \cancel{E}_T > 60 \text{ GeV} + \cancel{E}_T^\gamma > 60 \text{ GeV}$

### 6.2.3 ECAL Time

The photon arrival time at ECAL is our main observable for distinguishing background from signal. However, the presence of spikes, noisy crystals and pile-up events, require measuring the photon time with methods which are robust to timing bias from such events. There are different ways to measure the photon time using ECAL. The reference time is the time measured from a relativistic electromagnetic object like a photon produced from nominal proton-proton collisions arriving at ECAL in an average time of zero. The photon time is measured using either of the following methods:

- *Seed Time*: Time from the highest energy crystal, which is not a spike, of the photon supercluster.
- *Cluster Time*: Error weighted average time of all the crystals in the seed basic-cluster of the photon supercluster.

Timing reconstruction as described in chapter 4 is the extraction of time from the pulse shape through a fitting method. The  $\chi^2$  obtained from the fit determines how well the time is reconstructed. One way of rejecting fake photons which are either jets miss-identified as photons or spikes is to use the fitted  $\chi^2$ . Studies performed have shown that a  $\chi^2 < 4$  cut improves the ECAL timing resolution by rejecting spikes and anomalous photon events as possible. Figure 6.3 shows a comparison between the pulse shape profile of a spike and that of a good event.

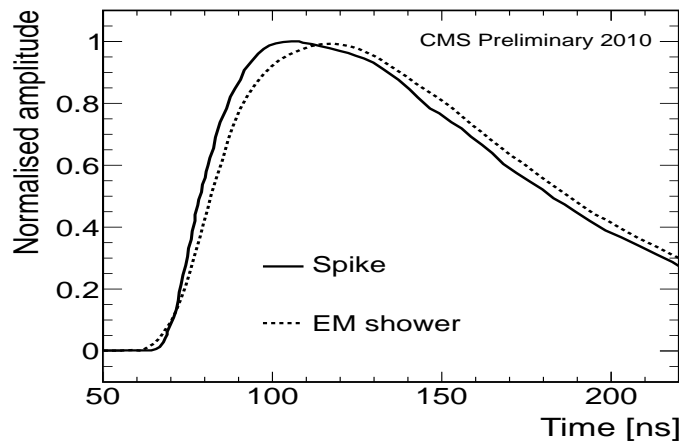


Figure 6.3: Pulse shape profile showing a spike (solid line) and a real photon (dashed line) from data.

In this thesis, we measure time using the seed crystal time approach. Our choice of seed time is based on a number of independent timing analysis performed comparing the timing resolution obtained from cluster time to the seed time. We observed the cluster timing method to be very biased towards the time of an isolated spike especially when the spike is embedded in a photon object. The timing resolution especially for large timing events is much better compared to the cluster time measurement method which is an essential region when searching for new long-lived particles. Figure 6.4 shows the timing measurements of photons using either seed time or cluster time. The seed time show an approximate timing resolution of 400 ps compared to 450 ps with a broad timing tail from using the error weighted average cluster time. The cluster time method is also computational time and resource consuming.

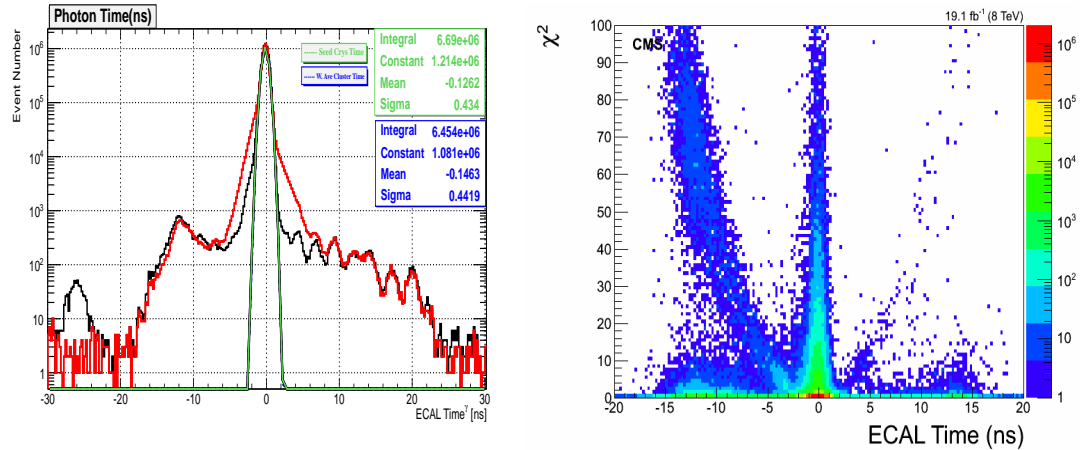


Figure 6.4: Timing distribution of photons showing timing measurements using seed crystal (black) and using Weighted Average basic cluster time (blue). Resolution ( $\sigma$ ) from seed time is better compared to that for cluster time which is computationally intensive. Together with the  $\chi^2$ , the seed time performs better in identifying anomalous timing objects.

Monte Carlo simulation of ECAL timing is challenging as the time of anomalous events such as spikes and noisy crystal channel present during data taking aren't well simulated. To account for MC and data timing measurement differences, We use QCD simulated  $\gamma + jets$  events and select events containing only one or two jets and study the

distribution of the difference between the generated time ( $T_{GEN}$ ) and the reconstructed MC event time ( $T_{RECO}$ ) in a timing window of [-2, 2] ns. Comparing this difference to data, the difference in the mean time between the data and MC  $\gamma +$  jet sample is used to smear the reconstructed time of the MC samples to be comparable to true reconstructed time in data. A difference of about 125 ps is observed between the timing from data and MC. Timing from the smeared MC sample show a close agreement with data. Figure 6.5 show this comparison before and after timing calibration (smearing adjustment) is applied on the MC samples.

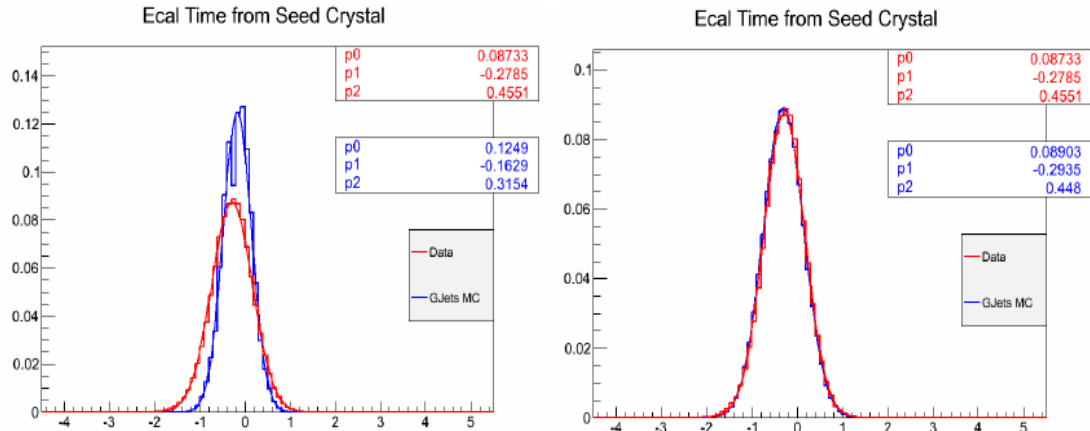


Figure 6.5: Timing distribution of photons showing timing of data and MC  $\gamma +$  jets (blue) samples and data (red) before (left) and after (right) timing Calibration is applied to MC.

It is worth noting that the difference of 125 ps between  $T_{RECO}^{MC}$  and  $T_{RECO}^{DATA}$  compared to 500 ps ECAL timing resolution is not enough to influence event selection, however event distribution in the tails remains a major concern.

The ECAL timing distribution for photons with  $pt > 50$  GeV in the ECAL (barrel and endcap inclusive i.e  $|\eta_\gamma| < 3.0$ ) show timing distributions (see figure 6.6)

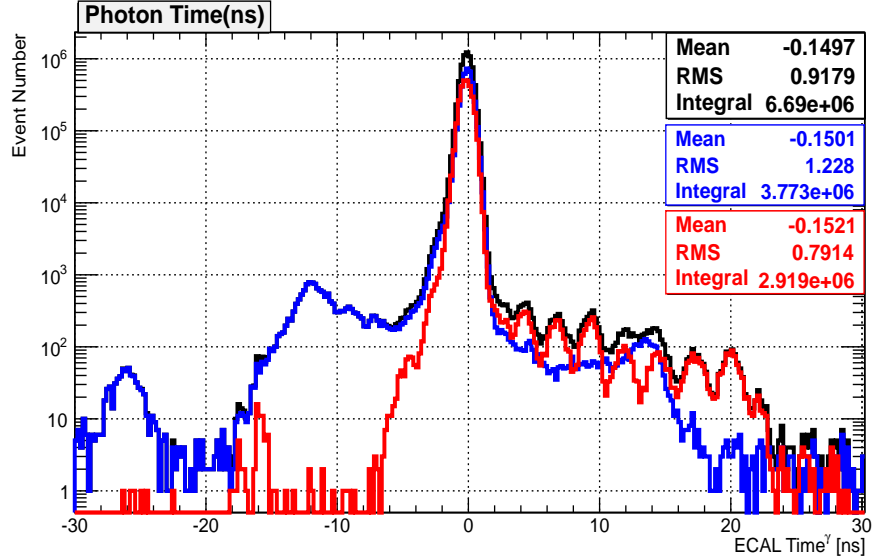


Figure 6.6: ECAL timing distribution of photons in barrel (EB), endcap (EE) and all of ECAL (ALL ECAL) with  $p_T > 50$  GeV from data. A 2.5 ns delay timing structure is observed in endcap subdetector.

with a clear 2.5 ns discrete pattern with most of these photons arriving in the endcap,  $1.47 < \eta < 3.0$  compared to the barrel,  $|\eta| < 1.47$ . These are photons produced from collisions of *Ghost* and *Satellite* bunches with either the main proton collision bunch or *Ghost/Satellite*. They contribute an irreducible amount to the photon time distribution which is very challenging to reject or estimate quantitatively. A rough estimate can be obtained by looking at ratio of the proton population in the filling profile of the LHC RF cavities as mentioned in section 3.1.5 of chapter 3 which gives a factor  $10^{-5}$  compared to contributions from the main proton-proton bunch collision. It is observed that contribution from ghost bunches is in the endcap crystals, since very few these photons are produced with enough  $p_T$  compared to those from main proton bunch collisions. And even if they do, the ratio of photons from these secondary proton collision to that of the main proton-proton collision is of the order of  $10^{-5}$  at most. As a result of this, we do not use the endcap in this analysis in addition to the fact that timing resolution in the endcap is relatively poor compared to the barrel. We check and validate this factor  $10^{-5}$  using events with  $Z \rightarrow e^+e^-$  since  $Z$  events do not require high  $p_T$  during production and must should capture the 2.5 ns timing pattern if present from

ghost/satellite collisions. We study electron candidates with time within [-2.0, 2.0] ns window. We use this in our background estimation method testing as will be discussed in future sections.

### Delayed Photon Source

With a well time calibrated ECAL and good MC to data time agreement, we can study the source of delayed photons from neutralino decay in ECAL using its decay kinematics. There are two possible sources for delayed photon from neutralino decay. From Figure 6.1, an estimated photon arrival time at ECAL can be given by the following methods:

- From slow moving neutralinos:  $\Delta t_1 = (L_1/c\beta) - (L_1/c)$
- From non-directpath traveled:  $\Delta t_2 = (L_1 + L_2 - L_3)/c$
- ECAL measured time =  $\Delta t_1 + \Delta t_2$

Figure 6.7 shows the distribution of  $\Delta t_1$  and  $\Delta t_2$  indicating that most of our late arrival photons are produced from the decay of slow moving neutralinos, i.e.  $\beta \ll 1$ , as opposed to photons from non-direct flight or travel path to ECAL. These neutralinos are produced with low  $p_T$  such that the ratio  $\frac{p_T}{m_{\chi_1^0}} \ll 1$ .

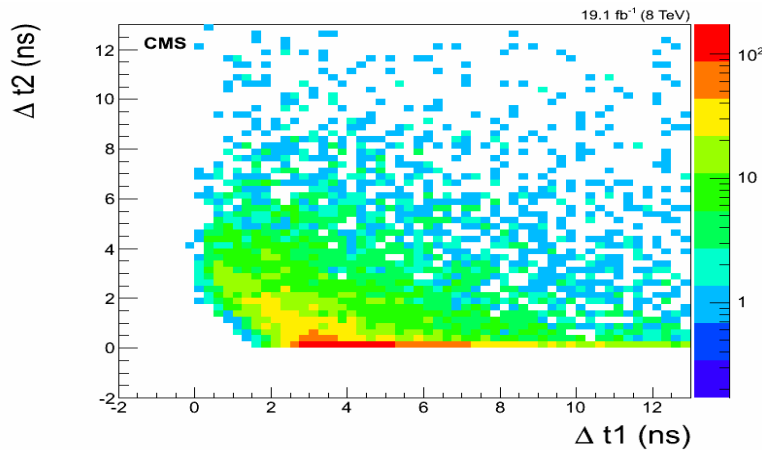
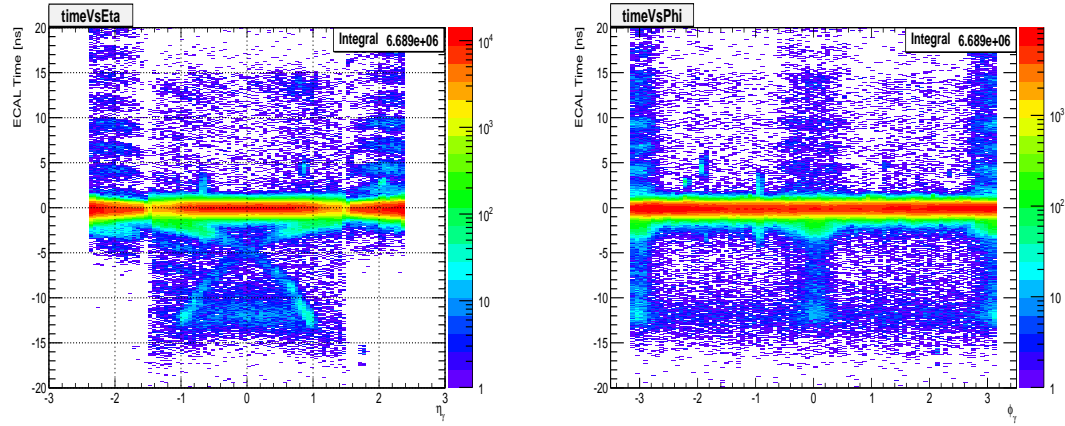


Figure 6.7: Sources of delayed photons produced from neutralino decay in the SPS8 model with  $\Lambda = 180$  TeV and  $c\tau = 6000$  mm arriving at ECAL.

### 6.3 Background Estimation

Our background estimation strategy is to first identify and reject as much non-collision background and anomalous events as possible then perform an ABCD background estimation technique on the irreducible residual background. We do this by comparing photon kinematic properties for in-time and off-time photon events. Separating our data sample into jet multiplicity and negative, in-time and positive time enable our approach to be possible. To better understand the different background sources and their contribution we make a two dimensional histogram of the photon  $\eta$  and  $\phi$  against the photon seed time and a one dimensional histogram of the timing distribution for different jet multiplicity events. These events pass the loose selection criteria for photons, jets and  $\cancel{E}_T$  already described in the previous section. The photon ECAL time Vs  $\eta$  and  $\phi$  inclusive 2-D distributions are shown in figure 6.8



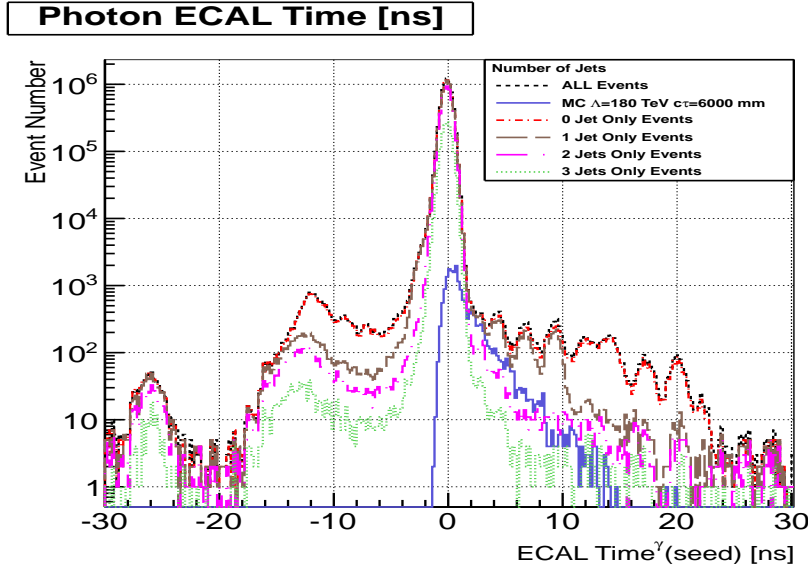


Figure 6.8: ECAL time against  $\eta$  (left) and ECAL time against  $\phi$  (right) for photons with  $p_T > 60$  GeV from data. The lower plot shows the photon timing distribution for events with different jet multiplicity.

The histograms in figure 6.8 show contributions from quite a variety of sources. The possible sources considered in this analysis include: QCD processes which we consider to be a combination of  $\gamma$ +jets, multijets and other processes producing photons from nominal proton-proton main bunch collisions. Most of the QCD processes are expected to have minimal contribution to large timing photons and  $\cancel{E}_T$  except due to timing miss-reconstruction and  $\cancel{E}_T$  miss-measurements or miss-identification of jets as photons. The events with significant contributions of possible or true large ECAL time measurements are produced from machine induced backgrounds (MIB)(arising from ghost/satellite bunch collisions) or beam halo muons, cosmic muons and anomalous events like spikes. These event do not only contribution significantly large photon times but also to large  $\cancel{E}_T$  which is our signal selection sample. We employ a data driven background estimation technique in this analysis described briefly as follows:

- Divide the dataset into individual samples peculiar to the expected kinematics and observation of each individual background source,
- Identify observable based on its kinematics which can be used as variables to

identify or tag and reject a particular background contribution with an acceptable amount of efficiency,

- Used alternate samples particular to each background source to calculate and verify the event tagging and miss-tag rate or efficiency,
- Use the tagging and miss-tag rates to estimate the background contribution of each individual background source in a well defined control region (CR) or sample,
- Use another CR as a closure test sample to verify our background estimation method.

All events are selected to be in the barrel i.e  $|\eta_\gamma| < 1.47$  as the overwhelming contribution of ghost/satellite bunch collisions observed in the endcap (EE)(see figure 6.6) and poor timing resolutions ( $\approx 3.0$  ns) make it very challenging to extend this analysis to include the endcap (EE). Our data driven method background estimation strategy involves splitting our single photon dataset into two major samples: Events with *Nominal or in-time* photons whose photon ECAL time is within  $\pm 2$  ns containing at least 2 jets, and events with *off-timing* photons where the photon ECAL time is  $2.0 < t_\gamma < 13.0$  ns and  $-10.0 < t_\gamma < -3$  ns with containing 0 or 1 jets. Our signal events are events containing photon(s) with ECAL time,  $2.0 < t_\gamma < 13.0$  ns, with at least 2 jets and large  $\cancel{E}_T$ . Our motivation is to avoid the observed spike overpopulated region with photon time ,  $t_\gamma \approx -12$  ns and because high jet multiplicity events are not usually MIB or non-collision events produced with  $p_T$ . On the other hand, nominal photons from QCD interaction are mostly produced in-time in association with more than 0 jets.

By comparing these two samples, we develop kinematics variables for studying and reducing contributions from collision and non-collision backgrounds.

### 6.3.1 Non-Collision Backgrounds

#### Halo Photons

##### Beam Halo

In addition to ghost/satellite bunches generating collisions events during collision, protons in ghost/satellite bunches can interact with collimators or gases such as H<sub>2</sub>, CO<sub>2</sub>

and others in the beam pipe leading to the production of high energy muons which later bremsstrahlung and shower directly in the calorimeter detectors. Main bunches due to betatron oscillations(departure of particles from nominal orbit in the transverse direction) can also through inelastic scattering with gas molecules in beam pipe about 550 m up from interaction point (IP)(since beam cleaning is not being 100% efficient), scattering on tertiary collimators (TCT) about  $z = 150$  m from IP and beam dump at about 150 m upstream CMS detector, produce through cascade decay energetic muons(sometimes muons with about 1 TeV) which bremsstrahlung in calorimeter detectors.

This kind of background from beam is referred to as *Machine Induced Background* (MIB) or *Beam-Induced Background* (BIB) and its contribution is called non-collision backgrounds as these are events observed in the detectors but not produced from the interaction point (IP). Throughout these thesis, we will refer to this kind of events as *Beam Halos or halos*. Because, they produce very high transverse momentum photons which can also be miss-identified as jets arriving in-time or out-of-time, they are a very important background in any analysis. In the later section, we will also show how we have developed new methods to identify and reject these kind of events and estimate its possible contribution to our analysis.

Muons with energy up to 1 TeV are produced when proton beam collides with collimators at  $z = 150$  m from the CMS detector interaction point or when proton beams collide with residual beam gas in the beam pipes. These are referred to as Beam-Induced Backgrounds (BIB). These muons through the process of bremsstrahlung produce high  $p_T$  photons with significantly large ECAL time, deposit their energy in ECAL crystals. The rate of BIB produced photons depend on the beam current and the operational conditions of the LHC such as machine optics, collimator settings, residual gas densities and filling scheme. These muons which travel in a near parallel flight path to the direction of main proton bunch in the beam pipe are referred to as *halo muons*. We expect halo muons to produce muon tracks in the Endcap muon systems (CSC and RPCs) with corresponding associated ECAL electromagnetic cluster in the ECAL. Halo muons can travel from one side of the detector, along the  $z$ -direction, to the other side of the detector if produced with sufficient energy. Their Time-Of-Flight (TOF) with respect to a potential hit position in the ECAL sub-detector can be estimated and

measured. The expected arrival time at ECAL of a halo muon traveling parallel along the beam line is estimated using it kinematics given in equation 6.1.

$$t_{\text{ECAL}}^{\text{expected}} = -1/c \left( \pm Z_{\text{cluster}} + \sqrt{Z_{\text{cluster}}^2 + R_{\text{cluster}}^2} \right) \quad (6.1)$$

$Z_{\text{cluster}}$  is the photon supercluster position or longitudinal distance along  $z$ -axis from nominal interaction point,  $R$  is the radial distance of the cluster from the beam line which is equal to  $R_{EB,\text{ECAL}} = 1.29$  m and  $c$  is the speed of light. One can further show that their expected arrival time in ECAL entirely depends on potential hit positions in ECAL and hence  $\eta$ . This is by reducing equation 6.1 to 6.2.

$$t_{\text{ECAL}}^{\text{expected}} = -\frac{R_{\text{cluster}}}{2c} \exp(-\eta) \quad (6.2)$$

Using this expression, we can compared halo flight path  $\eta$ -dependence as expected to what is observed from data. Our result in figure 6.9(*bottom, right*) confirm our expectation that most of the halo muons are produced from BIBs and tend to always produced photons with earlier (negative) arrival time in ECAL. In addition to using halo flight path to tag photons produced from halo muons, we also use halo muon hit positions in the Cathode Strip Chambers (CSC) matched to photon supercluster positions in the ECAL calorimeter. This is possible since halo muons are not bent in the azimuthal ( $\phi$ ) direction by the magnets and are mainly located around the  $y = 0$  plane. By measuring the difference in  $\phi$  between the CSC segment position and the ECAL photon cluster, we can associated with high percentage halo muons to photons produced from halo muons in ECAL. We call these photons *Halo Photons* and their matching to these halo muons is represented by a variable we call  $CSC(\text{Seg}, \gamma)\Delta\phi$ . A matching to within 3 deg shown in figure 6.9(*bottom, left*) provide a clear method of separating Halo photons from true photons from collision.

A distribution of the Halo photon time against the photon  $\phi_\gamma$  shown in figure 6.9(*top, right*) shows that most halo photon are distributed around  $\phi = 0, \pm\pi$  in agreement with our expectation since, the magnetic field in ECAL does not affect the flight path of Halo muons.

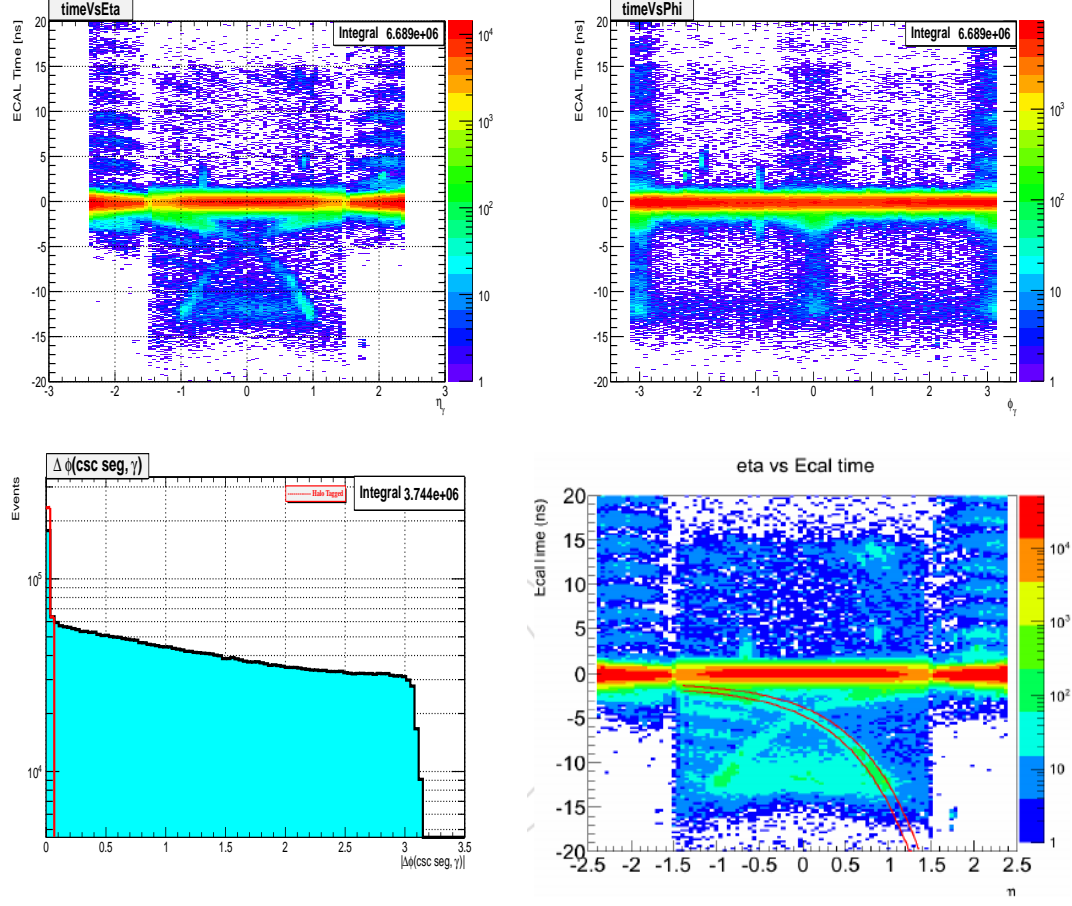


Figure 6.9: ECAL time Vs  $\eta$  (left) and ECAL time Vs  $\phi$  (right) and  $CSC(\text{Seg}, \gamma)\Delta\phi$  for photons with  $p_T > 80$  GeV from data. Halo photons show a clear matched between CSC segments and ECAL cluster in  $\Delta\phi$  with their distribution peaking at  $\phi = 0, \pm\pi$  and also the shape of their expected time.

### Cosmic Photons

Cosmic muons like beam Halo muons with sufficient energy will also bremsstrahlung in the ECAL producing photons referred here as *cosmic photons*. Unlike halo muons, cosmic muons can arrive at ECAL from any direction. Barrel cosmic photons are expected to be produced from cosmic muons with hits in the Drift Tubes (DT) segments. Using the DT hits and their corresponding photon supercluster  $\eta - \phi$  position in ECAL, we can match this hit position in DT segments to ECAL photon superclusters within  $\Delta\eta$  and  $\Delta\phi$ . The two dimensional distribution for  $DT\Delta\eta(DT, \gamma)$  and  $DT\Delta\phi(DT, \gamma)$  for

this matching for events with photon time above,  $t_\gamma > 2$  ns and time below,  $t_\gamma < -3$  ns is shown in figure 6.10. We conclude that events containing photons with small  $\Delta\eta$  and  $\Delta\phi$  to be candidate cosmic photons. Comparing this to  $\Delta\eta$  and  $\Delta\phi$  2-dimensional distributions of photons from a pure cosmic muons sample (data taken when no proton-proton collisions is happening) show these distributions to be very similar as seen in figure 6.10.

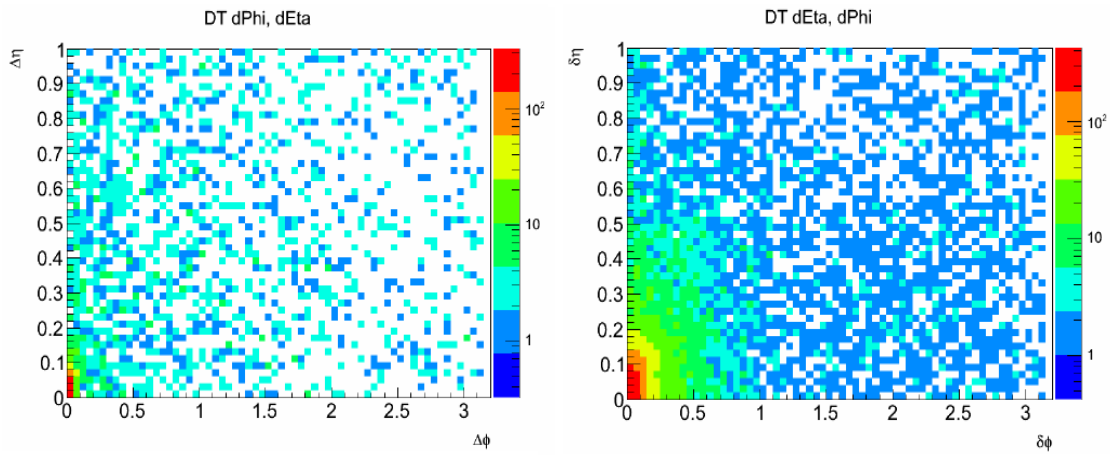


Figure 6.10: 2 dimensional plot showing  $DT\Delta\eta(\text{Seg}, \gamma)$  against  $DT\Delta\phi(\text{Seg}, \gamma)$  for photons with  $p_T > 80$  GeV, ECAL Time,  $t_\gamma > 2$  ns and ECAL Time  $t_\gamma < -3$  ns from proton-proton collision data (left) and pure cosmic muon data (right). Small  $\Delta\eta$  and  $\Delta\phi$  are cosmic photon candidates.

### Anomalous Photons: Spikes

Neutrons and some charge hadrons which deposit their energy directly to the APDs instead of the crystal scintillation are referred to as *anomalous signal* or *spikes*. Spikes can mimic the kinematics of true photons from proton-proton collisions leading to the miss-identification of spikes as true photons. Spikes like true energetic photons can be isolated and so easily pass photon isolation cuts without being identified. A spike supercluster usually consists of very few crystals and most of the time single or double crystals except when embedded in a true photon of high electromagnetic fraction jets where they consist of many crystals and are difficult to identify. However, most spikes show a different signal pulse shape to that of true photons and also have large negative

ECAL time especially at  $t_\gamma \approx -12.0$  ns region. In addition to using energy topological selection cuts, which are based on the spike crystal energy deposits, during ECAL cleaning one can also use the  $\chi^2$  fit value of the timing reconstruction to identify and reject spikes. Spike cleaning is performed during online and offline super cluster reconstruction. However, this online cleaning is not entirely very efficient. Since ECAL clusters belonging to spikes are usually made up of very few crystals compared to photons clusters with many crystals, using the number of crystals in a reconstructed super cluster can be used to distinguish true isolated photons from events with spikes. It has been observed that spike contributions increase with increase in LHC luminosity. Thus, as a selection criteria, photons passing our cosmic photons and halo photons identification and with number of good crystals less than 7 are considered to be spike candidates. Figure 6.11 shows the distribution of the number of crystals in a photon super cluster comparing photons with ECAL time,  $t_\gamma < 0$  ns, in-time photons (ECAL  $-2.0 < t_\gamma < 0$  ns) and selected spike and halo control sample. The spike control sample is selected using the spike energy topological cut “swiss-cross” variable in the region with  $t_\gamma \approx -12.0$  ns where it is observed that spike concentration is high, is used to identify and reject events with spikes during super cluster reconstruction. We observe as shown in figure 6.11(*left*) that most spikes always have fewer(< 7) crystals in their photon supercluster.

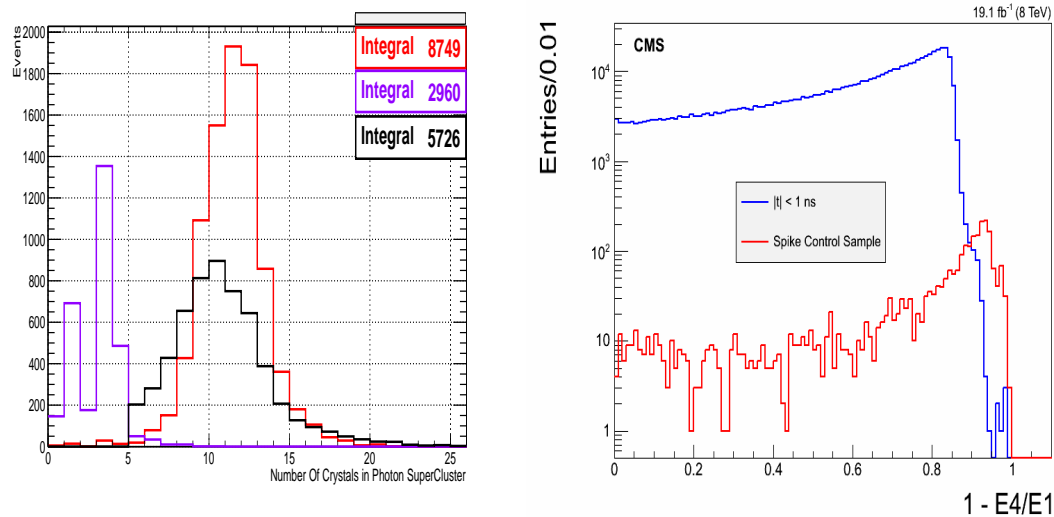


Figure 6.11: Plot showing *number of crystals* in photon supercluster for photons from the region with ECAL Time,  $t_\gamma < 0$  ns. Figure shows the timing distribution of candidate true photons(black), spike candidate photons (magenta) and halo candidate photons (red). The toplogical swiss-cross variable ( $1 - E_4/E_1$ ) distribution is shown comparing true photons ( $|t_\gamma| < 1.0$ ) to spike populated sample.

### 6.3.2 Collision Backgrounds

#### QCD Photons and Pile Up

Collisions from the main proton bunches happening every 50ns during 2012 LHC Run I are not the only collisions that can occur at the LHC. The presence of satellite/ghost bunches spaced in 5.0 ns or 2.5 ns discussed in section 3.1.5 along LHC bunch structure can also collide producing delayed photons either from collisions between these satellite/ghost bunches or with the main proton bunch. As observed in figure 6.6, photons from these events are a serious background source to delayed photons and most of these photons will pass all the above event and photon selection criteria. Thus, it is imperative to estimate delayed photon contributions from satellite/ghost bunches is it is not negligible. Since these background source is non-reducible and the kinematics of these events are very similar, we employ the standard ABCD method to for estimating these background contribution to the signal region. However, we only perform this estimation after cleaning for possibly non-collision event contamination.

#### 6.3.3 Event Cleaning, Veto Performance and Fake Rate

Using the derived kinematic variables for halo, cosmic and spike photons, we apply selection cuts on these variables for tagging and rejecting contributions from non-collision events. These cuts are applied in addition to our above event selections cuts to perform the following event cleaning:

- Veto 0-jet events as this sample is highly populated with beam halo events,
- Veto events with  $CSC\Delta\phi(Seg, \gamma) < 0.05$ ,
- Veto events with  $\Delta\eta(DTSeg, \gamma) < 0.1$  and  $\Delta\phi(DTSeg, \gamma) < 0.1$  .
- Only photons with  $|\eta_\gamma| < 1.45$  are considered,

- Veto events with photons with Number of Good crystals < 7 and  $1 - E_4/E_1 > 0.98$ .
- Remove photons tagged as halo and cosmic photons,
- Veto events with less than 2-jets.

Events which pass all these additional selection criteria make up the sample which is used to estimate our final background to our signal. Since it is very challenging to define pure control samples for each non-collision background source without possible contamination, we estimate the fake rates from the above veto or rejection conditions using in-time ( $|t_\gamma| < 2.0$  ns) photon sample where we believe non-collision contribution is small compared to true photons from collision. Our measured fake rates are shown in table 6.9.

| Background Source   | Fake Rate(%)  |
|---------------------|---------------|
| <i>Halo Photons</i> | $\approx 3$   |
| <i>Cosmic Muons</i> | $\approx 1.4$ |
| <i>Spikes</i>       | $\approx 0.4$ |

Table 6.6: Fake rates for different non-collision cleaning.

After performing our event cleaning criteria, tagging and rejection of most of halo, cosmic and spike events, our residual background photon timing distribution is shown in figure 6.12 with the different sources of our background tags. We now perform an ABCD background estimation technique on this residual background to estimate possible contamination of the remaining non-collision background to signal.

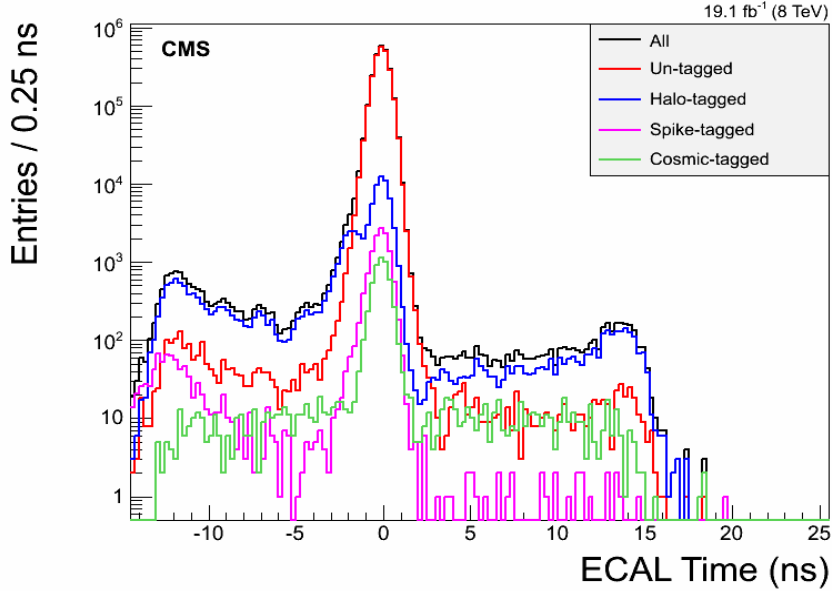


Figure 6.12: Residual Background after tagging the different non-collision background sources using the methods described in text.

### Residual Background Estimation Using ABDC Technique

In order to estimating the background contribution from collision and non-collision sources, we employ a 3-dimensional space involving  $\cancel{E}_T$ ,  $\cancel{E}_T^\gamma$  and photon ECAL time,  $t_\gamma$ . Our signal events are those with  $3.0 < t_\gamma < 13.0$  ns with large  $E_T^{\text{miss}}$ , and by large  $E_T^{\text{miss}}$ , we mean events with  $\cancel{E}_T > 60$  GeV,  $\cancel{E}_T^\gamma > 60$  GeV. Non-collision events as already seen can also have large time, since they are mostly out-of-time and by  $E_T^{\text{miss}}$  calculation and corrections(see discussion above) should have large  $\cancel{E}_T$  and small  $\cancel{E}_T^\gamma$ . Events from collision on the other hand are produced mostly in-time ( $-2.0 < t_\gamma < 2.0$  ns) except in cases of timing mis-measurements or ghost/satellite contributions where  $t_\gamma > 3.0$  ns. Collision events, mostly produced through SM interactions, cannot be produced with large correctly calculated  $E_T^{\text{miss}}$ , e.g.  $\gamma + \text{jets}$  events are produced with very small  $E_T^{\text{miss}}$ , however due to timing mis-measurements, they may appear out-of-time and assigned large  $E_T^{\text{miss}}$ . Thus we conclude that collision events will generally have small  $\cancel{E}_T$  but large  $\cancel{E}_T^\gamma$ .

We select control samples (CS) defined by  $\cancel{E}_T$ ,  $\cancel{E}_T^\gamma$  and  $t_\gamma$  according to the ABCD

technique to estimate our background contributions while remaining vigilant and taking into account the possible contamination to each background source from possible fluctuations in event rate as a result of our selection cuts in defining these CRs. The overall estimation technique is verified through a closure test procedure and the collision background estimation is validated using an extra control sample of  $Z \rightarrow e^+e^-$  events for  $Z$  candidates reconstructed from photon candidates extended to include out-of-time events.

1.  **$\cancel{E}_T > 60 \text{ GeV}$ :** CS in which collision (QCD) background is suppressed while halo, cosmic ray and spike photon is enhanced since most non-collision background photons are produced with high  $p_T$  hence large  $\cancel{E}_T^\gamma$ . Using this CS, we define four regions for estimating the non-collision background contribution using the ABCD recipe.

| Non-Collision                        | $\cancel{E}_T < 60 \text{ GeV}$ | $\cancel{E}_T > 60 \text{ GeV}$ |
|--------------------------------------|---------------------------------|---------------------------------|
| $3.0 < t_\gamma < 13.0 \text{ ns.}$  | $C$                             | $D$                             |
| $-10.0 < t_\gamma < -3.0 \text{ ns}$ | $A$                             | $B$                             |

Table 6.7: ABCD Control Regions (CRs) for estimating non-collision background.

Thus, the number of events expected in Control Region (CR)  $D$  using table 6.7 with the assumption that  $\frac{N_D}{N_B} = \frac{N_C}{N_A}$  is given as:

$$N_D = \left( \frac{N_B}{N_A} \right) \cdot N_C \quad (6.3)$$

2.  **$\cancel{E}_T > 60 \text{ GeV}$ :** CS where non-collision background (halo, cosmic and spike photons) contribution is suppressed while collision (QCD) background contribution is enhanced. Further dividing this CS and applying  $A' B' C' D'$  method to estimated collision contribution is shown in table 6.8.

| Collision                            | $\cancel{E}_T < 60 \text{ GeV}$ | $\cancel{E}_T > 60 \text{ GeV}$ |
|--------------------------------------|---------------------------------|---------------------------------|
| $3.0 < t_\gamma < 13.0 \text{ ns.}$  | $C'$                            | $D'$                            |
| $-2.0 < t_\gamma < 2.0 \text{ ns}$   | $I'$                            | $I$                             |
| $-10.0 < t_\gamma < -3.0 \text{ ns}$ | $A'$                            | $B'$                            |

Table 6.8:  $A' B' C' D'$  and  $I I'$  CRs for estimating collision background.

Using CRs defined in table 6.8, we can estimate the contributions of collision background in both CRs  $B$  and  $D$  of our non-collision background CS as follows:

$$N_B^{col} = N_{B'} = \left( \frac{I}{I'} \right) \cdot N_{A'}, \quad N_D^{col} = N_{D'} = \left( \frac{I}{I'} \right) \cdot N_{C'} \quad (6.4)$$

where we have assumed that  $\frac{N_{B'}}{N_{A'}} = \frac{N_I}{N_{I'}}$  and  $\frac{N_{D'}}{N_{C'}} = \frac{N_I}{N_{I'}}$ .

$N_B^{col}$  and  $N_D^{col}$  are collision contributions to CRs  $B$  and  $A$ . The final combined background estimation is given by equation 6.5.

$$N_D^{Total} = \left( \frac{N_B - N_B^{col}}{N_A} \right) \cdot N_C + N_D^{col} \quad (6.5)$$

where  $N_D^{Total} = N_D^{non-col} + N_D^{col}$  is the total background estimation in our signal region.

### Closure Test

Selecting events with 0-jets and 1-jet, we performed closure test of our background estimation method. We also perform a cross-check on the assumptions used in our background estimations for small contributions for collision background using  $Z \rightarrow e^+e^-$  events. Our underlying assumption here is that background contributions to large timing from collision source referred here as QCD is very small and must be of the order of  $10^{-5}$  in comparison to in-time photons. i.e the ratio  $N_{|t_\gamma|>3\text{ ns}}/N_{|t_\gamma|<2.0\text{ ns}} \approx 10^{-5}$  with  $N$  being the number of photons. The closure test compares the number of events observed in CR  $D$  to the number expected using our ABCD background estimation method in the same CR  $D$ . We observed 10 events while from using equation 6.5, we expected  $16.78^{+2.95}_{-3.45}$ . We argue that within our statistical uncertainties, there is quite an agreement between our expectation and observed events. The complete result from our closure test is shown in table 6.9. This gives us confidence that our background estimation method is robust and reliable. We apply the same ABCD to estimate the background contribution in our signal sample. Our signal sample consist of events with at least 2-jets, at least a single photon and  $\cancel{E}_T > 60\text{ GeV}$ ,  $\cancel{E}_T > 60\text{ GeV..}$

| Non-Collision                        | $E_T < 60 \text{ GeV}$ | $E_T > 60 \text{ GeV}$ |
|--------------------------------------|------------------------|------------------------|
| $3.0 < t_\gamma < 13.0 \text{ ns}$   | C(405)                 | D(10) <b>16.78</b>     |
| $-10.0 < t_\gamma < -3.0 \text{ ns}$ | A(871)                 | B(36)                  |
| Collision                            | $E_T < 60 \text{ GeV}$ | $E_T > 60 \text{ GeV}$ |
| $3.0 < t_\gamma < 13.0 \text{ ns}$   | $D'(4)$                | D(10)                  |
| $-2.0 < t_\gamma < 2.0 \text{ ns}$   | $F'(1353685)$          | F(34543)               |
| $-10.0 < t_\gamma < -3.0 \text{ ns}$ | $B'(5)$                | B(36)                  |

Table 6.9: Result from closure test of background estimation technique using 0 and 1-jet events. Numbers in bracket represent our expected background estimate using ABCD method.

### 6.3.4 Background Estimation Cross Check

The main assumption in our background estimation technique is that, the contribution from collision background events to out-of-time regions ( $3.0 < t_\gamma < 13.0 \text{ ns}$ ) is negligible. In order to show that this assumption is correct, we select  $Z \rightarrow e^+e^-$  events from `SingleElectron` and `DoubleElectron` data sets of 2012. Our motivation is to use a control sample where contributions from non-collision events is very small. We select  $Z$  candidate events from an extended photon sample including out-of-time photon events according to the following selection criteria:

- The candidate two electrons for the  $Z$  bosons must have individual  $p_T > 25 \text{ GeV}$ ,
- The di-mass of these two electrons,  $|m_{e^+e^-} - 91| > 61 \text{ GeV}/c^2$ ,
- Each electron must be in the barrel,  $|\eta_{e^-}| < 1.479$  and  $|\eta_{e^+}| < 1.479$ .

At the electron super cluster level, we used the seed crystal time adjusted to account for the electron time of flight, as the electron time. The seed crystal must satisfy the recommended crystals or rechit cleaning criteria by the ECAL group which include `kWeird`, `kBad`, `kPoorCalib` used for rejecting crystals showing anomalous behavior like spikes, noisy, bad crystals or poorly calibrated crystals. In this cross-check, we define our signal region as  $Z$ -candidate events with a well defined mass from both electrons i.e  $76 < |m_{e^+e^-}| < 100 \text{ GeV}/c^2$  while the non  $Z$  events control sample are events which do not fall into this signal category. A quick look at photon  $t_\gamma$  vs  $\eta_\gamma$  and  $\phi_\gamma$  plots as

previously shown for halo photons in figure 6.9, shows that the electron candidates from the **Single/DoubleElectron** dataset when compared to the **SinglePhoton** dataset in figure 6.13 show no or very little contribution from cosmic, halo and anomalous photon events. This confirms our choice of the  $Z$  candidate events sample as a reliable sample to study collision events as it is free from non-collision events.

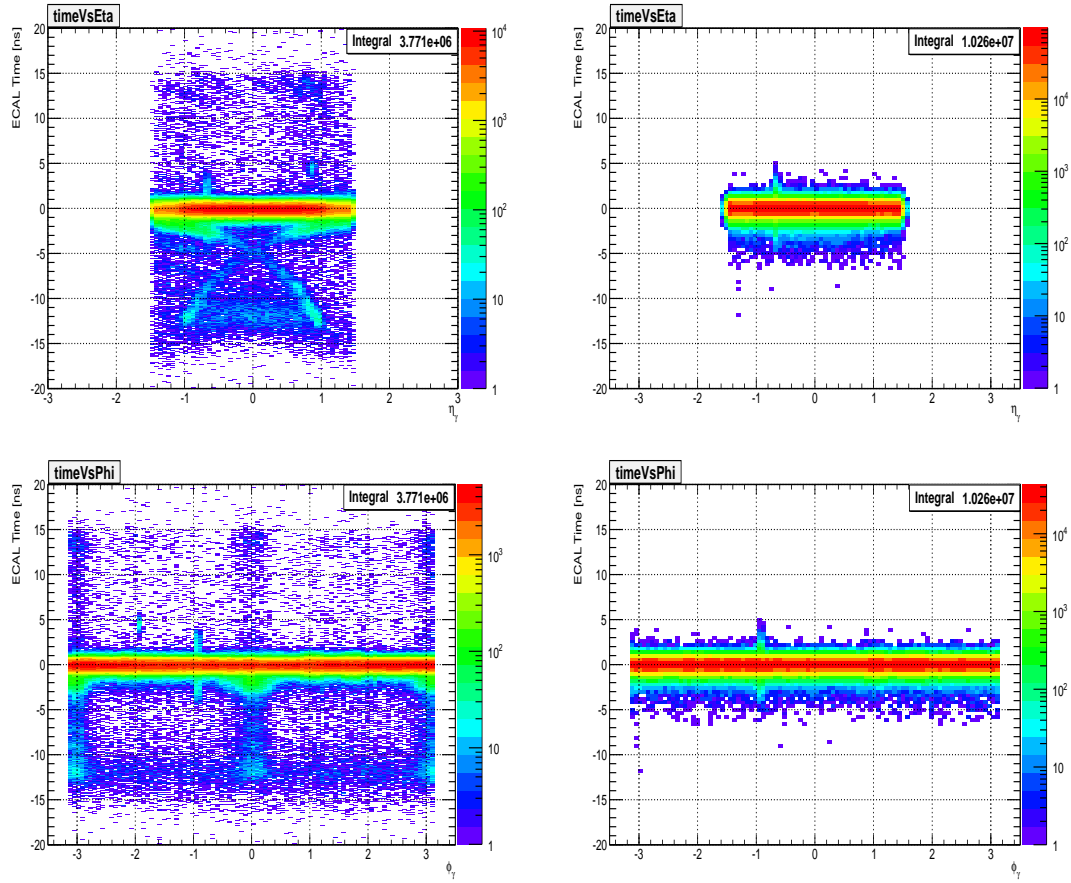


Figure 6.13: ECAL time,  $t_\gamma$  Vs  $\eta_\gamma$ (top) and  $t_\gamma$  Vs  $\phi$  (bottom) for photons from **SinglePhoton** dataset (left) compared to electron candidates from the **DoubleElectron** dataset (right). All photons or electron candidates are in barrel subdetector. Most of the photons with  $\phi = 0, \pm\pi$  are halo photons which are not observed in the  $Z$  boson candidate sample.

Figure 6.14 shows the  $Z$  boson mass reconstructed from the candidate electrons and timing of each electron for Signal (*top and blue*) and for our control sample (*bottom and*

red).

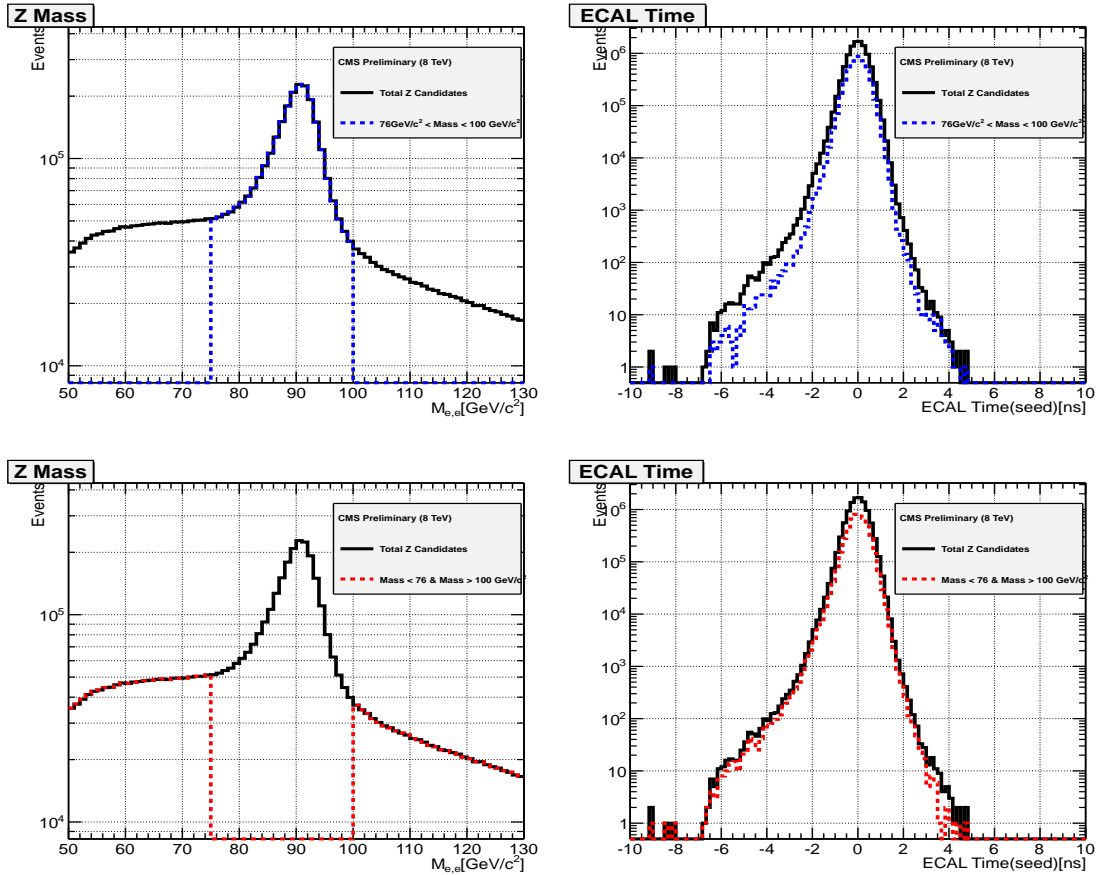


Figure 6.14: Di-electron candidate mass distribution and the time of both electrons for the signal  $76 < m_Z < 100$  GeV/ $c^2$   $Z$  boson sample(left) and similar distributions from the Control ( $50 < m_Z < 76$  GeV/ $c^2$  and  $100 < m_Z < 130$  GeV/ $c^2$ ) sample (right). Candidates events from the DoubleElectron dataset.

Using the background  $Z$  control sample, we estimate its contribution to out-of-time events using a simple scaling methods which can also be understood as an ABCD method. The method is applied as follows:

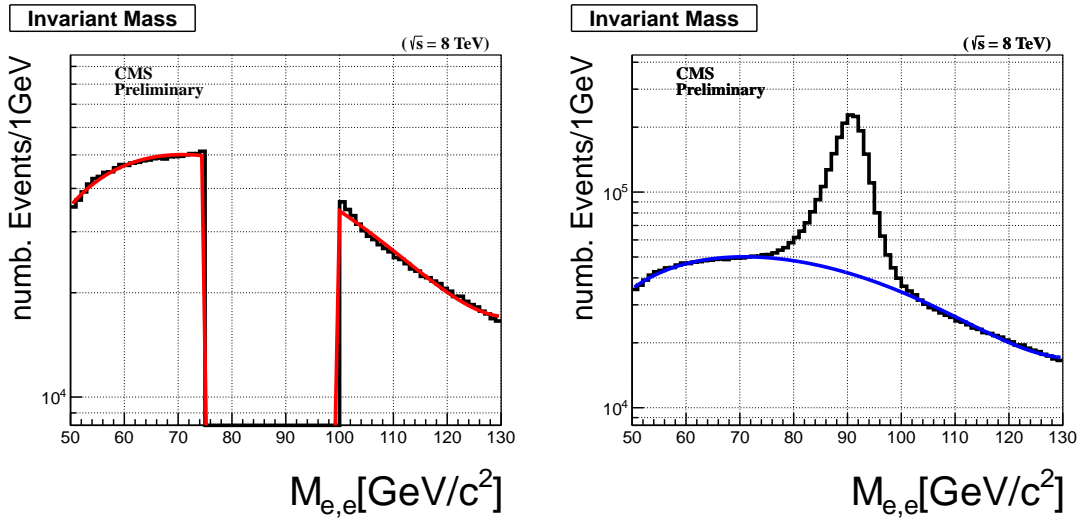
- Using a polynomial function, we fit the di-electron candidate mass distribution of the background control sample to extract a set of fit parameters,

- Using these fit parameters to define our polynomial function, we use this function to extract a scaling factor use to determine the true contribution of the background control region events in the signal region which in this case are  $Z$  bosons with possible large ECAL timing,  $|t| > 3$  ns.
- We scale the background control sample timing distribution (electrons time) using the extracted scale factor. This scale factor is defined as,

$$\text{Scale Factor} = \frac{N}{M_1 + M_2}$$

- By subtracting the scaled background control sample  $Z$  candidates timing distribution from the signal sample  $Z$  candidate timing distribution, we are left with the real  $Z$  boson events whose electron time can fluctuate into larger timing region.
- Comparing the total number of observe electron candidates with  $t > 3$  ns to those in-time,  $|t| < 2$  ns, their ratio i.e  $N_{t>3\text{ ns}}/N_{|t|<2.0\text{ ns}}$  gives us an estimate of the possible genuine electromagnetic objects from collision with large ECAL timing.

A simple picture showing the above procedure with distributions is shown in figure 6.15.



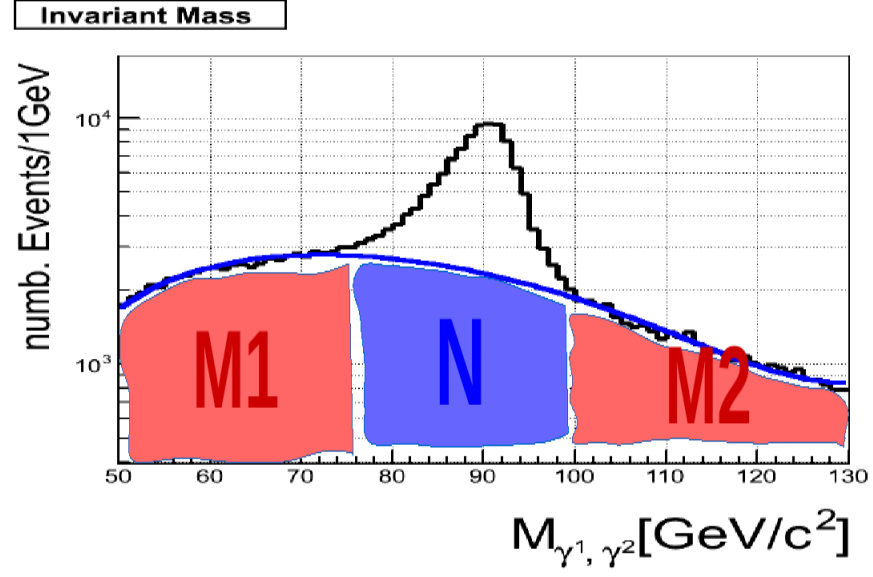


Figure 6.15: *Top:* Control sample (left) and signal sample (right) of di-electron candidate mass distribution. *Bottom:* Figure showing definition of scale factor use in estimating the contributions from control sample in signal sample.

The result of the final timing distribution for genuine  $Z$  boson events is shown in figure 6.16. It is not difficult to see that the ratio  $N_{t>3 \text{ ns}}/N_{|t|<2.0 \text{ ns}} < 10^{-5}$  confirming that indeed the contribution of electromagnetic objects with large timing  $t > 3$  ns is negligible and in agreement with our assumption that most collision events contain photons which are mostly in-time,  $|t| \leq 2$  ns. Its important to note that, we have not applied any  $E_T^{\text{miss}}$  selection cuts here. A simple cut,  $E_T^{\text{miss}} > 60 \text{ GeV}$  could further reduce this ratio to an even smaller number as assumed in our above background estimation.

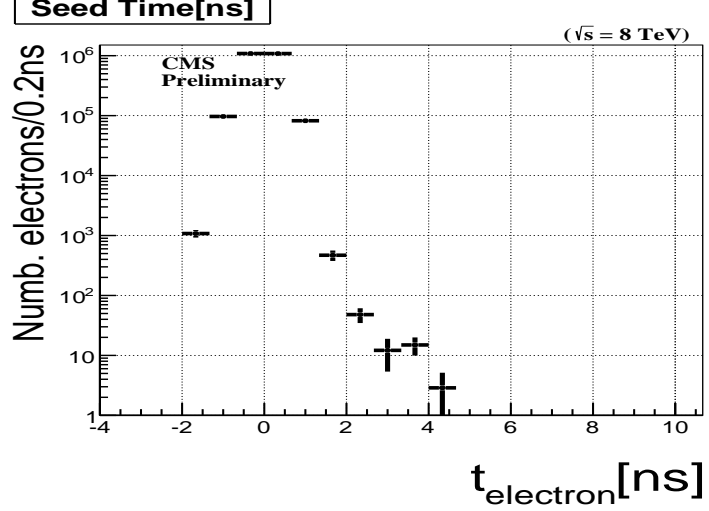


Figure 6.16: Timing distribution of genuine  $Z$  bosons after background contribution has been subtracted.

## 6.4 Results

Finally, we perform our background estimation on signal samples which are events with at least 2 jets, at least one high  $p_T > 80 \text{ GeV}/c$  isolated photon with ECAL time  $3.0 < t_\gamma < 13.0 \text{ ns}$  or  $-10.0 < t_\gamma < -3.0 \text{ ns}$  and  $E_T^\gamma > 60 \text{ GeV}$ ,  $E_T > 60 \text{ GeV}$ .

We observed 1 event and expected  $0.0888^{+0.1869}_{-0.0444}$  background events within our statistical uncertainties. Our complete result is shown in table 6.10 and in table 6.11, we show the number of GMSB SPS8 signal events passing our final selection for  $\Lambda = 180 \text{ TeV}$  with different  $c\tau$  values of the neutralino.

| Non-Collision                        | $E_T < 60 \text{ GeV}$ | $E_T > 60 \text{ GeV}$           |
|--------------------------------------|------------------------|----------------------------------|
| $3.0 < t_\gamma < 13.0 \text{ ns}$   | $C(0)$                 | $D(1)$                           |
| $-10.0 < t_\gamma < -3.0 \text{ ns}$ | $A(5)$                 | $B(1)$                           |
| Collision                            | $E_T < 60 \text{ GeV}$ | $E_T > 60 \text{ GeV}$           |
| $3.0 < t_\gamma < 13.0 \text{ ns}$   | $D'(5)$                | $D \ 0.0888^{+0.1869}_{-0.0444}$ |
| $-2.0 < t_\gamma < 2.0 \text{ ns}$   | $F'(657663)$           | $F(30242)$                       |
| $-10.0 < t_\gamma < -3.0 \text{ ns}$ | $B'(1)$                | $B \ 0.23^{+0.092}_{-0.118}$     |

Table 6.10: Result of observed events and estimated background from signal sample, events with at least 2-jets. Numbers in bracket represent our observed number of events while numbers not in bracket are our expected number of background events estimated using ABCD method.

| SPS8 GMSB Signal   | Number of Events |
|--|------------------|
| GMSB(SPS8) ( $\Lambda = 180 \text{ TeV}, c\tau = 250 \text{ mm}$ )   | 0.2096           |
| GMSB(SPS8) ( $\Lambda = 180 \text{ TeV}, c\tau = 500 \text{ mm}$ )   | 4.5423           |
| GMSB(SPS8) ( $\Lambda = 180 \text{ TeV}, c\tau = 1000 \text{ mm}$ )  | 6.3646           |
| GMSB(SPS8) ( $\Lambda = 180 \text{ TeV}, c\tau = 2000 \text{ mm}$ )  | 6.3968           |
| GMSB(SPS8) ( $\Lambda = 180 \text{ TeV}, c\tau = 4000 \text{ mm}$ )  | 6.1442           |
| GMSB(SPS8) ( $\Lambda = 180 \text{ TeV}, c\tau = 6000 \text{ mm}$ )  | 4.6498           |
| GMSB(SPS8) ( $\Lambda = 180 \text{ TeV}, c\tau = 12000 \text{ mm}$ ) | 2.918            |

Table 6.11: Final number for  $\Lambda = 180 \text{ TeV}$  GMSB SPS8 MC signal events passing our selection cuts.

## 6.5 Systematic Studies

The different sources of systematic which affect this analysis and the estimated contribution of each identified source of systematic is shown in table 6.12. These systematic is also used in the calculation of the upper limit on observed signal cross-section. We obtained these systematic percentage by varying each individual source and see how that affects the number of events passing our selection cuts. The systematic uncertainty on luminosity measurement has the recommended value of 2.2% provided by CMS and LHC luminosity measurements. The uncertainty for the jet energy corrections (JEC) and jet energy scale (JES) has also been measured using the standard CMSSW tool by [50] and provided by the CMS JEMET working group. The uncertainty on the photon energy scale in barrel was estimated to be 1.0% and based on the final-state radiation (FSR) in  $Z \rightarrow \mu\mu\gamma$  events [51]. The uncertainty from parton density functions (PDF) evaluated using the re-weighting technique using the Master Equation of CTEQ65 model set described in [52]. The uncertainty on the  $E_T^{\text{miss}}$  resolution uses a conservative estimate from [53]. The uncertainty on the ECAL timing obtained by comparing the peak in the timing distribution between  $\gamma +$  jet sample and data events with time  $|t| < 2 \text{ ns}$  is found

to be of the order of 200 ps per event and from a study of high  $p_T$  photons beyond gain transitions has agreed by ECAL DPG to be a conservative estimate. Another important source of systematic is in the selection of the background control samples and our background estimation and individual systematic in the tagging and miss-tagging of non-collision background and estimating background contributions from collisions. We combined these separate systematic contributions into a single background estimation systematic referred here as our background estimation systematic. This is our largest source of uncertainty in our analysis which we estimate to vary from 50% to 200%.

| <b>Source</b>                            | <b>Uncertainty on <math>\sigma_{UL}^{Exp}(\%)</math></b> |
|--|--|
| Photon energy scale (1.0%)               | < 3.0%   |
| Jet energy scale                         | < 0.05%  |
| Jet energy resolution (10%)              | < 1.90%  |
| PDF uncertainty (10%)                    | < 1.70%  |
| $E_T^{\text{miss}}$ resolution (10%)     | < 2.8%   |
| ECAL time uncertainty (0.5 ns)           | < 5.0%   |
| Background estimation uncertainty (50.0) | < 51.0%  |
| Luminosity (4.5%)                        | < 2.2%   |

Table 6.12: Summary of systematic uncertainties used in this analysis and applied to our cross-section upper limit,  $\sigma_{UL}$  calculation.

## Chapter 7

# Statistical Analysis

### 7.1 Limit Computation

The upper limit calculation procedure used in this analysis is the CLs technique. We fed carefully estimated amounts of background and signal with systematic to obtain the limit. The variable for which the 95% upper limit is set unlike previous experiments is based entirely on the neutralino proper decay length,  $c\tau_{\tilde{\chi}_1^0}$ .

The method we used in our upper limit calculation is by first performing a Hypothesis test and then use the result of this test to derived our confidence intervals. We do the following:

- We define a NULL hypothesis ( $H_0$ ) and the Alternate hypothesis ( $H_1$ ). If we had several other hypothesis, we will defined them also.
- Select a Test statistics ( $t(x)$ ), where  $x$  is the data.
- Select a corresponding test statistics calculator.
- Use the result of the hypothesis test to compute the interval by inverting the result of the hypothesis test.

First, we describe the acceptable technique in experimental high energy physics for computing *p-values* used in any search and discovery experiment.

### 7.1.1 CLs Technique

The  $CL_s$  technique [57] is attributed as the standard technique or framework for computing the confidence or exclusion intervals in a search and discovery experiment. It has been shown to work during the search for the Higgs boson at LEP and recently in the discovery of the scalar boson in 2012, by both CMS and ATLAS experiments with the mass of this boson being:  $m_H = 125.36 \pm 0.37(\text{stat.Unc}) \pm 0.18(\text{syst.Unc})$ .

This method has been implemented in a unique statistical software package called *HiggsCombine* with the goal of providing direct access to a variety of robust statistical methods with optimised performance for computing limits or confidence intervals. *HiggsCombine* [59] is the official standard tool recommended by the CMS statistical committee and CMS Higgs group for calculating limits in any CMS search and discovery analysis. It takes as input estimates on the number or distribution of signal and background and the observed number or distribution from data and produces an upper limit in the production cross section of a given physics process for a given value of a parameter of interest (POI). *Higgscombine* tool has the advantage in that, it allows for the possibility to use several different statistical methods of calculating the upper limit. This way, one can make comparison and simple checks for any inconsistency. In this analysis, we used an Asymptotic [60] and HybridNew (a hybrid of Frequentist and Bayesian methods),[59], to calculate our observed upper limits. The purpose of the using the  $CL_s$  method is to compute reliable upper limits in a search scenario when the observed signal is very small compared to the background. In the  $CL_s$  technique, one uses not the p-value ( $CL_{s+b}$ ) but rather divide this by  $CL_b$  (which is 1 minus the p-value for background only hypothesis). The reason for this is to define a conditional probability conditioned to the scenario of observing only background or background only hypothesis. The  $CL_s$  is formally defined as:

$$CL_s = \frac{CL_{s+b}}{CL_b} = \frac{p_{s+b}}{1 - p_b} \quad (7.1)$$

where  $s + b$  means signal and background.

### 7.1.2 Statistical Test Formalism

The Neyman-Pearson Theorem states that the likelihood ratio gives the most powerful hypothesis test. Therefore, we construct our test statistics  $t_\mu$  as a function of the observed data, as a likelihood ratio. In a search analysis, one defines the null hypothesis  $H_0$  describing only known processes, or the background only which is to be tested against an alternate hypothesis  $H_1$  defined as a background and signal. However in the computation of upper limits:

- $H_0$  being the NULL hypothesis includes the background and signal ( $s + b$ ) while
- $H_1$  being the ALTERNATE hypothesis includes only the background ( $b$ ).

Using these, two hypothesis we quantify the level of agreement between our observed data with either of the hypothesis by computing a  $p$ -value ( $p$ -value if the probability under the assumption of a given hypothesis, of finding data of equal or greater incompatibility with the predictions of the given hypothesis). A given hypothesis is then regarded as being excluded if its  $p$ -value is observed below a given threshold. In particle physics, this threshold value for the  $p$ -value is 0.05 corresponding to 95% of confidence level (CL). The CMS accepted method of computing upper upper limit is based on mix of frequentist-hybrid significance test using the profilelikelihood ratio as a test statistics (HybridNew method). The parameter of interests in in our case the rate (cross section) of signal process as well as *nuissance parameters* as systematics for the background and signal models. This parametrized systematics effects results, as is always the case, to loss in sensitivity.

In this search experiment, for each event in the signal, we measured the timing of the photon as our observable. We use this value to construct a histogram  $\mathbf{n} = (n_1, \dots, n_N)$ . The expectation value for each value of  $n_i$  can be written as:

$$E[n_i] = \mu s_i + b_i \quad (7.2)$$

where  $\mu$  is the parameter which determines the signal strength, when  $\mu = 0$  means background-only and when  $\mu = 1$  then we have the signal and background hypothesis.

The the mean number of entries in the  $i$ th bin from signal and background are given as:

$$s_i = s_{tot} \int_{bin,i} f_s(t; \theta_s) \quad b_i = b_{tot} \int_{bin,i} f_b(t; \theta_b) \quad (7.3)$$

with the functions  $f_s(t; \theta_s)$  and  $f_b(t; \theta_b)$  being the probability density functions (Pdfs) of the variable  $t$  for the signal and background events and  $\theta_s$  and  $\theta_b$  representing the parameters which characterise the shapes of the pdfs.  $s_{tot}$  and  $b_{tot}$  represents the total mean numbers of signals and backgrounds while the integrals represent the probabilities for an event to be found in bin  $i$ .  $\theta = (\theta_s, \theta_b, b_{tot})$  denote all nuisance parameters (systematic uncertainties) while  $s_{tot}$  is the signal normalization is fixed to the value predicted by the nominal signal model.

The likelihood function is the product of the Poisson probabilities for all bins:

$$\mathcal{L}(\mu, \theta) = \prod_{r=1}^N \frac{(\mu s_r + b_r)^{n_r}}{n_r!} e^{-(\mu s_r + b_r)} \cdot \mathcal{G}(\theta) \quad (7.4)$$

where  $\mathcal{G}(\theta)$  is a discrete (Poisson) distribution of the nuisance parameters. This distribution can be different for different nuisance parameter.

Using the likelihood function, the profilelikelihood ratio is then defined as:

$$\lambda(\mu) = \frac{\mathcal{L}(\mu, \hat{\theta})}{\mathcal{L}(\hat{\mu}, \hat{\theta})} \quad (7.5)$$

Here  $\hat{\theta}$  is the the value of  $\theta$  that maximizes  $\mathcal{L}$  for a specified  $\mu$ , thus, it is referred to as the *conditional maximum-likelihood estimator* (CMLE) of  $\theta$  (given as a function of  $\mu$ ). While  $\mathcal{L}(\hat{\mu}, \hat{\theta})$  is the maximized (unconditional) likelihood function with  $\hat{\mu}$  and  $\hat{\theta}$  being its *maximum likelihood* (ML) estimators. The nuisance parameters broadens the profilelikelihood as a function of  $\mu$  relative to what is expected if their values where fixed and this reflects in the loss of sensitivity or information about  $\mu$  due to the systematic uncertainties.

### 7.1.3 Test Statistics and $p$ -values

The above expression for  $\lambda(\mu)$  shows that  $0 \leq \lambda \leq 1$ , where  $\lambda$  close to 1 indicates a very good agreement between the data and hypothesis value of  $\mu$ . The test statistics to be used for our statistical test is defined as:

$$t_\mu = -2 \ln \lambda(\mu) \quad (7.6)$$

It is important to note that the test statistics approach to any statistical test is favourable because just by looking at the values of the test statistics, higher values corresponds to increasing incompatibility between the data and the value of  $\mu$  which is from the signal hypothesis. This incompatibility or disagreement between the data and a given hypothesis is quantified by calculating the probability or  $p$ -value as:

$$CL_{s+b} = p_u = \int_{t_{\mu,obs}}^{\infty} f(t_\mu|\mu) dt_\mu \quad (7.7)$$

where,  $t_{\mu,obs}$  is the value of the test statistics  $t_\mu$  obtained from the data and  $f(t_\mu|\mu)$  is a pdf constructed from  $t_\mu$  depending on the signal strength  $\mu$ . The set of values for  $\mu$  that are rejected because their  $p$ -value is below a specified threshold value  $\alpha$  lying on either sides of those not rejected gives a two sided confidence interval of  $\mu$  and if just on one side of the ones not rejected gives an upper limit on the rejected values of  $\mu$ .

In the background only scenario i.e  $\mu = 0$ , the test statistics is defined as:

$$q_\mu = \begin{cases} -2 \ln \lambda(0), & \hat{\mu} \geq 0 \\ 0, & \hat{\mu} \leq 0 \end{cases}$$

where  $\lambda(0)$  is the profilelikelihood ratio for  $\mu = 0$  defined in 7.5. and again to quantify the disagreement between the background-only hypothesis ( $\mu = 0$ ) and the data is given by the  $p$ -value as:

$$CL_b = p_0 = \int_{q_{0,obs}}^{\infty} f(q_0|0) dq_0 \quad (7.8)$$

where  $f(q_0|0)$  denotes the pdf if the test statistics  $q_0$  under the background-only ( $\mu = 0$ ) hypothesis. Figure 7.1 shows a sampling distributions of the test statistics and how the

$p$ -values can be extracted from these distributions.

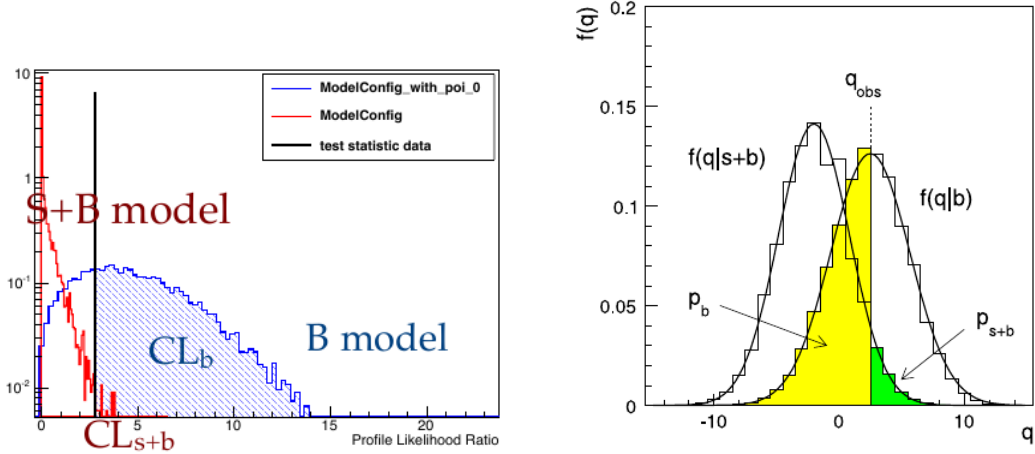


Figure 7.1: Sampling distributions for  $f(t_\mu|\mu)$  showing how one extracts the  $p$ -values. left: is the using a analytic of the Asymptotic method and right: is from the HybridNew method.

In addition to the  $p$ -value, for expressing the disagreement between the data and a given hypothesis, the Higgscombine tool also provides a quantity known as the *significance* ( $\mathcal{Z}$ ).  $\mathcal{Z}$  and the  $p$ -value have a very non-linear relation. Once can defined that relation using a two-sided fluctuation if a Gaussian variable  $\sigma$ , with  $5\sigma$  significance corresponding to a  $p$ -value of  $p = 5.7 \times 10^{-7}$  to denote a discovery. Since, we have not observed any significant excess of events over our standard model background, we will not mention a lot about significance in this thesis, but rather talk about  $p$ -values as they are indispensable in computing limits.

The important question is always, how does one obtain an expression or a distribution of the test statistics and  $f(t_\mu|\mu)$  from the likelihood function? To answer this question, the HiggsCombine tool was developed which consist of various ways of both analytically (e.g the Asymptotic statistical method [60]) or through numerical integration or Monte Carlo computation ( e.g the HybridNew statistical method) obtain the test statistics and  $f(t_\mu|\mu)$ . We have shown the limit computation results of both methods as used in this analysis. As an example, the pdf  $f(q_\mu|\mu)$  of the test statistics ( $q_\mu$ )

obtained through the **Asymptotic** statistical method as given in [60] is:

$$f(t_\mu|\mu') = \Phi\left(\frac{\mu - \mu'}{\sigma}\right)\delta(t_\mu) + \frac{1}{2}\frac{1}{\sqrt{2\pi}}\frac{1}{t_\mu} \exp\left[-\frac{1}{2}\left(\sqrt{t_\mu} - \frac{\mu - \mu'}{\sigma}\right)^2\right] \quad (7.9)$$

where result to a half-chi-square distribution when  $\mu = \mu'$ .

In subtle point worth mentioning is that in the HybridNew approach, systematics uncertainties are taken into account through the Bayesian prior density  $\pi(\theta)$ , and the distribution of the test statistics is computed under the assumption if the Bayesian model of average given as:

$$f(q) = \int f(q|\theta)\pi(\theta)d\theta$$

and the prior pdf  $\pi(\theta)$  is obtained from some measurements characterised by a given likelihood function  $\mathcal{L}_\theta(\theta)$  which is then used to find the prior using Bayes' Theorem. Unlike other cases where systematic uncertainties are taking as being part of the data and incorporated directly through  $\mathcal{G}(\theta)$  as shown in equation 7.4. Nevertheless, they arrive at the same result.

In summary, the hypothesis test is performed using a given statistical method on each value of a chosen parameter of interest (POI)(usually denoted  $\mu$ ). The  $p$ -value if obtained from the sampling distribution of the test statistics being used. Can either obtain this test statistics analytically or through Monte Carlo computation and numerical integration. By plotting the p-value as a function of the POI, we obtain the p-value curve (in this case the  $CL_s = \frac{CL_{s+b}}{CL_b}$ ). The value of  $\mu$  which has a p-value  $\alpha$  ( e.g 0.05) is the upper limit (for 1-dimensional limits, 2-dimensional limits gives lower and upper limits) of  $1 - \alpha$  confidence interval (e.g 95%).

## combined result

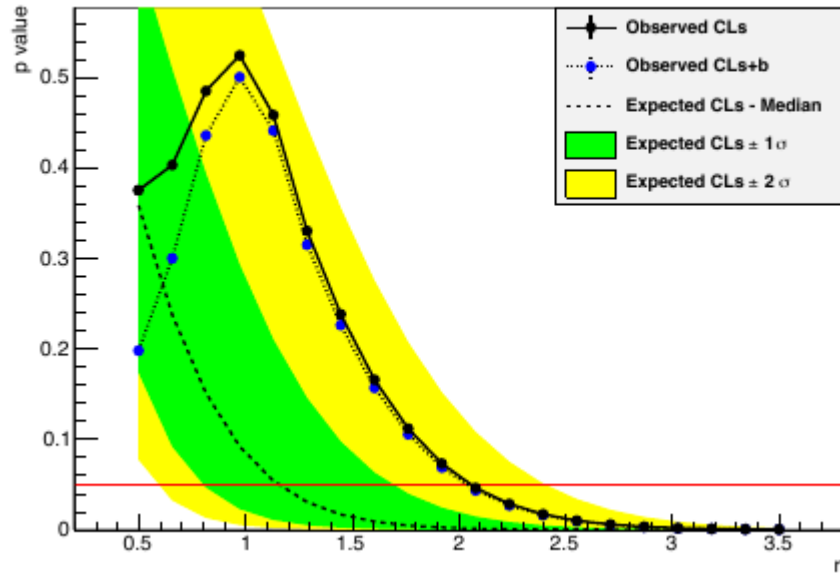


Figure 7.2: Distribution of  $p$ -values showing how upper limit on  $\mu$  is extracted for a given threshold probability.

# Chapter 8

## Limit Interpretation

Using the  $CL_s$  technique, the HiggsCombine tool produces an upper limit along with the expected limit at different quantiles as the signal strength computed which is a ratio of Number of Signal events over the Number of Expected signal events i.e

$$r = \frac{N^{Obs}}{N_{expect}} \quad (8.1)$$

and using the equation as given in chapter 3 on the cross-section  $\sigma = \frac{N}{\varepsilon \cdot A \cdot \mathcal{L}}$  and hence the observed cross-section upper limit is given as:

$$\sigma_{UL}^{Obs} = \frac{r \cdot N^{expect}}{\varepsilon \cdot A \cdot \mathcal{L}} \quad (8.2)$$

where  $\mathcal{L}$  is the integrated luminosity ( $19 \text{ fb}^{-1}$ ) and  $\varepsilon$  and  $A$  are the signal selection efficiency and Acceptance respectively. In addition to the observed limits (Solid black line), the uncertainties on the expected limits at 68%/16% ( $\pm 1\sigma$ ) and at 98%/2.5% ( $\pm 2\sigma$ ) provide the **GREEN** and **YELLOW** respectively, the error from the median (50%) expected limits (dashed red line) shown in figure 8.2.

### 8.1 Signal Efficiency and Acceptance

The efficiency times acceptance ( $\varepsilon \times A$ ) combined as one is seen the figure 8.1.

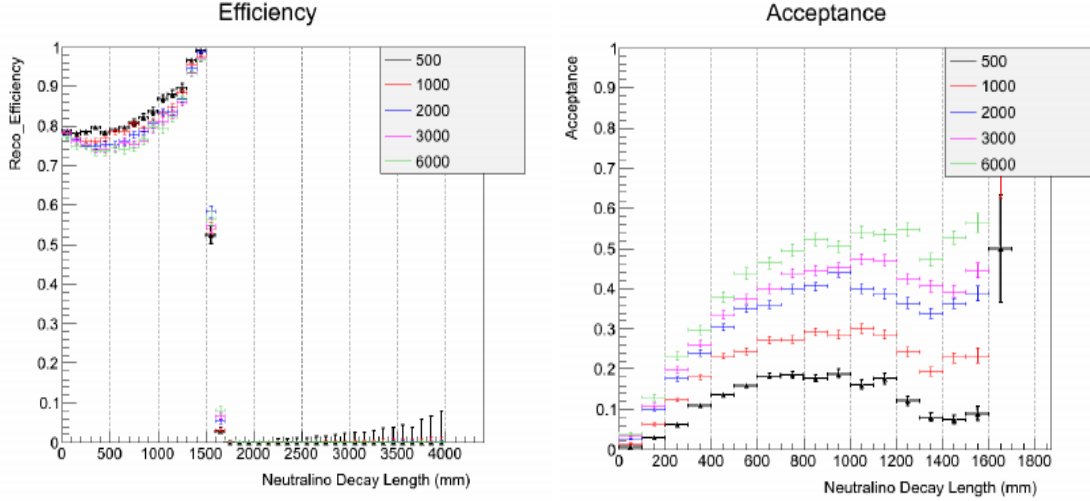


Figure 8.1: The reconstruction and selection efficiency (left)  $\times$  Acceptance ( $t > 3$  ns) (right) against transverse decay length in laboratory frame for different  $c\tau$  points.

The  $\frac{N_{expet}}{\mathcal{L}}$  defines the expected signal cross section which is obtained from a given signal model. In our scenario, our choice of signal model we want to produce exclusion limits on the possible production and decay of a long-lived particle described by this signal model is GMSB. Thus the interpretation of our search analysis is given within the context of any GMSB model with a long-live neutral particle decaying to a photon and gravitino. Such a model is the minimal GMSB or the SPS8 model and the general GMSB model. However, the results provided are based on interpretation within the context of the SPS8 model. In GMSB, the neutralino  $\tilde{\chi}_1^0$  is the NLSP and decays to the gravitino  $\tilde{G}$  the LSP (as a result of R-parity conservation) in association with a very energetic photon  $\gamma$ . Because of the smallness in mass difference between the  $\tilde{\chi}_1^0$  and the  $\tilde{G}$  as well as the coupling, the  $\tilde{\chi}_1^0$  decay to  $\tilde{G}$  is delayed and as a result, the photon emitted can arrive late in the calorimeter crystals. Measuring the arrival time of the photon on ECAL crystals, we can extract important parameters of theory of GMSB.

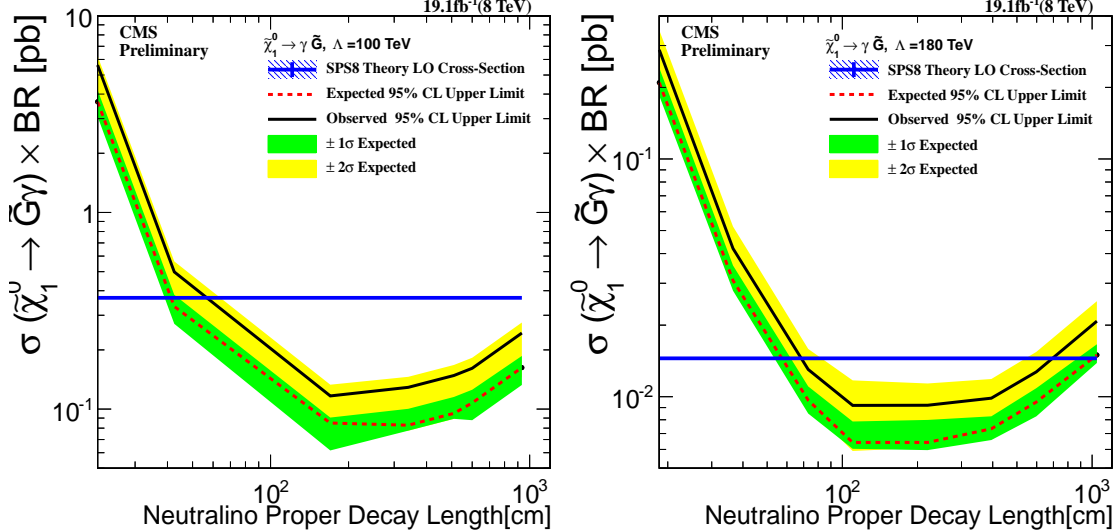


Figure 8.2: Neutralino production cross section against proper delay length upper limit interpretation in SPS8 model. (Left)  $\Lambda = 100$  TeV, (Right)(left)  $\Lambda = 180$  TeV

In the SPS8 model, the parameter space for long-live neutralinos is governed by  $\Lambda_m - c\tau$  2-dimensional parameter space. For each  $\Lambda_m$  point, we have a fixed neutralino mass with different proper lifetimes  $c\tau$ . We have obtained limits for  $\Lambda_m$  ranging from 100 TeV to 180 TeV corresponding to lightest neutralino mass  $m_{\tilde{\chi}_1^0}$  between 90 to 255  $GeV/c^2$  and proper lifetime  $c\tau$  ranging from 250 to 12000 mm corresponding to  $\tau_{\tilde{\chi}_1^0}$  from 0.8 ns to 40 ns.

For a given value of  $\Lambda_m = 180$  TeV, we have a lightest neutralino production cross section times branching ratio plot shown in figure 8.2, showing that the ECAL detector is sensitive to lightest neutralinos of mass  $m_{\tilde{\chi}_1^0} = 255$   $GeV/c^2$  and life time upto 30 ns and we are 95% confident that we have not missed any neutralino whose mass is  $m_{\tilde{\chi}_1^0} = 255$   $GeV/c^2$  and lifetime is  $\tau \leq 30$  ns.

For a given lifetime of  $\tau = 20$  ns, we can also obtain upper limits on the production cross section times branching ratio when compared against their theoretically expected values for a lightest neutralino with mass ranging from  $m_{\tilde{\chi}_1^0} = 90$   $GeV/c^2$  to  $m_{\tilde{\chi}_1^0} = 255$   $GeV/c^2$ . The observed upper limit on this cross section is  $\sigma_{\tilde{\chi}_1^0}^{UP} \geq XX$  pb with proper lifetime of  $\tau = 30$  ns.

Using both the mass and proper lifetime of the lightest neutralino, we present possible

2-dimensional limits simultaneously on  $m_{\tilde{\chi}_1^0}$  or  $\Lambda_m$  and  $c\tau$  or  $\tau$  in the SPS8 model, comparing this with the result of previous experiments. This is shown in figure 8.3.

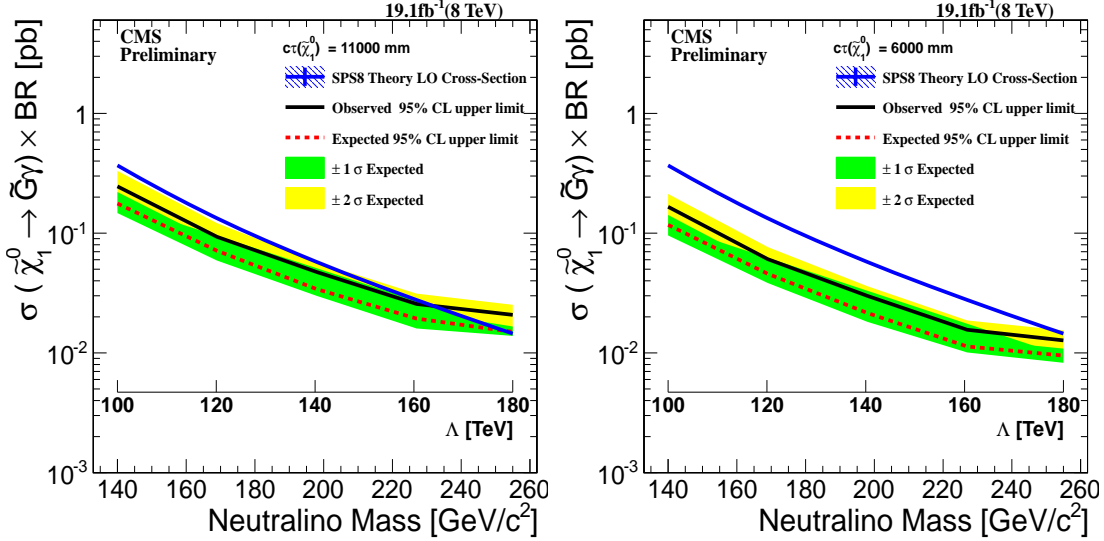


Figure 8.3: Neutralino production cross section against neutralino mass upper limit at 95% confidence levels interpretation in SPS8 model. (Left)  $C\tau = 11000$  mm, (Right)  $C\tau = 6000$  mm

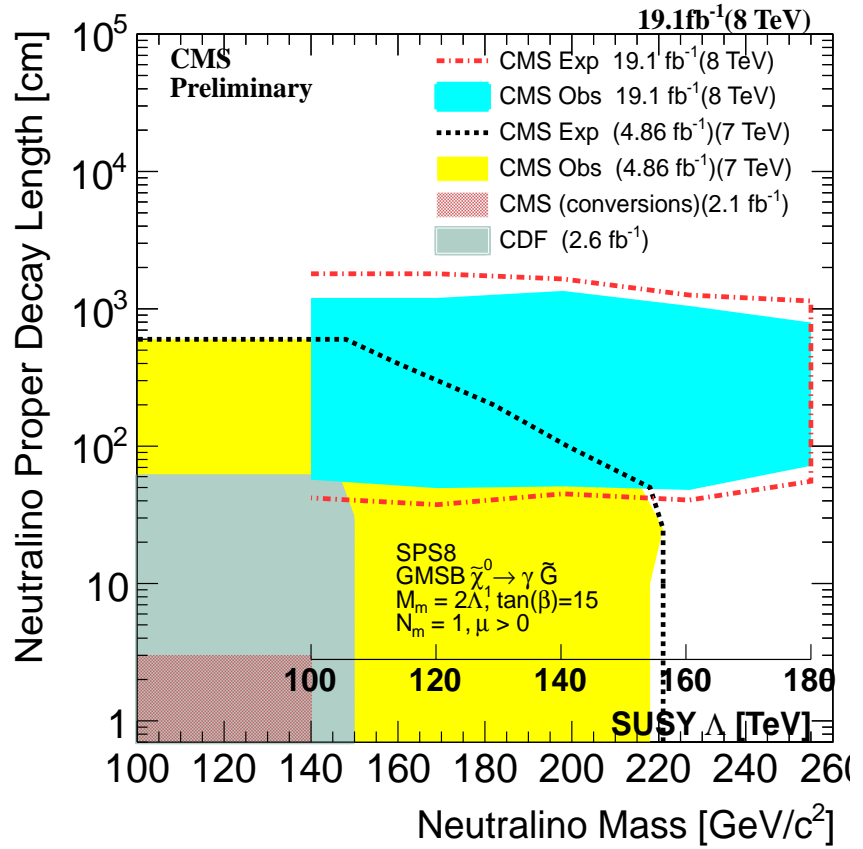


Figure 8.4: Neutralino two dimensional exclusion limit of neutralino mass ( $\Lambda$ ) against proper delay length upper limit interpretation in SPS8 model in the decay  $\tilde{\chi}_1^0 \rightarrow \gamma + \tilde{G}$  with limits from previous experiments shown.

# Chapter 9

## Conclusion

We have performed a search analysis for NMLLP decaying to photons using the time of arrival of the photon as measured by the ECAL sub detector of the CMS detector. Haven fail to find any significant signal of delayed photons over the standard model background, we interpreted our results in SUSY models with NMLLP like SPS8 of minimal GBSM or general GMSB models. We showed that, neutralinos whose production and decay mechanism is described in the SPS8 mGMSB model, with  $m_{\tilde{\chi}_1^0} \leq 235 \text{ GeV}/c^2$  and  $\tau_{\tilde{\chi}_1^0} \leq 35 \text{ ns}$  are ruled out of existence at 95% confidence level using the 2012 8 TeV LHC dataset. This corresponds to an upper limit of  $\sigma_{\tilde{\chi}_1^0}^{UP} \geq 0.02 \text{ pb}$  on the production cross section times branching ratio in a hadron collider. In addition, we mention some of the limitations in this particular analysis from a detector point of view and how in future studies can be improved. We hope that in the future, with increase in center of mass energy of the LHC collider as well as luminosity and an improve in timing resolution beyond what is already very reliable, we will surely find a new fundamental particle whose dynamics cannot be described by the already very successful standard model of particle physics.

# Bibliography

- [1] “*Observation of a new boson at a mass of 125 GeV with the CMS experiment at LHC*”, *Phys. Lett. B* 716 (2012) 30-61
- [2] Steven Weinberg, “A Model of Leptons”, *Phys. Rev. Lett.* 19, 12641266 (1967)
- [3] “Observation of a Charged Charmoniumlike Structure in  $e^-e^+ \rightarrow \pi^+\pi^-J/\psi$  at  $\sqrt{S} = 4.26\text{GeV}$ ” M. Ablikim et al. *Phys. Rev. Lett.* 110, 252001 (2013), “Study of  $e^-e^+ \rightarrow \pi^+\pi^-J/\psi$  and Observation of a Charged Charmoniumlike State at Belle”, Z. Q. Liu et al. *Phys. Rev. Lett.* 110, 252002 (2013);
- [4] Peter W. Higgs “Broken symmetries and the masses of gauge bosons”, *Phys. Rev. Lett.* 13.508, 19 October, 1964;
- [5] Haag,Rudolf; Sohnius, Martin; opuszaski, Jan T. “All possible generators of supersymmetries of the S-matrix”, Nuclear Physics B 88: 257274 (1975);
- [6] Ellis John, Olive Keith A. (2010). “Supersymmetric Dark Matter Candidates”. arXiv:1001.3651 [astro-ph]
- [7] Laura Covi “Gravitino Dark Matter confronts LHC” Journal of Physics: Conference Series 485 (2014) 012002
- [8] J.Ellis, J.Hagelin, D. Nanopoulos, K.A. Olive and M. Srednicki; *Nucl. Phys.* B238 (1984) 453; H. Goldberg, *Phys. Rev. Lett.* 50 (1983) 1419; J. Ellis, T. Falk, G. Ganis, K.A. Olive and M. Srednicki, *Phys. Lett. B* 510 (2001) 236, arXiv: hep-ph/0102098.
- [9] B.Allanach et al,arXiv:hep-ph/0202233v1;

- [10] S.Mathin, arXiv:hep-ph/9709356;
- [11] Howard Baer, Xerxes Tata “Weak Scale Supersymmetry: From Superfields to Scattering Events”
- [12] S. Ambrosanio 1 , Graham D. Kribs 2 , and Stephen P. Martin hep-ph/9703211  
arXiv:hep-ph/9703211v2.
- [13] G.F. Giudice and R. Rattazzi “ Theories with Gauge-Mediated Supersymmetry Breaking” arXiv:hep-ph/9801271v2
- [14] J.Dann et al.(LEPSUSY Working Group), Internal note LEPSUSYWG/97-04(1997), P. Janot, talk at the EPS Conference, Jerusalem, 1997.
- [15] CDF Collaboration, “Search for Supersymmetry with Gauge-Mediated Breaking in Diphoton Events with Missing Transverse Energy at CDFII “,*Phys. Rev. Lett.*
- [16] ATLAS Collaboration “Search for Diphoton Events with Large Missing Transverse Momentum in  $1 \text{ fb}^{-1}$  of 7TeV Proton-Proton Collision Data with the ATLAS Detector”, arXiv:1111.4116v1,17th Nov 2011.
- [17] CMS Draft Analysis, “Search for Long-Lived Particles using Displaced Photons in  $PP$  Collision at  $\sqrt{S} = 7\text{TeV}$  ”, CMS AN AN-11-081 104(2010)011801,
- [18] ATLAS Collaboration, J. High Energy Phys. 1212, 124 (2012), arXiv:1210.4457 [hep-ex]
- [19] The LHC Machine, Lyndon Evans and Philip Bryant *Jinst*,
- [20] CMS Collaboration, “CMS Physics: Technical design report, Volume 1” CERN-LHCC-2006-001
- [21] The CERN Brochure 2009-003-Eng
- [22] CMS Collaboration, “The CMS experiment at the CERN LHC”, JINST 0803:S08004, 2008.
- [23] CMS uses a right-handed coordinate system, with the origin at the nominal interaction point, the  $x$ -axis pointing to the center of the LHC, the  $y$ -axis pointing up

(perpendicular to the LHC plane), and the  $z$ -axis along the counterclockwise-beam direction. The polar angle,  $\theta$ , is measured from the positive  $z$ -axis and the azimuthal angle,  $\phi$ , is measured in the  $x$ - $y$  plane.  $\eta = -\ln \tan(\theta/2)$ . The transverse energy and momentum are defined as  $E_T = E \sin \theta$  and  $p_T = p \sin \theta$  where  $E$  is the energy measured in the tracking system.  $E_T^{\text{miss}} = | - \sum_i E_T^i \vec{n}_i |$  where  $\vec{n}_i$  is a unit vector that points from the interaction vertex to the transverse plane.

- [24] “Timing Distribution at the LHC”, B.G. Taylor Colmar, 9-13 September 2002
- [25] “An FPGA based multiprocessing CPU for Beam Synchronous Timing in CERNs SPS and LHC”. *Proceedings of ICAL EPICS 2003, Gyeongju, Korea ICAL EPICS 2003*
- [26] “Timing and Synchronization in the LHC Experiments”, Varela, J. Krakv, 11-15 September 2000.
- [27] <http://ttc.web.cern.ch/TTC/intro.html>
- [28] “Study of the LHC ghost charge and satellite bunches for luminosity calibration.”, CERN-ATS-Note-2012-029 PERF
- [29] “LHC bunch current normalisation for the April-May 2010 luminosity calibration measurements.”, CERN-ATS-Note-2011-004 PERF
- [30] CMS Collaboration, “The electromagnetic calorimeter. Technical design report”,. CERN-LHCC-97-33
- [31] Bo Lofstedt, “The digital readout system for the CMS electromagnetic Calorimeter”, *Nucl. Inst. Methods in Physics Research*, A 453 (2000) 433-439
- [32] CMS Electromagnetic Calorimeter Collaboration, “Energy resolution of the barrel of the CMS Electromagnetic Calorimeter”, *JINST* 2(2007)P04004.
- [33] CMS Collaboration, “Time Reconstruction and Performance of the CMS Crystal Electromagnetic Calorimeter”, *CFT-09-006*, 2009.
- [34] <https://twiki.cern.ch/twiki/bin/viewauth/CMS/ECALDPGTimeCalibration>
- [35] <https://twiki.cern.ch/twiki/bin/viewauth/CMS/ECALDPGHwTimeCalibration>

- [36] CMS Collaboration, “The CMS ECAL performance With examples”, JINST 9 C02008, 2014.
- [37] CMS-DP-2014/011: “*ECAL Timing Performance Run1*”
- [38] <https://twiki.cern.ch/twiki/bin/view/CMSPublic/EcalDPGResultsCMSDP2014011>
- [39] <https://twiki.cern.ch/twiki/bin/view/CMSPublic/EcalDPGResultsCMSDP2014012>
- [40] “Characterization and treatment of anomalous signals in the CMS Electromagnetic Calorimeter” CMS AN AN-10-357
- [41] “ Mitigation of Anomalous APD signals in the CMS ECAL”, 2013, *JINST 8 C03020*, W.Bialas and D.A. Petyt
- [42] CMS Collaboration, “CMS trigger and data taking in 2010 ”, *CMS CR-2011/051*.
- [43] CMS Collaboration, “Reconstruction of the signal amplitude of the CMS electromagnetic Calorimeter”, *Eur.Phys.J. C46S1(2006)23-35*.
- [44] D.del Re et al “An algorithm for the determination of the flight path of long-lived particles decaying into photons” CMS AN -2010/212.
- [45] CMS Collaboration, “Particle-Flow Event Reconstruction in CMS and Performance for Jets, taus and  $\cancel{E}_T$ ”, CMS Physics Analysis Summary CMS-PAS-PFT-09-001(2009).
- [46] CMS Collaboration, Missing Transverse Energy Performance in Minimum-Bias and Jet Events from Proton-Proton Collisions at  $\sqrt{s} = 7$  TeV , CMS Physics Analysis Summary CMS-PAS-JME-10-004 (2010).
- [47] MET JINST (arXiv:1106.5048)
- [48] CMS Collaboration, “Missing transverse energy performance of the CMS detector”; arXiv:1106.5048v1
- [49] CMS Collaboration, “CMS Physics: Technical design report, Volume 2” CERN-LHCC-2006-001.

- [50] CMS Collaboration, “Determination of Jet Energy Scale in CMS with pp collisions at  $\sqrt{S} = 8$  TeV”, *JME-10-010(2012)*
- [51] “<https://twiki.cern.ch/twiki/bin/viewauth/CMS/EGamma2012>.”
- [52] “Parton distributions for the LHC” *Eur.Phys.J C63(2009) 189-285* or arXiv:0901.0002
- [53] CMS Collaboration, “Search for ADD Extra-dimensions with Photon + MET signature”, *AN-11-319(2011)*
- [54] ISAJET 7.84 F.E. Paige, S.D. Protopopescu, H. Baer and X. Tata, <http://www.nhn.ou.edu/~isajet/>
- [55] T. Sj ostrand, S. Mrenna, and P. Skands, PYTHIA 6.4 physics and manual, *JHEP 05 (2006) 026*, doi:10.1088/1126-6708/2006/05/026, arXiv:hep-ph/0603175
- [56] GEANT4 Collaboration, GEANT4a simulation toolkit, *Nucl. Instrum. Meth. A 506(2003) 250*, doi:10.1016/S0168-9002(03)01368-8.
- [57] “Presentation of search results: the CLs technique”, *A. L Read 2002 J. Phys. G: Nucl. Part. Phys. 28 2693*
- [58] “Computation of confidence levels for search experiments with fractional event counting and the treatment of systematic errors”, *Peter Bock JHEP01(2007)080*
- [59] <https://twiki.cern.ch/twiki/bin/viewauth/CMS/>
- [60] “Asymptotic formulae for likelihood-based tests of new physics” *G. Cowan et al, arXiv:1007.1727v3*
- [61] N.-E. Bomark and L. Roszkowski “3.5 keV x-ray line from decaying gravitino dark matter” *Phys. Rev. D 90, 011701(R)* Published 18 July 2014

## Appendix A

# Glossary and Acronyms

Care has been taken in this thesis to minimize the use of jargon and acronyms, but this cannot always be achieved. This appendix defines jargon terms in a glossary, and contains a table of acronyms and their meaning.

### A.1 Glossary

- **Cosmic-Ray Muon (CR  $\mu$ )** – A muon coming from the abundant energetic particles originating outside of the Earth’s atmosphere.
- **SUSY** – A theoretical model based on a fundamental symmetry called supersymmetry in which the fermions and bosons can exchange their spin, extending the standard model to account for the stability in the observed Higgs boson mass and to also predicting the existence of many extra new particles which could be candidates of dark matter.

### A.2 Acronyms

Table A.1: Acronyms

|          |                                       |
|----------|---------------------------------------|
| NMLLP    | Neutral Massive Long-Lived Particles. |
| DM       | Dark Matter.                          |
| DE       | Dark Energy.                          |
| GMSB     | Gauge Mediated Supersymmetry Breaking |
| LHC      | Large Hadron Collider                 |
| CMS      | Compact Muon Solenoid                 |
| CR $\mu$ | Cosmic-Ray Muon                       |